

Czech Technical University in Prague, Faculty of Electrical Engineering, Department of Physics

3D PIC MODEL OF THE HELICAL CURRENT FILAMENT
(Inaugural dissertation)

Doc. RNDr. Petr Kulhánek, CSc.

Prague 2004

CONTENTS

<u>LIST OF SYMBOLS</u>	3
<u>LIST OF ABBREVIATIONS</u>	6
<u>1. THE ROLE OF THE FILAMENTS IN SPACE AND LAB PLASMAS</u>	7
<u>2. PARTICLE IN CELL MODELING OF THE FILAMENTS</u>	15
2.1. INTRODUCTION	15
2.2. MODEL DETAILS	15
2.3. INITIAL AND BOUNDARY CONDITIONS	16
2.4. GRID	18
2.5. NONDIMENSIONAL VARIABLES	20
2.6. NONRELATIVISTIC AND RELATIVISTIC PARTICLE SOLVERS	21
2.7. WEIGHTING PARTICLES AND FIELDS	29
2.8. FIELD SOLVERS	30
<u>3. PIC PACKAGE ADD-INS</u>	34
3.1. FIELD VISUALIZATION - LIC	34
3.2. PARTICLE VISUALIZATION	41
3.3. DIAGNOSTICS	45
3.4. COLLISIONS	53
3.5. RADIATION	60
3.6. ROLE OF THE DUST	64
3.7. ANIMATIONS	65
<u>4. SUPPORTING THEORY ADD-INNS</u>	66
4.1. FILAMENT EQUILIBRIUM (NON-HELICAL)	66
4.2. RADIATING FILAMENT EQUILIBRIUM (NON-HELICAL)	73
4.3. HELICAL STRUCTURES	79
<u>5. RESULTS AND CONCLUSIONS</u>	85
<u>REFERENCES</u>	92
<u>ACKNOWLEDGEMENT</u>	98

LIST OF SYMBOLS

A	vector electromagnetic potential
B, B	magnetic field induction
<i>c</i>	speed of light
B_{ext}	external magnetic field induction
<i>C_V</i>	heat capacity (at constant volume)
D	electric field induction
<i>D</i>	cumulative distribution function
E, E	electric field intensity
e_r, e_φ, e_θ	unit vectors, spherical coordinates
f_B	magnetic pressure force density
f_p	plasma pressure force density
f_R	curvature force density
F_e, F_e	electrostatic force
F_g, F_g	gravitational force
<i>G</i>	gravitational constant
G_x, G_y, G_z	granularity of the grid in <i>x</i> , <i>y</i> and <i>z</i> directions
H	magnetic field intensity
<i>H</i>	helicity
<i>I</i>	intensity of radiation
j	current density
j_C	conductive current density
j_M	magnetization current density
j_{∇B}	gradient <i>B</i> drift current density
J	current
<i>J_{PB}</i>	Pease-Braginski current
<i>J</i>	total current in area $\langle 0, r \rangle$ of the filament
<i>k_B</i>	Boltzmann constant
<i>k(s)</i>	convolution kernel
<i>K</i>	integral helicity
<i>L</i>	length

L_x, L_y, L_z	length of the grid in x , y and z directions
$\ln \Lambda$	Coulomb logarithm
m_e, m_i, m_n	mass of electrons, ions and neutrals
n_e, n_i, n_n	concentration of electrons, ions and neutrals
M	magnetization
n	unit position vector of the observer \mathbf{R}/R
N_e, N_i, N_n	number of electrons, ions and neutrals
N_x, N_y, N_z	number of grid points in x , y and z direction
F	force
p	pressure
P	polarization
P	probability
P	radiation power density
Q_e, Q_i, Q_n	charge of electrons, ions and neutrals
r	radial coordinate
R	position vector of the observer
r_D	Debye radius
t	time
t'	retarded time
T_e, T_i, T_n	temperature of electrons, ions and neutrals
u	$\mathbf{u} \equiv \gamma \mathbf{v}$, auxiliary quantity for relativistic calculations
V	volume
V	vector field
$\mathbf{v}_e, \mathbf{v}_i, \mathbf{v}_n$	velocity of electrons, ions and neutrals
$\mathbf{x}_e, \mathbf{x}_i, \mathbf{x}_n$	position of electrons, ions and neutrals
W	energy
W_M	magnetic field energy
z	ionization degree
α	power-step exponent
β	relativistic coefficient v/c
β	power-step exponent
β	pitch angle

γ	relativistic coefficient gamma
γ	polytrophic exponent
γ_k	random number
$\Delta x, \Delta y, \Delta z$	space step (grid)
Δt	time step
ϵ_0	vacuum permittivity
ϵ_{kl}	permittivity tensor
η_M	magnetic viscosity, $\eta_M \equiv 1/\sigma\mu_0$
θ	spherical coordinates' angle
κ	$1 - \mathbf{n}\mathbf{v}/c$
μ_0	vacuum permeability
μ_{kl}	permeability tensor
ν, ν_α	collision frequency
ξ	nondimensional radial coordinate in filament, $\xi \equiv r/R$
ρ	charge density
σ	conductivity
σ_{kl}	conductivity tensor
σ	differential cross section area
$\sigma(s)$	field line parameterized by its length
τ_d	characteristic time of diffusion
φ	polar angle
ϕ	scalar electromagnetic potential
ϕ_g	scalar gravitational potential
χ	magnetic susceptibility
ω_c	cyclotron frequency of electrons
$\omega_{pe}, \omega_{pi}, \omega_{pd}$	plasma frequency of electrons ions and charged dust
$\omega_{\mathbf{v}}$	vorticity
Ω	space angle

LIST OF ABBREVIATIONS

AGN	Active Galaxy Nuclei
BB	Boris – Buneman
CIC	Cloud In Cell
CN	Canonical
CPU	Central Processor Unit
CTU	Czech Technical University
DFT	Discrete Fourier Transform
EOL	End Of Line
EOF	End Of File
FFT	Fast Fourier Transform
GUI	Graphical User Interface
IDFT	Inverse Discrete Fourier Transform
IFFT	Inverse Fast Fourier Transform
LF	Leap-frog
LIC	Line Integral Convolution
MC	Monte Carlo
MUDPACK	Multigrid Package
NE	Newton – Euler
NGP	Nearest Grid Point
OpenGL	Open Graphic Library
PC	Personal Computer
PDE	Partial Differential Equation
PIC	Particle In Cell
PM	Particle – Mesh
PP	Particle – Particle
RGB	Red – Green – Blue
RK	Runge – Kutta
UCAR	University Corporation for Atmospheric Research

1. THE ROLE OF THE FILAMENTS IN SPACE AND LAB PLASMAS

Plasma in the Universe

About 99 percent of all the matter in our Universe is in the plasma state. Only on the Earth we luckily live in the one percent of another state. Nevertheless there are a lot of plasma phenomena we can see on the Earth: the lightning channels, ionosphere, auroras and the whole Earth magnetosphere. In the Sun system the plasma is in the solar wind, planet magnetospheres and cometary's tails. In the Jupiter's and Saturn's surroundings the plasma forms giant plasma toruses. And the Sun itself, as well as all the other stars, is a huge plasma ball and the well-known plasma phenomena such as protuberances, sunspots, prominences, spicules are worth of investigating [60-63]. Not only stars but knock-out most of nebulas in galaxies are wide plasma clouds. In the nebulas we can see typical plasma phenomena: filament structures caused by the presence of electric and magnetic fields, acceleration of charged particles and radiation of various origins. In the vicinity of the Galaxy centre there are extensive plasma filaments with length about 250 light years perpendicular to the Galaxy disk. In other galaxies similar shapes are observed, especially in the so called Active Galaxy Nuclei (AGN). Neighboring galaxies are interconnected through hydrogen plasma bridges (e.g. our Galaxy and Magellan clouds). Typical quasar and AGN jets are plasma formations and the characteristic double radio spots have origin in the related plasma phenomena. In this decade numerical simulations validated that plasma phenomena could be responsible for the star creation from protostar nebulas and enable to form the original globules without achievement of the Jeans criterion values and even without initial shock wave generated by neighboring supernovae. Furthermore it seems that galaxy spirals could be formed both by electromagnetic and gravitational forces. High energy particles in cosmic rays were accelerated in plasma filaments and double layers. Today we come to somewhat different picture of our universe: it is not only gravitation which is responsible for the phenomena in our world, electromagnetic interaction and its properties contribute by equal role to the structures of our universe [3, 4, 10].

Usually plasma is defined as a quasi-neutral state of matter with free carriers of charge and collective phenomena. In plasma clouds the electromagnetic interaction forms typical plasma filaments and walls. Charged particles drift perpendicularly to the magnetic field lines [81], a great number of electromagnetic and acoustic waves propagate through the plasma [68, 74, 76, 84]. Plasma instabilities can be responsible for short time energy bursts, double layers for acceleration of charged particles to the considerable velocities, etc. The plasma phenomena are fascinating and plentiful.



Fig. 1: Filamentary structures in the Vela supernovae remnant. Photography by David Malin, UK. Schmidt Telescope, Anglo Australian Telescope board, 1996.

Plasma filaments

Plasma filaments (fibers, pinches) belong to the most common structures in both lab and space plasmas. The simplest formation is a plasma column with axial current and azimuthal magnetic field. This field acts by means of the Lorentz force on the column and pinches it in radial direction. Gradient of the plasma pressure is in equilibrium with the Lorentz force. This equilibrium is unstable and filament of such a kind disintegrates quickly. If the magnetic field lines are twisted into magnetic strand (both azimuthal and axial components are nonzero), the filament is much more stable and survives for a long time. These filaments are called *helical pinches* and are described by the quantity called *helicity*.

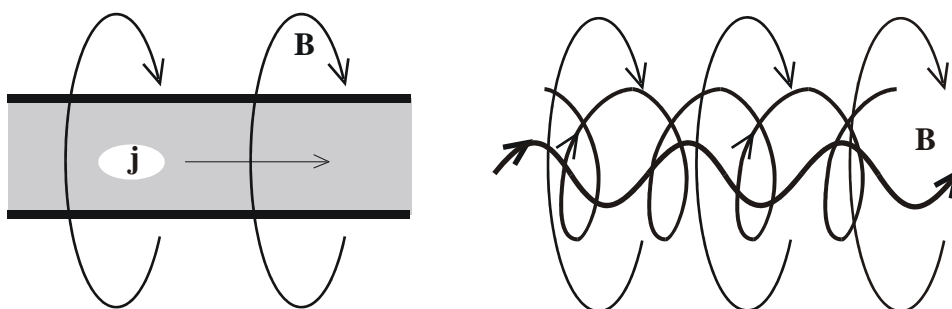


Fig. 2: Left: z-pinch, axial current, azimuthal field. Right: Helical pinch.

In “long living” pinches the helical structure is usually observed. In the laboratory pinch the spirals suddenly occur in the final steps of the evolution. The current density and magnetic field

have both axial and azimuthal components. The helical structures seem to be relatively common feature of the plasma behavior [3, 10, 20, 52, 58].

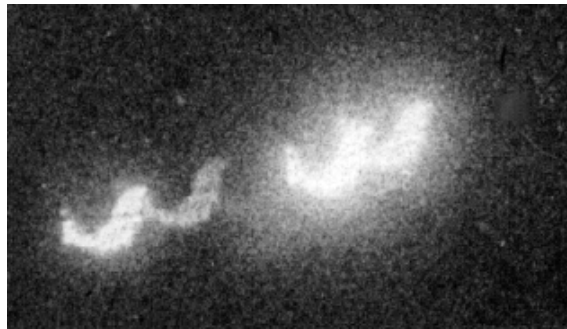


Fig. 3: Cu filament discharge spiral, $\varnothing 110 \times 10^{-6}$ m, 1.3 MA, RTG, S-300 device, RRC Kurchatov Institute, 1998. Shot No. 19059801. Camera obscura $\varnothing 100 \times 10^{-6}$ m, foil 24×10^{-6} m Mylar + 120 nm Al.

In space plasma (e.g. in cometary's tails) are sometimes observed intertwined *double-spirals*. Two parallel helical filaments with the same current density orientation are attracted on long distances (as conductors with parallel current). But on short distances repulsion caused by azimuthal current component occurs. That is the reason why bounded double-spirals exist. In lab one more filament configuration is of a great interest: *toroidal pinch* – plasma confined in tokamaks. The two main components of current density and magnetic field are called poloidal (instead of azimuthal) and toroidal (instead of axial).

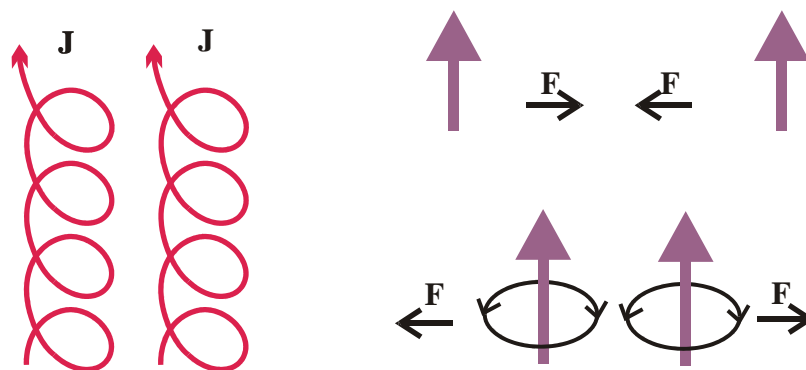
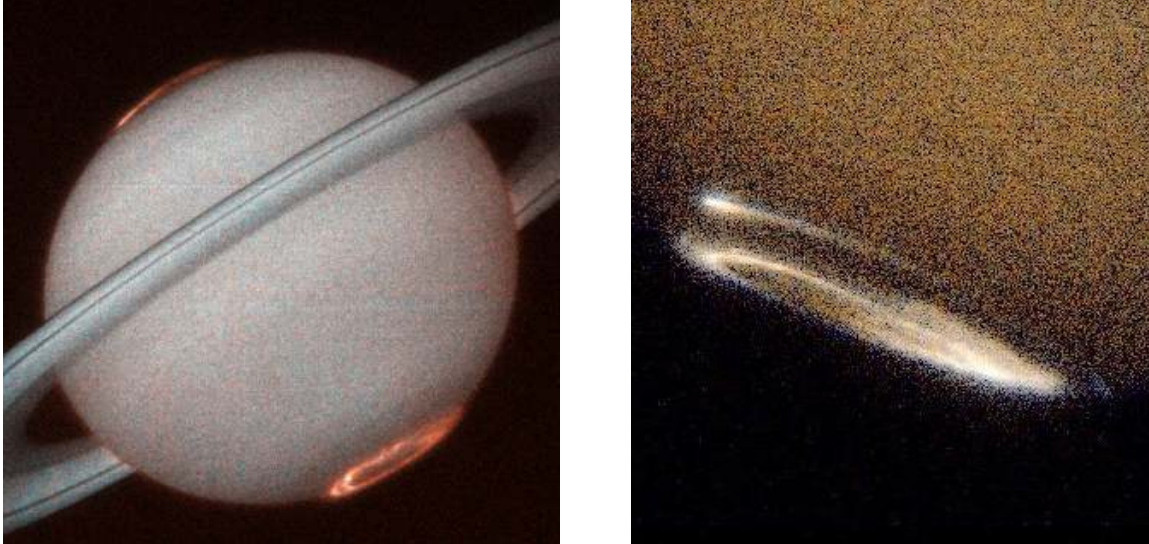


Fig. 4: Double-spirals

Another typical plasma structures are *pinch layers or plasma sheaths* [46]. Similarly to the filaments these shapes are confined by magnetic field generated by surface currents. These structures are known from terrestrial observations. In auroral area vertical plasma sheaths are localized approximately 70° of south and north latitude. The thickness of the sheaths is several tens of kilometers, linear dimension are thousands of kilometers. The sheath is oriented along the Earth magnetic field lines. Through the sheath passes a discharge with current density of magnitude approximately $30 \mu\text{A}/\text{m}^2$. This current generates internal magnetic field with well-

known accompanying phenomena such as *aurora polaris*. This field corresponds to the azimuthal field in the filament. First detection of terrestrial pinch sheaths comes from navigation satellite 1963-38C and was done in 1966. First detailed research of these interesting structures did satellite TRIAD in 1976. The aurora polaris is nowadays relatively well explored phenomenon not only on the Earth, but also on Saturn and Jupiter.



Figs. 5, 6: Saturn's aurora polaris (left). Jupiter's aurora polaris (right). Consequence of the discharge in plasma pinch sheath in auroral area. HST, STIS camera, UV, 1998.

Force free configuration and Birkeland currents

In plasmas so called force free configurations with current density aligned along magnetic field are very common, $\mathbf{j} \parallel \mathbf{B}$ (Birkeland current). In this case the Lorentz force density $\mathbf{j} \times \mathbf{B}$ is zero. Such a configuration has the lowest possible energy and plasma with energy dissipation tends to this configuration. The force free magnetic field is always helical (see chapter 4.1). The force free configuration evolves in final steps of the filament evolution and matches the onset of helical mode. Let us figure out the most widely known structures with Birkeland currents:

- *Lab pinches*. If the pinch survives for a sufficiently long period of time it evolves in force free helical configuration with Birkeland currents.
- *Aurora polaris*. In auroras the electric current typically flows along the Earth magnetic field. Longitudinal filaments of the length about 100 m are observed very often.
- *Venus ionosphere*. In the Venus ionosphere current Birkeland filaments with the length up to 20 km were detected.

- *Jupiter-Io*. From the plasma point of view it is an exceptionally interesting system. The Jupiter's moon Io ejects a lot of sulphur plasma due to its volcanic activity. Along the whole Io's trajectory extensive plasma torus originates. Along the Jupiter's magnetic field lines (perpendicularly to the plasma torus) Birkeland currents flow. They are closed through the Io and together with the tidal forces warm up the moon. The magnitude of these Birkeland currents is estimated to be about several mega amperes.
- *Comets*. In cometary's tails long living filamentary structures are occasionally detected. After the discovery of magnetic field presence in cometary's tails it is obvious that these structures are formed due to the Birkeland currents.

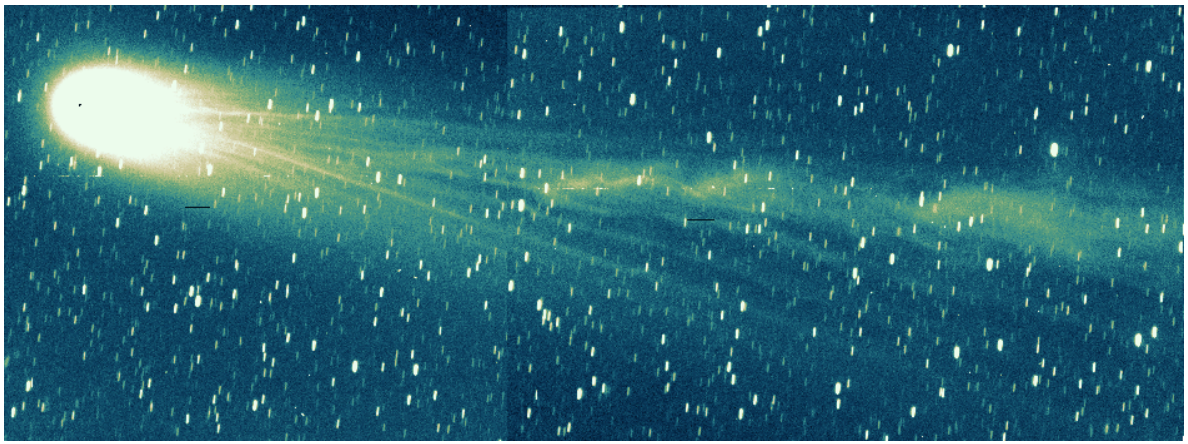


Fig. 7: The comet Hyacutake. The tail has characteristic filamentary structure. March 20, 1996.

- *Sun*. In the solar activity we can find a great number of helical structures with Birkeland currents flowing along the local magnetic field lines: Prominences (10^{11} A), spicules, corona currents, chromosphere eruptions, etc.

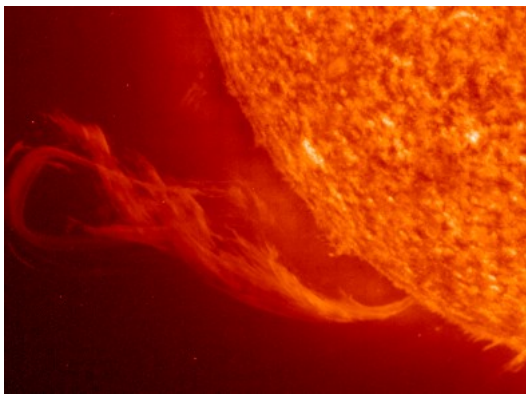


Fig. 8: Solar prominence controlled by magnetic field.

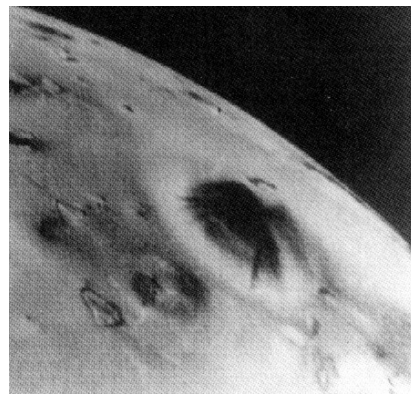


Fig. 9: Active volcano Prometheus on Io. Voyager 2, 1979.

- *Nebulas*: In nebulas filamentary structures are mostly detected. Unfortunately we have no direct evidence of Birkeland filaments, nevertheless there are indirect indicia: observation of polarized synchrotron radiation which originates only in areas with magnetic fields and

detection of high energy particles phenomena; such particles could be accelerated in plasma pinch structure.

- *Galaxy center.* There are several filaments with length approximately 60 pc near the center of our Galaxy. They look like twisted ropes and have helical structure. It is probable that they are plasma formations confined by the magnetic field. The estimation of the current and field magnitude is based only on vague dimension extrapolation.
- *Radio galaxies, AGN, quasar jets.* In the vicinity of these energetic objects, filamentary structures, which are probably generated by electromagnetic interaction, are detected.

Radiation

In filament, the Joule heating is compensated by the radiation processes. There are three basic mechanisms of the radiation: recombination, bremsstrahlung and synchrotron radiation. The recombination is dominant for the temperatures bellow 10^5 K, the bremsstrahlung in the temperature interval $(10^5 \div 10^7)$ K and synchrotron radiation above 10^7 K [35, 45].

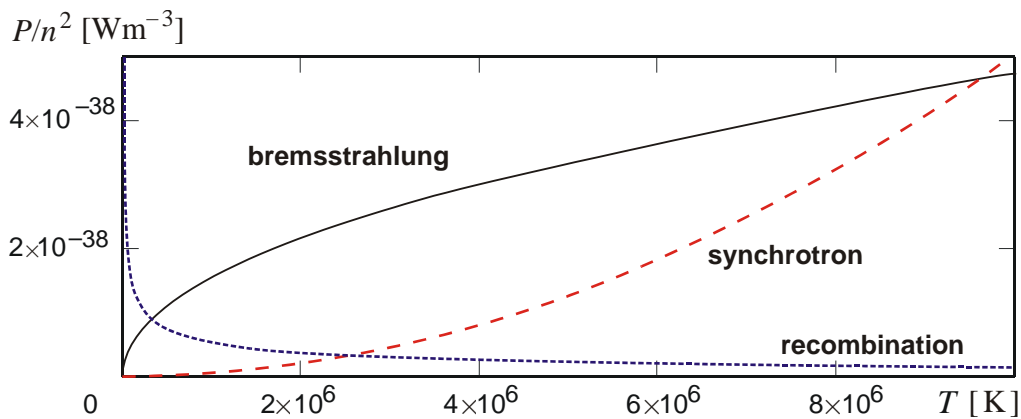


Fig. 10: Radiation channels

The radiation dominantly influences the behavior of the filament. The filament has not Bennett profile [35, 45], its boundary is not sharp, and the pressure tends to zero very slowly. In some cases the depletion of the concentration in the pinch center occur (hollow pinch). Due to the radiation, the temperature gradient cannot be neglected. The temperature gradient leads to the chemical and charge separation in the radial direction and can result in diocotron instability and the onset of the helical mode.

Electromagnetic collapse

Plasma filaments are typical equilibrium structures for electromagnetic interaction. On the contrary for gravitation interaction the typical equilibrium structures are spherical (e.g. stars, planets, etc.). In stars the pressure gradient of matter is balanced by the gravitational field; in

plasma filaments the pressure gradient of matter is balanced by the gradient of magnetic pressure (Lorentz force). Let us compare these two typical equilibrium configurations:

- The symmetry of gravitationally bounded objects is spherical; the symmetry of electromagnetically bounded objects is either cylindrical or planar.
- Gravitationally bounded object is not dependent on its surroundings. Plasma filaments have nonzero current density evoked by external circuit in lab and by external fields in space.
- Both configurations can exist in different dimensions. This is caused by different strength of electromagnetic and gravitational forces. For example the ratio of these forces for two protons is $F_e/F_g = 10^{36}$. Due to this fact filaments of small dimensions can be created in lab (millimeters and centimeters) In these filaments the state of matter is similar to that of the star interior.
- The star equilibrium configuration is in a wide range of parameters stable, the equilibrium of the filaments mostly unstable. Generally, helical pinches suffer from instability phenomena much less than z-pinches.

In 1957 R. S. Pease and S. Braginski independently predicted the possibility of electromagnetic collapse. The current passing through the filament heats it up by Ohmic processes. This energy is carried out by recombination, bremsstrahlung and synchrotron radiation. If the total current in the filament is sufficiently high, the equilibrium is broken, magnetic gradient pressure outbalances the gradient pressure of matter and the plasma filament collapses to the center [43]. During this process the temperature decreases because of the intensive drain-off energy by radiation. This collapse can be stopped by the pressure of degenerated electron or neutron gas. The scenario of the electromagnetic collapse reminds the final evolution stages of stars – gravitational collapse to white dwarf or neutron star. The electromagnetic collapse ought to occur for current higher than $J_{PB} = 1.6$ MA (derived by Pease and Braginski for bremsstrahlung). In lab the filaments divide into several smaller filaments before reaching the Pease-Braginski current. In these sub-filaments the current is sub critical. In high energy filaments the radiation mechanism is not bremsstrahlung one, the synchrotron radiation for which the Pease-Braginski calculation is not correct, prevails. The possibility of the existence of the electromagnetic collapse is nowadays still open. In the biggest apparatuses (Saturn – Sandia Labs, USA) are conditions very near to the electromagnetic collapse and the matter is in super dense state. Especially so called hot dots radiating in X-ray region are very interesting.

Present state

In the Department of Physics of the CTU the plasma filaments are investigated for many years. The experimental background is oriented on diagnostic methods including schlieren photography, Quadro camera diagnostics, X - ray and VUV diagnostics, interferometry measurements, etc. [13-15,17-18, 21-28, 30, 33]. In 1997 spirals surrounding the pinch were detected. This phenomenon seems to have the same nature as structures observed in space.

The theoretical research formally orientated on the pure z -pinch [11, 12, 16, 19, 31, 32, 34, 36, 37, 39]. The model was based on the equilibrium equation, Ampere law, energy balance equation and Ohm law. The radiative processes were included in the energy balance equation. Later the helical structures and conditions of their onset were investigated. Calculations of the helical equilibrium states were done in [45, 65, 69, 72, 79, 80].

In parallel with the experimental and theoretical endeavor a PIC program package simulating the onset of helical states in plasma filaments was developed [50, 51, 54, 59, 64, 67, 70, 71, 73, 75, 77, 78]. Description of this PIC package is the main topic of this dissertation.

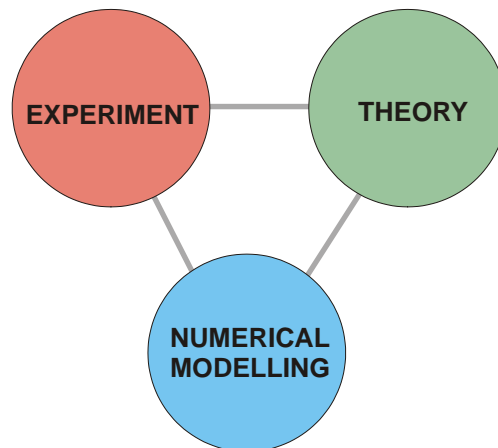


Fig. 11: Three integral parts of present day physics

2. PARTICLE IN CELL MODELING OF THE FILAMENTS

2.1. Introduction

Very good model for the description of filament structures is the PM (Particle Mesh) model [5, 7, 55, 57]. Particles move freely through the mesh and fields are located in the mesh points only. The fields are calculated from the Maxwell equations via some suitable field solver. As the particles are located anywhere in the computational area and the fields are located in the mesh points, some weighting procedure of the particles to the mesh points and of the fields to the particles must be implemented in the model. Our endeavor in search of fast and efficient particle and field solvers as well as field display technique and diagnostics of the numerical experiment is the main topic of this dissertation. Detailed description of the model and its results can be found in papers [50, 51, 54, 55, 59, 64, 67, 70, 71, 73, 75, 77, 78].

2.2. Model Details

Program code was written in FORTRAN 95, free-style (without compulsory columns). FORTRAN compiler and linker were used from Compaq Visual FORTRAN 6.6 A embedded in the Microsoft Development studio GUI.

PIC parameters

Particle solver: Newton, Runge Kutta, Leap Frog, Buneman, Canonical

Field solver: FFT, Multigrid

Weighting: 0, 1

Particle parameters: Q/Qe, M/Me, N, T[eV]

Qe: -1, Qi: +1, Qn: 0
Me: 1, Mi: 8, Mn: 8
Te: 3, Ti: 3, Tn: 3
Ne: 50000, Ni: 50000, Nn: 200

Perturbation: Sausage, Kink, Radial Field, Axial Current
Magnitude: 0.2

Model input: Background, Beam R, Beam L
e: e, i, n
e: e, i, n
Beam diameter (%): 20

Beam parameters: Ve: 0, Vi: 0, Vn: 0
Te: 3, Ti: 3, Tn: 3
Ne: 400000, Ni: 400000, Nn: 1000

External nondimensional fields E, B: Ex: 1, Ey: 1, Ez: 0
Bx: 0, By: 0, Bz: 1

Model output: Diagnostics (2 # steps/diag), Visualiz. File (250 # steps/snap), Radiation File (1 # steps/rad), Bitmap File (200 # steps/bmp)

Grid: size Lx, Ly, Lz, granularity G (integer 1...8)
Lx: 1000, Ly: 1000, Lz: 1000
Gx: 4, Gy: 3, Gz: 3

Draw: PIC redraw, Grid, Electric field, Magnetic field
 Plane (x,y), Plane (y,z), Plane (z,x)

total steps: 50

OK

Fig. 12: GUI of the PIC model. Input dialog (version without dust particles).

Fully three-dimensional code with periodical boundary conditions was developed. The fields are solved via either FFT solver or Multigrid solver. There are implemented five particle solvers in the PIC package (Newton-Euler, Boris-Buneman, Leap-Frog, Runge-Kutta and Canonical). A special graphical package based on the OpenGL Library was developed for visualization of the particles and fields [56]. The field visualization method is based on LIC (Line Integral Convolution) algorithm [48, 49]. Another package was developed for calculation of the filament radiation processes [50].

2.3. Initial and Boundary Conditions

There are three types of particles included, which may vary by their charge and mass (usually electrons, ions and neutrals). The particles are localized in three-dimensional rectangular parallelepiped with periodical boundary conditions. These conditions can be applied for particle's motion and internal fields. They cannot be used for potentials of external fields (e.g. homogeneous electric field has linear potential ϕ dependence which must have discontinuity on the boundary).

Initial coordinates

Initial coordinates of the particles are generated randomly. In the computational area two beams and surrounding particles are present. The beam's radius and particles' velocity and temperature can be chosen.

Initial velocities

The initial particle velocity has two components: The beam (ordered) and the random one. The beam velocity can be assigned to the beam particles, the chaotic component is entered as temperature of the particles and corresponding Gaussian distribution is generated according the following algorithm. If we rewrite the Gauss velocity distribution

$$dw(v_k) = \frac{m}{\sqrt{2\pi mkT}} \exp\left[-\frac{mv_k^2}{2k_B T}\right] dv_k ; \quad k = 1, 2, 3 \quad (1)$$

into nondimensional form ($mv^2/k_B T = x$)

$$f(x) = \frac{1}{\sqrt{2\pi}} \exp\left[-\frac{x^2}{2}\right]; \quad x \in (-\infty, \infty), \quad (2)$$

two succeeding values x_1 and x_2 of the distribution will be given by formulas [83]

$$\begin{aligned}x_1 &= \sqrt{-2 \ln \gamma_1} \cos(2\pi\gamma_2); \\x_2 &= \sqrt{-2 \ln \gamma_1} \sin(2\pi\gamma_2),\end{aligned}\tag{3}$$

where γ_1 and γ_2 are random numbers from the interval $(0, 1>$. The initial temperature of the beam and surrounding particles can differ.

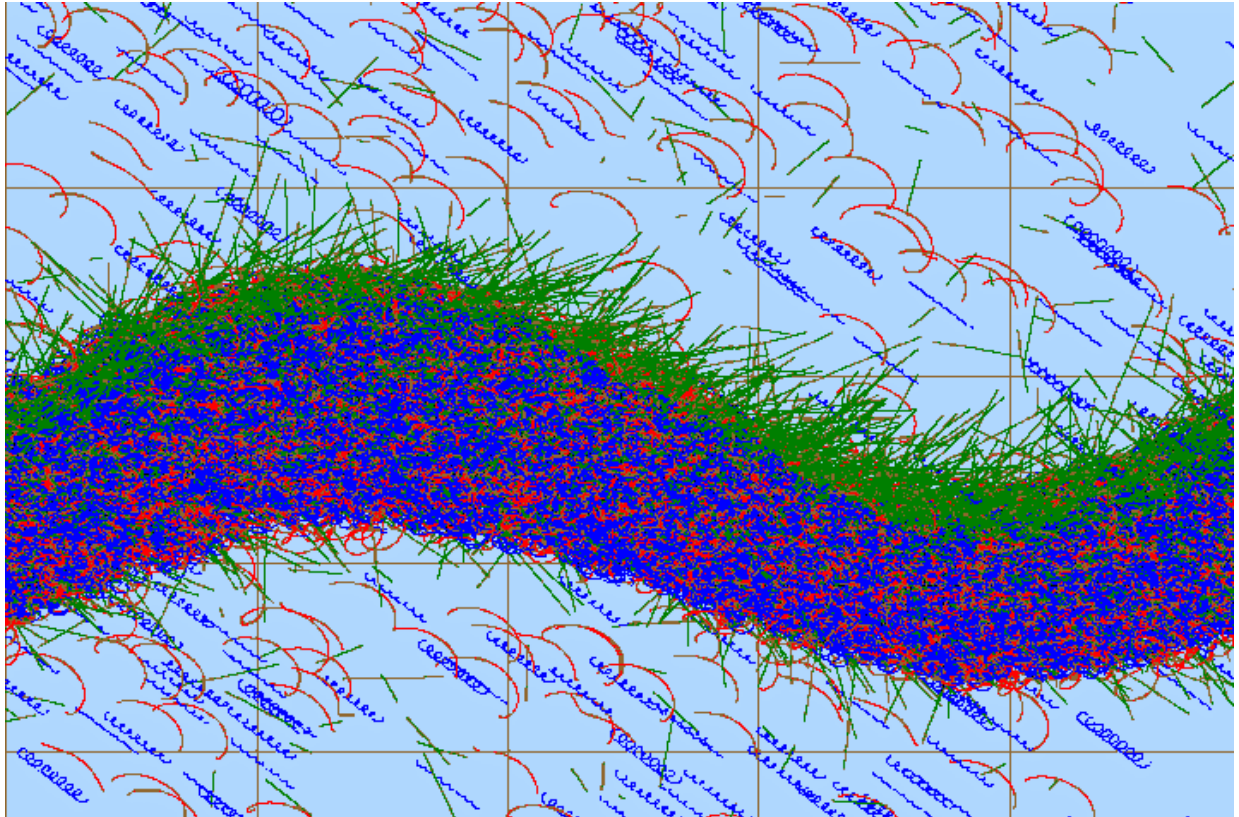


Fig. 13: Tests of the model. ExB drift motions, early stage, 10 000 particles.
Non-drifting neutrals remained in the top area.

Initial perturbations

Various initial perturbations of the beam shape can be performed: sausage, kink, small radial displacement of the electrons or ions (radial electric field perturbation), and axial current perturbation. Magnitude of the perturbations can be adjusted from the initial dialog window.

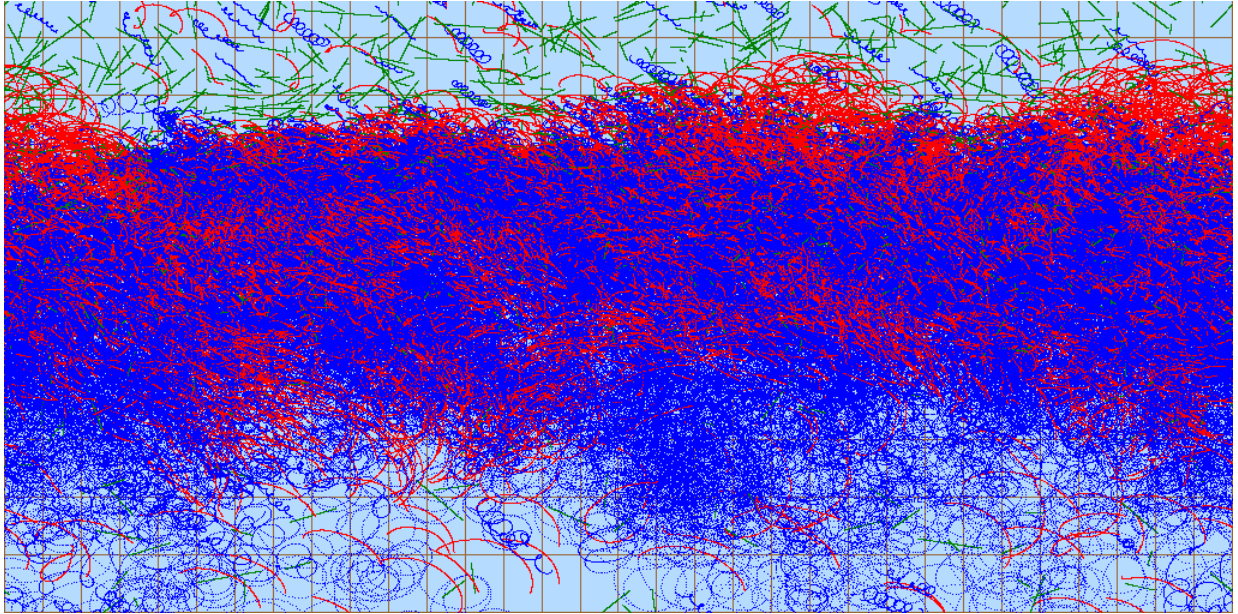


Fig. 14: Tests of the model. ExB drift motions, later stage, 10 000 particles.
Non-drifting neutrals remained in the top area.

2.4. Grid

We use orthogonal grid and functional periodicity $f(x_L) = f(x_R)$. Following one dimensional notation is used only for simplicity. The grid points are in the program identified in three different ways according to the field solver used (*basic*, *normal*, *multigrid*; the fields can be transferred between these descriptions via routines *trasform_bm* and *trasform_mb*):

Basic

X_L						X_R		$N \equiv N_{gridb}; \quad f_N = f_0,$
•	x	x	...	x	•			$\Delta x = (x_R - x_L) / N,$
0	1	2		N-1	N			$x_i = x_L + i * \Delta x; \quad i = 0, 1, \dots, N.$

Normal

X_L						X_R		$N \equiv N_{gridn}; \quad f_{N+1} = f_1,$
•	x	x	...	x	•			$\Delta x = (x_R - x_L) / N,$
1	2	3		N	N+1			$x_i = x_L + (i-1) * \Delta x; \quad i = 1, \dots, N+1.$

Multigrid

X_L						X_R		$N \equiv N_{gridm}; \quad f_N = f_1,$
•	x	x	...	x	•			$\Delta x = (x_R - x_L) / (N - 1),$
1	2	3		N-1	N			$x_i = x_L + (i-1) * \Delta x; \quad i = 1, \dots, N.$

In multigrid methods the number of the grid points must have a shape $N_{gridm} = k * 2^{n-1} + 1$.

If k is small prime (2 or 3) and n is much greater than k the method works most efficiently.

Practically, following combinations are possible:

Table 1: Possible grid dimensions for multigrid method

1)	$2 \times 2^1 + 1 = 5$	$k=2, n=2$
2)	$2 \times 2^2 + 1 = 9$	$k=2, n=3$
3)	$2 \times 2^3 + 1 = 17$	$k=2, n=4$
4)	$3 \times 2^3 + 1 = 25$	$k=3, n=4$
5)	$2 \times 2^4 + 1 = 33$	$k=2, n=5$
6)	$3 \times 2^4 + 1 = 49$	$k=3, n=5$
7)	$2 \times 2^5 + 1 = 65$	$k=2, n=6$
8)	$3 \times 2^5 + 1 = 97$	$k=3, n=6$

As the number of the grid points N_{gridp} is chosen, one calculates Δx and number of the points for other methods $N_{gridb} = N_{gridn} = N_{gridm} - 1$. The number of the grid points is in the program given by the value of quantity called grid granularity (GUI input, N_{gran} , 1st column of the Table above, 1 ... 8).

In FFT method the number of grid points must have shape $N_{gridb} = 2^{n-1} + 1$. Reasonable values are:

Table 2: Possible grid dimensions for FFT method

1)	$2 \times 2^1 + 1 = 5$	$n=2$
2)	$2 \times 2^2 + 1 = 9$	$n=3$
3)	$2 \times 2^3 + 1 = 17$	$n=4$
4)	$2 \times 2^4 + 1 = 33$	$n=5$
5)	$2 \times 2^5 + 1 = 65$	$n=6$

The left column in both tables is entered as granularity in the initial dialog window. Some of the values of both methods are the same. This fact can be used for comparison of the methods.

2.5. Nondimensional Variables

In all physical models nondimensional variables play exceptionally important role. In all the branches of science similar phenomena exist in very different dimensions. After introducing the nondimensional variables (if it is possible) we can treat plasma filaments in nebulas as well as in laboratory by the same model. The real dimensions are hidden in the transformation equations and some combinations of concentration, length, magnetic field, temperature and other plasma parameters yield the same solutions. In the PIC model the nondimensional variables according to the following table are used.

Table 3: Nondimensional PIC model variables

Time:	$\bar{t} \equiv t/t_0;$	$t_0 = \begin{cases} 1/\omega_c = m_e/Q_e B_{ext} & ; B_{ext} \neq 0; \\ m_e v_0 / Q_e E_{ext} & ; B_{ext} = 0; E_{ext} \neq 0; \\ 1 \mu s & ; B_{ext} = 0; E_{ext} = 0. \end{cases}$
Length:	$\bar{x} \equiv x/x_0;$	$x_0 = v_0 t_0.$
Velocity:	$\bar{\mathbf{v}} \equiv \mathbf{v}/v_0;$	$v_0 = (kT_0/m_e)^{1/2}.$
Temperature:	$\bar{T} \equiv T/T_0;$	$T_0 = 1 \text{ eV}.$
Magnetic field:	$\bar{B} \equiv B/B_0;$	$B_0 = m_e/Q_e t_0.$
Electric field:	$\bar{E} \equiv E/E_0;$	$E_0 = m_e v_0 / Q_e t_0.$
Charge:	$\bar{Q} \equiv Q/Q_0;$	$Q_0 = Q_e.$
Mass:	$\bar{m} \equiv m/m_0;$	$m_0 = m_e.$
Charge density:	$\bar{\rho} \equiv \rho/\rho_0;$	$\rho_0 = Q_e / x_0^3.$
Current density:	$\bar{\mathbf{J}} \equiv \mathbf{J}/J_0;$	$J_0 = Q_e / t_0 x_0^2.$
Scalar potential:	$\bar{\phi} \equiv \phi/\phi_0;$	$\phi_0 = E_0 x_0.$
Vector potential:	$\bar{\mathbf{A}} \equiv \mathbf{A}/A_0;$	$A_0 = B_0 x_0.$
Permittivity:	$\bar{\epsilon}_0 \equiv \epsilon_0/a;$	$a = Q_e / x_0^2 E_0 = Q_e^2 t_0^2 / m_e x_0^3.$
Permeability:	$\bar{\mu}_0 \equiv \mu_0/b;$	$b = m_e x_0 / Q_e^2.$
Speed of light:	$\bar{c} \equiv c/c_0;$	$c_0 = v_0;$ $\bar{c} = \frac{1}{\sqrt{\bar{\epsilon}_0 \bar{\mu}_0}}.$

Nondimensional particle equations

With the variable choice described above the particle equations of motion rewritten into the nondimensional variables preserve the same shape:

$$m_\alpha \frac{d\mathbf{v}_\alpha}{dt} = Q_\alpha [\mathbf{E} + \mathbf{v}_\alpha \times \mathbf{B}],$$
$$\frac{d\bar{\mathbf{v}}_\alpha}{d\bar{t}} = \frac{\bar{Q}_\alpha}{\bar{m}_\alpha} [\bar{\mathbf{E}} + \bar{\mathbf{v}}_\alpha \times \bar{\mathbf{B}}].$$

The case of relativistic equations of motion will be treated separately.

Nondimensional field equations:

The Maxwell equations maintain in the nondimensional variables its shape

$$\bar{\nabla} \cdot \bar{\mathbf{B}} = 0;$$
$$\bar{\nabla} \cdot \bar{\mathbf{E}} = \frac{\bar{\rho}}{\bar{\epsilon}_0};$$
$$\bar{\nabla} \times \bar{\mathbf{B}} = \bar{\mu}_0 \bar{\mathbf{J}} + \bar{\epsilon}_0 \bar{\mu}_0 \frac{\partial \bar{\mathbf{E}}}{\partial \bar{t}};$$
$$\bar{\nabla} \times \bar{\mathbf{E}} = - \frac{\partial \bar{\mathbf{B}}}{\partial \bar{t}},$$

as well as the Maxwell equations in the potentials (must be supplemented by the Lorentz condition):

$$\left(\bar{\Delta} - \bar{\epsilon}_0 \bar{\mu}_0 \frac{\partial^2}{\partial \bar{t}^2} \right) \bar{\phi} = - \frac{\bar{\rho}}{\bar{\epsilon}_0};$$
$$\left(\bar{\Delta} - \bar{\epsilon}_0 \bar{\mu}_0 \frac{\partial^2}{\partial \bar{t}^2} \right) \bar{\mathbf{A}} = - \bar{\mu}_0 \bar{\mathbf{J}};$$
$$\bar{\mathbf{E}} = - \bar{\nabla} \bar{\phi} - \frac{\partial \bar{\mathbf{A}}}{\partial \bar{t}}; \quad \bar{\mathbf{B}} = \bar{\nabla} \times \bar{\mathbf{A}}.$$

2.6. Nonrelativistic and Relativistic Particle Solvers

There are implemented several particle solvers in the model:

- Newton-Euler solver
- Leapfrog solver
- Runge-Kutta 4th order solver
- Boris-Buneman solver
- Canonical solver

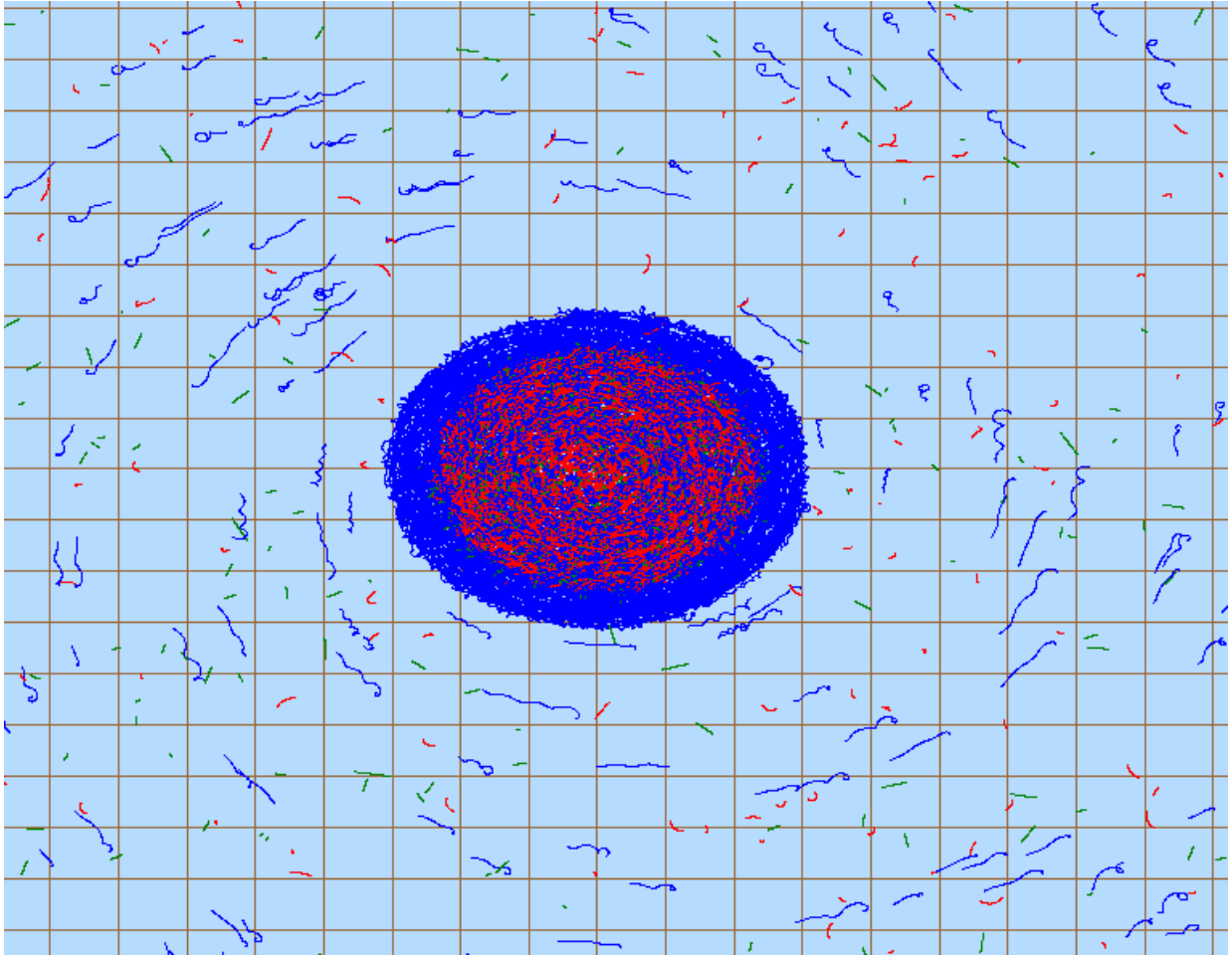


Fig. 15: Tests of the model. Radial charge perturbation and corresponding azimuthal drift.

Newton-Euler solver is very fast but doesn't follow theoretical solution ($\mathbf{E} \times \mathbf{B}$ drifts and other motions were tested) sufficiently exactly. In collision dominated plasma this needn't lead to serious problems because only small parts of Larmor orbits are realized. Other solvers follow the theoretical trajectory and no deviations were observed. The "canonical" scheme proposed in our department seems to be the fastest in the tests performed.

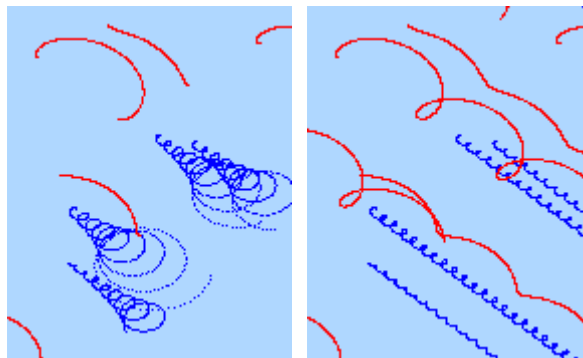


Fig. 16: Test of drift motions. Newton-Euler scheme (left), Boris-Buneman scheme (right). All the solvers behaved like Boris-Buneman solver with the exception of the Newton-Euler one.

Both non-relativistic and relativistic variants are incorporated in the model. In case of relativistic velocity of the particle the solver is automatically switched to relativistic one. The relativistic variants of all the schemes (with exception of the canonical one) were developed in frame of the Dan Škandera Diploma Thesis. Details can be found in [9]. Stability and convergence of the schemes were investigated as well.

In tests with 50 000 electrons and 50 000 ions moving under external electric and magnetic fields the CPU time for 200 differential steps was (PC, Celeron 333 MHz):

Table 4: CPU time of the schemes

Scheme	Nonrelativistic	Relativistic
Newton-Euler	14.8	33.5
Leapfrog	38.5	92.0
Runge-Kutta 4 th order	25.6	44.7
Boris-Buneman	21.5	45.7
Canonical	17.4	42.1

In the table only time of numerical calculations was included. With the exception of the first order Newton-Euler scheme the fastest is the Canonical scheme. The relativistic variants are approximately twice slower than nonrelativistic ones.

In relativistic case the main problem is that the velocity is on both sides of the Lorentz equation of motion:

$$\frac{d}{dt}(\gamma\mathbf{v}) = \frac{Q}{m_0} [\mathbf{E} + \mathbf{v} \times \mathbf{B}]; \quad \gamma \equiv \frac{1}{\sqrt{1 - v^2/c^2}}. \quad (4)$$

Using substitution

$$\mathbf{u} \equiv \gamma\mathbf{v}, \quad (5)$$

the Lorentz equation of motion can be rewritten into form

$$\frac{d\mathbf{u}}{dt} = \frac{Q}{m_0} \left[\mathbf{E} + \frac{\mathbf{u}}{\gamma} \times \mathbf{B} \right]; \quad \gamma = \sqrt{1 + \frac{\mathbf{u}^2}{c^2}}. \quad (6)$$

Equation (6) can be simply used for the construction of the numerical schemes.

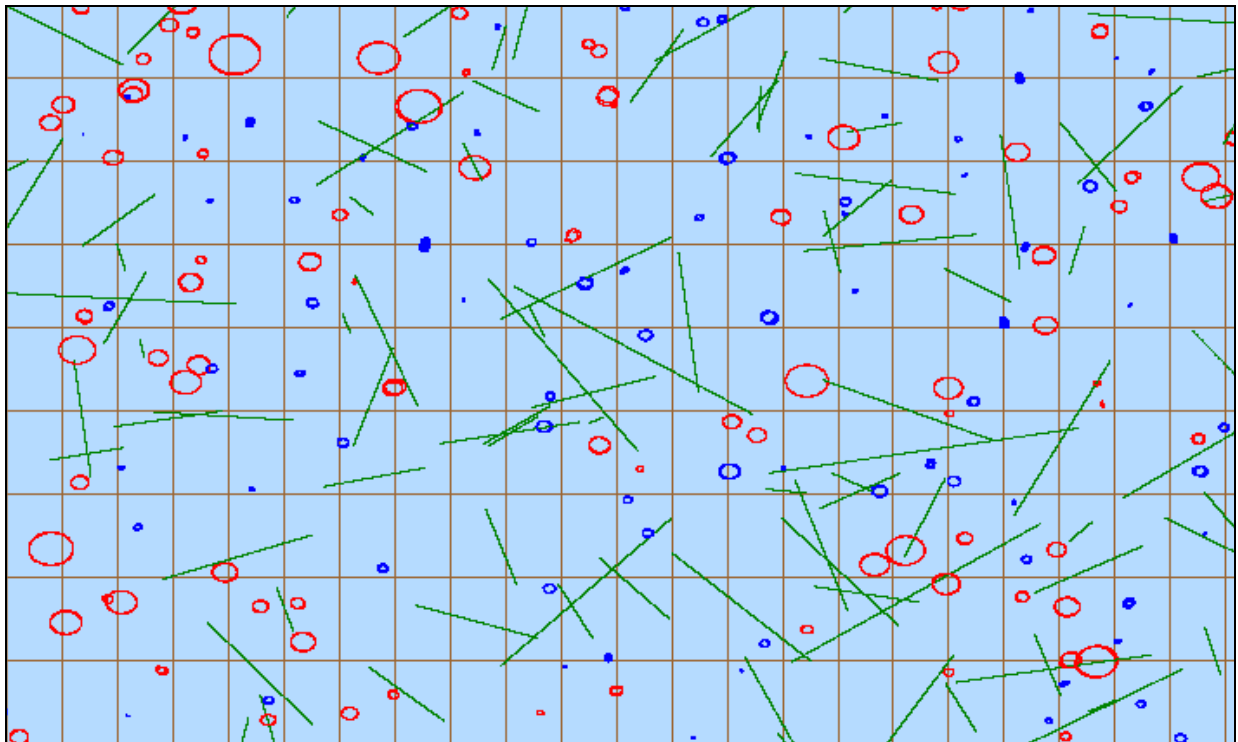
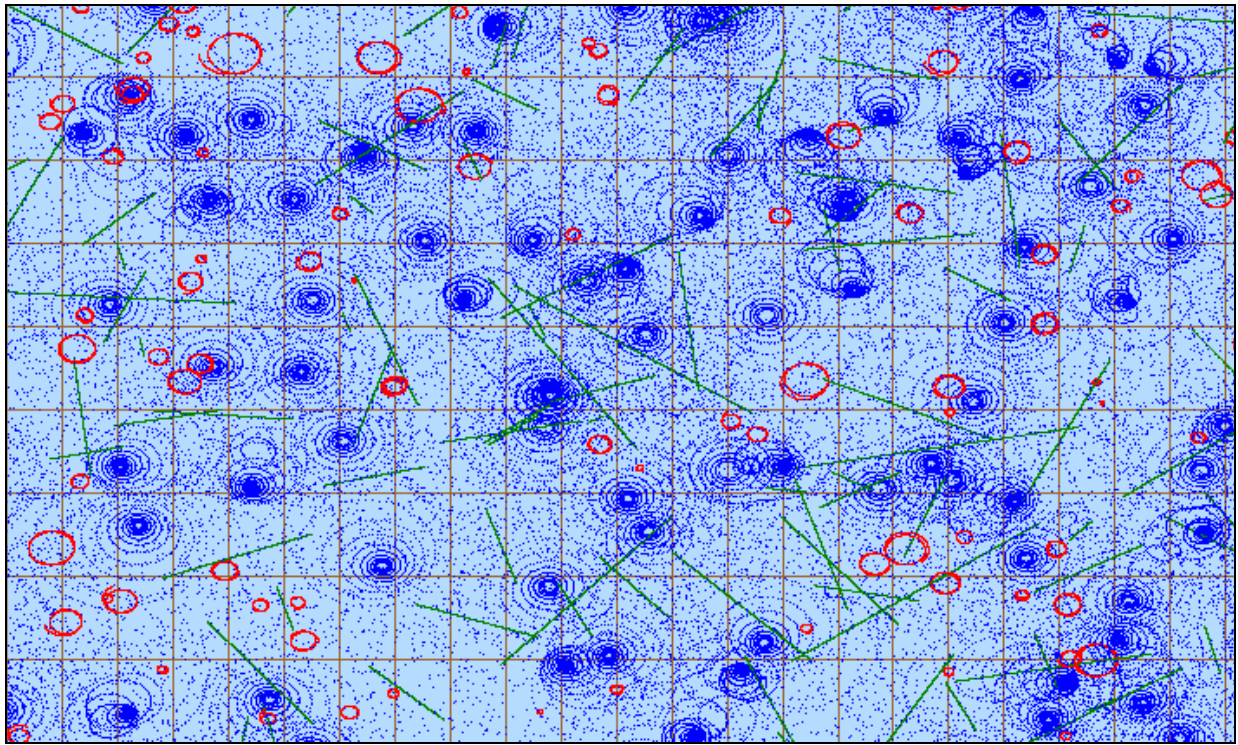


Fig. 17: Simple test of motion in magnetic field. Newton-Euler solver (top) and Canonical solver (bottom). Number of steps: 1000, electrons: blue, ions: red, neutrals: green, $m_i/m_e=8$. The inaccuracy of the NE scheme is evident.

Table 5: Non-relativistic particle solvers

<p><i>Newton-Euler scheme:</i></p>	$\tilde{\mathbf{E}} = \frac{Q\Delta t}{m} \mathbf{E} ; \quad \tilde{\mathbf{B}} = \frac{Q\Delta t}{m} \mathbf{B} ,$ $\mathbf{v}_{n+1} = \mathbf{v}_n + \tilde{\mathbf{E}} + \mathbf{v}_n \times \tilde{\mathbf{B}} ,$ $\mathbf{x}_{n+1} = \mathbf{x}_n + \frac{(\mathbf{v}_{n+1} + \mathbf{v}_n)}{2} \Delta t .$
<p><i>Leapfrog scheme:</i></p>	$\tilde{\mathbf{E}} \equiv \frac{Q\Delta t}{m} \mathbf{E} , \quad \tilde{\mathbf{B}} \equiv \frac{Q}{m} \frac{\Delta t}{2} \mathbf{B} ;$ $\tilde{\mathbf{v}} = \mathbf{v}_{n-1/2} + \tilde{\mathbf{E}} + \mathbf{v}_{n-1/2} \times \tilde{\mathbf{B}} ,$ $\mathbf{v}_{n+1/2} = \tilde{\mathbf{v}} + \frac{(\tilde{\mathbf{v}} + \tilde{\mathbf{v}} \times \tilde{\mathbf{B}}) \times \tilde{\mathbf{B}}}{1 + \tilde{\mathbf{B}}^2} ,$ $\mathbf{x}_{n+1} = \mathbf{x}_n + \mathbf{v}_{n+1/2} \Delta t .$
<p><i>Runge-Kutta 4th order scheme:</i></p>	$\tilde{\mathbf{E}} \equiv \frac{Q}{m} \frac{\Delta t}{2} \mathbf{E} , \quad \tilde{\mathbf{B}} \equiv \frac{Q}{m} \frac{\Delta t}{2} \mathbf{B} ;$ $\mathbf{K}_1 = \mathbf{v}_n , \quad \mathbf{L}_1 = \tilde{\mathbf{E}} + \mathbf{v}_n \times \tilde{\mathbf{B}} ;$ $\mathbf{K}_2 = \mathbf{v}_n + \mathbf{L}_1 , \quad \mathbf{L}_2 = \tilde{\mathbf{E}} + \mathbf{K}_2 \times \tilde{\mathbf{B}} ;$ $\mathbf{K}_3 = \mathbf{v}_n + \mathbf{L}_2 , \quad \mathbf{L}_3 = \tilde{\mathbf{E}} + \mathbf{K}_3 \times \tilde{\mathbf{B}} ;$ $\mathbf{K}_4 = \mathbf{v}_n + 2\mathbf{L}_3 , \quad \mathbf{L}_4 = \tilde{\mathbf{E}} + \mathbf{K}_4 \times \tilde{\mathbf{B}} ;$ $\mathbf{x}_{n+1} = \mathbf{x}_n + (\mathbf{K}_1 + 2\mathbf{K}_2 + 2\mathbf{K}_3 + \mathbf{K}_4) \Delta t / 6 ,$ $\mathbf{v}_{n+1} = \mathbf{v}_n + (\mathbf{L}_1 + 2\mathbf{L}_2 + 2\mathbf{L}_3 + \mathbf{L}_4) / 3 .$
<p><i>Boris-Buneman scheme:</i></p>	$\tilde{\mathbf{E}} \equiv \frac{Q}{m} \frac{\Delta t}{2} \mathbf{E} , \quad \tilde{\mathbf{B}} \equiv \frac{Q}{m} \frac{\Delta t}{2} \mathbf{B} ;$ $\tilde{\mathbf{v}} = \mathbf{v}_n + \tilde{\mathbf{E}} ,$ $\tilde{\tilde{\mathbf{v}}} = \tilde{\mathbf{v}} + 2 \frac{(\tilde{\mathbf{v}} + \tilde{\mathbf{v}} \times \tilde{\mathbf{B}}) \times \tilde{\mathbf{B}}}{1 + \tilde{\mathbf{B}}^2} ,$ $\mathbf{v}_{n+1} = \tilde{\tilde{\mathbf{v}}} + \tilde{\mathbf{E}} ,$ $\mathbf{x}_{n+1} = \mathbf{x}_n + \mathbf{v}_{n+1} \Delta t .$
<p><i>Canonical scheme:</i></p>	$\tilde{\mathbf{E}} \equiv \frac{Q\Delta t}{m} \mathbf{E} , \quad \tilde{\mathbf{B}} \equiv \frac{Q\Delta t}{m} \mathbf{B} ;$ $\tilde{\mathbf{v}} = \mathbf{v}_n + \frac{\mathbf{v}_n \times \tilde{\mathbf{B}}}{2} ,$ $\mathbf{x}_{n+1} = \mathbf{x}_n + \tilde{\mathbf{v}} \Delta t ,$ $\mathbf{v}_{n+1} = \mathbf{v}_n + \tilde{\mathbf{E}} + \tilde{\mathbf{v}} \times \tilde{\mathbf{B}} .$

Newton-Euler scheme (NE)

In the Newton scheme the derivatives are simply replaced with time advanced differences. Resulting scheme is as follows:

$$\begin{aligned}\gamma_n &= 1/\sqrt{1-\mathbf{v}_n^2/c^2}; \\ \tilde{\mathbf{E}} &= \frac{Q\Delta t}{m_0} \mathbf{E}; \quad \tilde{\mathbf{B}} = \frac{Q\Delta t}{m_0 \gamma_n} \mathbf{B}; \\ \mathbf{u}_n &= \gamma_n \mathbf{v}_n; \\ \mathbf{u}_{n+1} &= \mathbf{u}_n + \tilde{\mathbf{E}} + \mathbf{u}_n \times \tilde{\mathbf{B}}; \\ \mathbf{v}_{n+1} &= \frac{\mathbf{u}_{n+1}}{\sqrt{1+\mathbf{u}_{n+1}^2/c^2}}; \\ \mathbf{x}_{n+1} &= \mathbf{x}_n + \frac{\mathbf{v}_{n+1} + \mathbf{v}_n}{2} \Delta t.\end{aligned}$$

From the third equation we calculate from old values the substituted variable \mathbf{u} . Next from the equation of motion (6) the new value of \mathbf{u} is obtained. According to the substitution (5) it is transformed to the new value of \mathbf{v} . Last step is the calculation of new position from $\mathbf{v} = d\mathbf{x}/dt$. As both new and old values of \mathbf{v} are known, central difference could be used. The scheme is relatively fast, but local discretization error is of the order $O(\Delta t)$.

Leapfrog scheme (LF)

In Leapfrog scheme the positions and velocities are calculated in times shifted about $\Delta t/2$. This ensures local discretization error of the order $O((\Delta t)^2)$. Time differences are centered and it results in implicit scheme

$$\mathbf{u}_{n+1/2} = \mathbf{u}_{n-1/2} + \frac{Q}{m_0} \left(\mathbf{E} + \frac{\mathbf{u}_{n-1/2} + \mathbf{u}_{n+1/2}}{2\gamma_n} \times \mathbf{B} \right) \Delta t,$$

which can be solved analytically either by matrix method or by decomposition into longitudinal and perpendicular part (with respect to the magnetic field). The details are given in [64]. The final form of the LF scheme is

$$\begin{aligned}\gamma_n &= 1/\sqrt{1-\mathbf{v}_n^2/c^2}; \\ \tilde{\mathbf{E}} &\equiv \frac{Q\Delta t}{m_0} \mathbf{E}, \quad \tilde{\mathbf{B}} \equiv \frac{Q}{m_0} \frac{\Delta t}{2\gamma_n} \mathbf{B};\end{aligned}$$

$$\mathbf{u}_{n-1/2} = \frac{\mathbf{v}_{n-1/2}}{\sqrt{1 - \mathbf{v}_{n-1/2}^2 / c^2}};$$

$$\tilde{\mathbf{u}} = \tilde{\mathbf{u}}_{n-1/2} + \tilde{\mathbf{E}} + \tilde{\mathbf{u}}_{n-1/2} \times \tilde{\mathbf{B}};$$

$$\mathbf{u}_{n+1/2} = \tilde{\mathbf{u}} + \frac{[\tilde{\mathbf{u}} + \tilde{\mathbf{u}} \times \tilde{\mathbf{B}}] \times \tilde{\mathbf{B}}}{1 + \tilde{\mathbf{B}}^2};$$

$$\mathbf{x}_{n+1} = \mathbf{x}_n + \frac{\mathbf{u}_{n+1/2}}{\gamma_{n+1/2}} \Delta t.$$

Runge-Kutta scheme (RK)

Runge-Kutta is the standard solver for ordinary differential equations. It has fourth order accuracy and excellent results. The time consumption can be reduced by longer time interval (while the accuracy is prolonged on the same level as compared with other schemes). The relativistic analogue is

$$\gamma_n = 1 / \sqrt{1 - \mathbf{v}_n^2 / c^2};$$

$$\tilde{\mathbf{E}} \equiv \frac{Q}{m} \frac{\Delta t}{2} \mathbf{E}, \quad \tilde{\mathbf{B}} \equiv \frac{Q}{m} \frac{\Delta t}{2} \mathbf{B},$$

$$\mathbf{u}_n = \gamma_n \mathbf{v}_n;$$

$$\mathbf{K}_1 = \frac{\mathbf{u}_n}{\gamma_n}, \quad \mathbf{L}_1 = \tilde{\mathbf{E}} + \mathbf{K}_1 \times \tilde{\mathbf{B}},$$

$$\mathbf{K}_2 = \frac{\mathbf{u}_n + \mathbf{L}_1}{\gamma_{K_2}}, \quad \mathbf{L}_2 = \tilde{\mathbf{E}} + \mathbf{K}_2 \times \tilde{\mathbf{B}},$$

$$\mathbf{K}_3 = \frac{\mathbf{u}_n + \mathbf{L}_2}{\gamma_{K_3}}, \quad \mathbf{L}_3 = \tilde{\mathbf{E}} + \mathbf{K}_3 \times \tilde{\mathbf{B}},$$

$$\mathbf{K}_4 = \frac{\mathbf{u}_n + 2\mathbf{L}_3}{\gamma_{K_4}}, \quad \mathbf{L}_4 = \tilde{\mathbf{E}} + \mathbf{K}_4 \times \tilde{\mathbf{B}},$$

$$\mathbf{x}_{n+1} = \mathbf{x}_n + \frac{1}{6} \Delta t (\mathbf{K}_1 + 2\mathbf{K}_2 + 2\mathbf{K}_3 + \mathbf{K}_4),$$

$$\mathbf{u}_{n+1} = \mathbf{u}_n + \frac{1}{3} (\mathbf{L}_1 + 2\mathbf{L}_2 + 2\mathbf{L}_3 + \mathbf{L}_4),$$

$$\mathbf{v}_{n+1} = \frac{\mathbf{u}_{n+1}}{\sqrt{1 + \mathbf{u}_{n+1}^2 / c^2}},$$

where γ_{K_i} is the gamma factor determined from the numerator of the K_i fraction.

Boris–Buneman scheme (BB)

In the Boris-Buneman scheme first of all one half of the electric field acceleration is performed ($\tilde{\mathbf{u}}$), followed by Larmor rotation in magnetic field ($\tilde{\tilde{\mathbf{u}}}$) and completed by the second half of the electric field acceleration (\mathbf{u}_{n+1}). BB scheme is very fast solver suitable for plasma calculations [7, 10]. Simple relativistic generalization can be used for relativistic plasma. Resulting scheme is (details are in [64, 70])

$$\begin{aligned}\gamma_n &= 1/\sqrt{1-\mathbf{v}_n^2/c^2}; \\ \tilde{\mathbf{E}} &\equiv \frac{Q}{m_0} \frac{\Delta t}{2} \mathbf{E}, \quad \tilde{\mathbf{B}} \equiv \frac{Q}{m_0} \frac{\Delta t}{2\gamma_n} \mathbf{B}; \\ \mathbf{u}_n &= \gamma_n \mathbf{v}_n; \\ \tilde{\mathbf{u}} &= \mathbf{u}_n + \tilde{\mathbf{E}}; \\ \tilde{\tilde{\mathbf{u}}} &= \tilde{\mathbf{u}} + 2 \frac{(\tilde{\mathbf{u}} + \tilde{\mathbf{u}} \times \tilde{\mathbf{B}}) \times \tilde{\mathbf{B}}}{1 + \tilde{\mathbf{B}}^2}; \\ \mathbf{u}_{n+1} &= \tilde{\tilde{\mathbf{u}}} + \tilde{\mathbf{E}}; \\ \mathbf{v}_{n+1} &= \frac{\mathbf{u}_{n+1}}{\sqrt{1 + \mathbf{u}_{n+1}^2/c^2}}; \\ \mathbf{x}_{n+1} &= \mathbf{x}_n + \mathbf{v}_{n+1} \Delta t.\end{aligned}$$

Canonical scheme (CN)

The canonical scheme [53, 55] is very simple and efficient, it was derived on the basis of Hamilton canonical equations with canonical momentum containing local vector potential $\mathbf{A} = \mathbf{r} \times \mathbf{B}/2$. The relativistic variant of the scheme follows:

$$\begin{aligned}\gamma_n &= 1/\sqrt{1-\mathbf{v}_n^2/c^2}; \\ \tilde{\mathbf{E}} &\equiv \frac{Q\Delta t}{m_0} \mathbf{E}, \quad \tilde{\mathbf{B}} \equiv \frac{Q}{m_0} \frac{\Delta t}{\gamma_n} \mathbf{B}; \\ \mathbf{u}_n &= \gamma_n \mathbf{v}_n; \\ \tilde{\mathbf{u}} &= \mathbf{u}_n + \frac{\mathbf{u}_n \times \tilde{\mathbf{B}}}{2}; \\ \mathbf{u}_{n+1} &= \mathbf{u}_n + \tilde{\mathbf{E}} + \tilde{\mathbf{u}} \times \tilde{\mathbf{B}}; \\ \mathbf{v}_{n+1} &= \frac{\mathbf{u}_{n+1}}{\sqrt{1 + \mathbf{u}_{n+1}^2/c^2}}; \\ \mathbf{x}_{n+1} &= \mathbf{x}_n + \frac{\tilde{\mathbf{u}} \Delta t}{\gamma_n}.\end{aligned}$$

This scheme was proposed in our department. It is very fast and provides excellent results.

The computation of particle trajectories adapts to the physical situation. In case of relativistic velocity of the particle the solver is switched to the relativistic one; if the time step is not sufficiently fine, it is refined immediately.

2.7. Weighting Particles and Fields

Particle positions and velocities must be weighted into the grid points, where they represent source terms of the Maxwell equations for the electric and magnetic fields. After the weighting, charge and current densities must be known in all grid points. Zero and first order weighting had been implemented in the model:

Zero order weighting

Zero order weighting represents standard PIC (Particle in Cell) or NGP (Nearest Grid Point) method. The particle attribute - charge or velocity - is assigned to the nearest grid point. This scheme is very fast, but passage of the particle near the grid point is discontinuous and may cause some numerical problems.

First order weighting

This method is mostly referred as CIC (Cloud in Cell). Particles are weighted to the 8 nearest cell points (4 in 2D) according to the “opposite” volumes (areas in 2D). The passage of the particle near a grid point is continuous (but not the first derivative) and particle behaves like a cloud of particles of the same sign. This type of weighting is used very often because numerical problems connected with discontinuities are eliminated and it is fast enough in comparison with higher order types of the weighting.

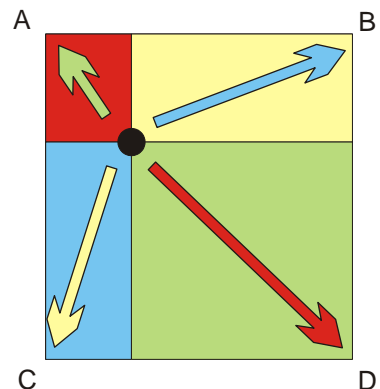


Fig. 18: Example of 2D weighting procedure. Particle is weighted proportionally to the area in the neighborhood of the opposite corner.

Higher order weighting

The passage of the particle near a grid point is smooth, but the computational time required is enormous. That is why the higher order weighting have not been implemented into the model. Weighting fields from the grid points to the particles must have the same order as weighting particles to the grid. In other case numerical problems could occur.

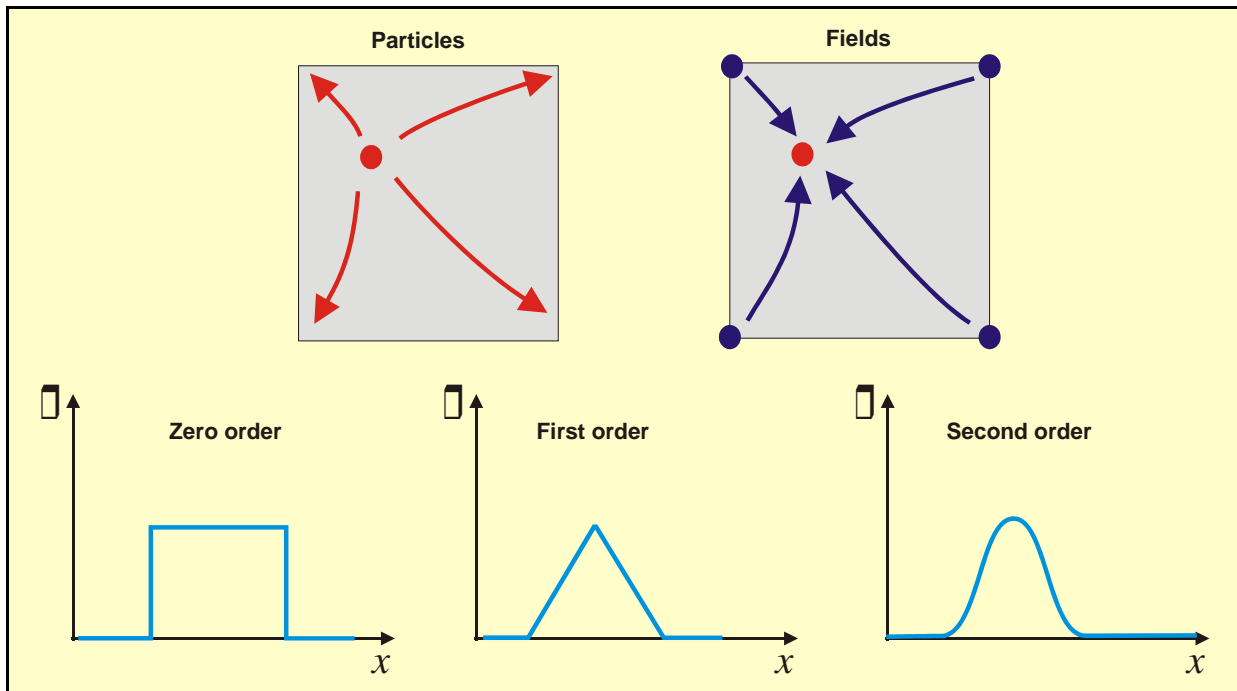


Fig. 19: Example of 2D weighting procedure. Observer in a grid point would feel the charge density of particle passing nearby according to the curves presented.

2.8. Field Solvers

There are implemented two field solvers in the model nowadays. The time evolution is treated as explicit via methods based on similar considerations as in the Boris-Buneman particle scheme [7]. Electric and magnetic fields are calculated separately from Laplace–Poisson equations. In the same manner can be treated gravitational field acting on dust particles. Subsequently time field step follows.

FFT solver for Laplace-Poisson equation

The FFT solver for the Laplace-Poisson equation was developed by Radim Dejmek (FEE CTU student) in frame of his diploma thesis [57]. It is based on standard libraries modified to our purposes. Finite properties of the grid are involved in the Laplace differential operator in the \mathbf{k} space.

The algorithm consists from five basic steps:

1. Discretization of the Laplace-Poisson equation,
2. Discrete Fourier transform of the equation,
3. Algebraic solution of the equation in \mathbf{k} space,

4. Inverse DFT, retrieval of the potential,
5. Calculations of the fields in the grid points from the potentials.

Let us explain these steps on the Laplace–Poisson equation for the electric field potential

$$\Delta\varphi = -\frac{\rho}{\varepsilon_0}. \quad (7)$$

The discretization of this equation can be for example done as (via central differences)

$$\begin{aligned} \frac{\Delta_x^2\varphi}{(\Delta x)^2} + \frac{\Delta_y^2\varphi}{(\Delta y)^2} + \frac{\Delta_z^2\varphi}{(\Delta z)^2} &= -\frac{\rho_{n_1,n_2,n_3}}{\varepsilon_0}; \\ \frac{\Delta_x^2\varphi}{(\Delta x)^2} &\equiv \frac{\varphi_{n_1+1,n_2,n_3} - 2\varphi_{n_1,n_2,n_3} + \varphi_{n_1-1,n_2,n_3}}{(\Delta x)^2}, \\ \frac{\Delta_y^2\varphi}{(\Delta y)^2} &\equiv \frac{\varphi_{n_1,n_2+1,n_3} - 2\varphi_{n_1,n_2,n_3} + \varphi_{n_1,n_2-1,n_3}}{(\Delta y)^2}, \\ \frac{\Delta_z^2\varphi}{(\Delta z)^2} &\equiv \frac{\varphi_{n_1,n_2,n_3+1} - 2\varphi_{n_1,n_2,n_3} + \varphi_{n_1,n_2,n_3-1}}{(\Delta z)^2}. \end{aligned} \quad (8)$$

The Discrete Fourier Transform (DFT) of the function F and the Inverse Discrete Fourier Transform (IDFT) are done by the formulas

$$\begin{aligned} \tilde{F}(k_1, k_2, k_3) &= \frac{1}{N_1 N_2 N_3} \sum_{n_1=0}^{N_1-1} \sum_{n_2=0}^{N_2-1} \sum_{n_3=0}^{N_3-1} F(n_1, n_2, n_3) \exp\left[2\pi i \left(\frac{k_1 n_1}{N_1} + \frac{k_2 n_2}{N_2} + \frac{k_3 n_3}{N_3}\right)\right]; \\ F(n_1, n_2, n_3) &= \sum_{k_1=0}^{N_1-1} \sum_{k_2=0}^{N_2-1} \sum_{k_3=0}^{N_3-1} \tilde{F}(k_1, k_2, k_3) \exp\left[-2\pi i \left(\frac{k_1 n_1}{N_1} + \frac{k_2 n_2}{N_2} + \frac{k_3 n_3}{N_3}\right)\right]. \end{aligned} \quad (9)$$

Application of the DFT on the equation (8) leads to the Laplace-Poisson equation in the \mathbf{k} space:

$$\left[\frac{4N_1^2}{L_x^2} \sin^2 \frac{\pi k_1}{N_1} + \frac{4N_2^2}{L_y^2} \sin^2 \frac{\pi k_2}{N_2} + \frac{4N_3^2}{L_z^2} \sin^2 \frac{\pi k_3}{N_3} \right] \tilde{\varphi}(k_1, k_2, k_3) = \frac{\tilde{\rho}(k_1, k_2, k_3)}{\varepsilon_0}. \quad (10)$$

Let us remark, that Fourier Transform for continuous variables would give $k^2 \tilde{\varphi} = \tilde{\rho}/\varepsilon_0$. The “sinuses” in the result are caused by the influence of the grid. Algebraic solution of this equation is very simple:

$$\tilde{\varphi}(k_1, k_2, k_3) = \frac{\tilde{\rho}(k_1, k_2, k_3)}{\varepsilon_0 \left[\frac{4N_1^2}{L_x^2} \sin^2 \frac{\pi k_1}{N_1} + \frac{4N_2^2}{L_y^2} \sin^2 \frac{\pi k_2}{N_2} + \frac{4N_3^2}{L_z^2} \sin^2 \frac{\pi k_3}{N_3} \right]}. \quad (11)$$

Inverse Discrete Fourier Transform IDFT yields the searched potential in the grid points

$$\varphi = \text{IDFT}(\tilde{\varphi}). \quad (12)$$

Knowing the potential we can calculate electric fields in the grid points. The DFT algorithm is time consuming; the number of operations is proportional N^2 , N being the number of points. Instead of the DFT is usually used the FFT algorithm with the number of operations reduced by the DIT or DIF method to be proportional only to $N \log N$. The FFT and IFFT routines were adapted from the commercial CMXL library distributed by the Compaq Company. During the first call of the FFT procedure a table of sinuses is calculated. The values from this table are used during subsequent calls of the procedure. If it is possible, computational time is minimized.

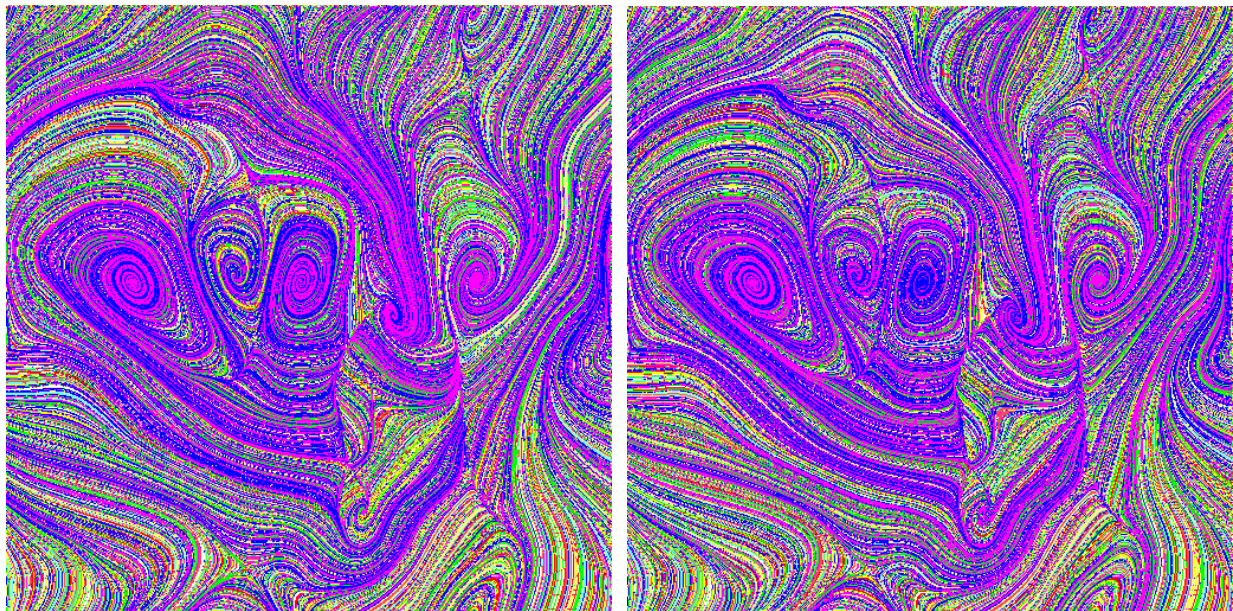


Fig. 20: Comparison of the FFT (left) and Multigrid (right) solver. On the figure is longitudinal filament cross section of the magnetic field for the grid $17 \times 17 \times 17$ and 10 000 particles. In the same situation magnetic field was calculated by both methods. The field lines are very similar, almost identical.

Multigrid solver

The alternative algorithm to the FFT in the PIC package is the Multigrid one. Multigrid iteration combines classical iterative techniques, such as Gauss-Seidel line or point relaxation, with adaptive multilevel grid structure and subgrid refinement procedures to yield a method superior to the iterative techniques alone. By iterating and transferring approximations and

corrections at subgrid levels, a good initial guess and rapid convergence at the fine grid level can be achieved. Multigrid iteration requires less storage and computation than direct methods for nonseparable elliptic partial differential equations and is competitive with direct methods such as cyclic reduction for separable equations. In particular, three-dimensional problems can often be handled at reasonable computational cost.

The multigrid solver package MUDPACK 5 developed in the UCAR (University Corporation for Atmospheric Research) was used. It can be obtained on the URL: <http://www.scd.ucar.edu/css/software/mudpack>. The solver is very fast, was written in FORTRAN 90 and it was without serious problems adapted to our needs. Author of the package is John C. Adams (National Center for Atmospheric Research, e-mail: johnad@ucar.edu) [47]. In multigrid methods the number of the grid points in arbitrary dimension must have shape $N = k * 2^{n-1} + 1$. The method works most efficiently if k is small prime (2 or 3) and n is much greater than k .

The author of the MUDPACK 5 package presents it in these words:

“MUDPACK is a collection of vectorized portable Fortran 77/90 subprograms which efficiently solve linear elliptic Partial Differential Equations (PDEs) using multigrid iteration. OpenMP directives are used in the latest version to enable shared memory parallelism. The package was created to make multigrid iteration available in user friendly form. The software is written in much the same format as the separable elliptic PDE package. It extends the domain of solvable problems to include both separable and nonseparable PDEs.”

Both methods (FFT and Multigrid) yield very similar results, see Fig. 20. For some parameters of the plasma simulation the FFT solver is faster, for other the Multigrid one.

3. PIC PACKAGE ADD-INS

3.1. Field Visualization - LIC

Program package VISUAL

A special program package based on Qt and OpenGL libraries was developed for the particle and field visualization in frame of O. Novak Diploma Thesis [56]. The program is easily portable and can be compiled both on Microsoft Windows and Linux systems.

The Qt library is developed by the Norwegian Company TrollTex. This multiplatform library is designated for working with Graphical User Interface (GUI) of operational systems. The library is offered as freeware for noncommercial usage on the LINUX platform and as a paid professional version for MS Windows platform. The Qt library gives unified programmer's interface based on C++ language, which is completely portable between both platforms. The communication between objects is based on unique *signal/slot* mechanism (this mechanism distinguishes this library from other similar libraries).

The OpenGL library was developed by Silicon Graphics Company. From 1992 it is an open standard independent on hardware environment. OpenGL represents integrated layer between the programmer and the display hardware. The display hardware is required to have frame buffer. The application interface includes about 120 commands for creating objects and manipulating them. The basic functions are: display of the line, triangle and polygon (3D); 2D image manipulation; work with textures; work with light including lighting the scene; creation of the mist; calculation of the objects visibility; work with the alpha channel; graphical transformations.

Data file

The PIC model output is written into file with extension .dpc (define plasma cube). The data are written in frames. One frame is a snapshot of the plasma filament situation including particle positions and velocities and electric and magnetic field values at the grid points.

The file format is line oriented sequential ASCII (for good portability), all the data records are separated by EOL (End of Line) character.

The file consists of two parts, the *head* and the *body*. First line of the head is free text and it is not retrieved by the program. Basic information about the model parameters is in the second line.

The body of the file is separated by key statements @FRAME, @PARTICLE and @FIELD into subparts. Key statement @FRAME starts new frame, following data will be incorporated into this frame. The key statement @PARTICLE starts a block of data with information about the particle positions and velocities. Parameters of this statement define the kind of particles and color for their visualization. The key statement @FIELD starts a block of field data (field values in the grid points). The parameter of the statement specifies the kind of the field (electric or magnetic).

The data file *.dpc serves as input file for the program package VISUAL.

Field lines calculation

The vector field (electric or magnetic) is visualized in cross section planes parallel with coordinate lattice. That means two-dimensional vectors located on the two-dimensional grid have to be visualized.

The cross section can be realized in arbitrary place of the rectangular parallelepiped. The vector values in the grid points are calculated by linear interpolation from neighboring grid planes:

$$\mathbf{F} = \mathbf{F}_A + (\mathbf{F}_B - \mathbf{F}_A) t; \quad t = \frac{s(X) - s(A)}{s(B) - s(A)}, \quad (13)$$

where s denotes the location of the point in the calculated coordinate (x, y, z) .

For the field line calculation we have to know the vector value in arbitrary location of the two-dimensional grid in the cross section plane. It is determined by bilinear interpolation algorithm (two consequent linear interpolations). The field line itself is calculated by Runge-Kutta numerical integrator of the fourth order [38]. The step of the integration is dynamically changed to ensure preservation of small details inside homogeneous areas.

LIC visualization

The LIC (Line Integral Convolution) method of the field visualization reminiscent the well-known experiment with permanent magnet and iron filings. After shaking, the fillings form itself along the magnetic field lines.

The LIC method has two inputs: the vector field $\mathbf{F}: \mathbf{R}^2 \rightarrow \mathbf{R}^2$ and noise texture represented by noise function T [8]. The noise texture is locally blurred along the field lines and the resulting output picture matches the structure of the field.

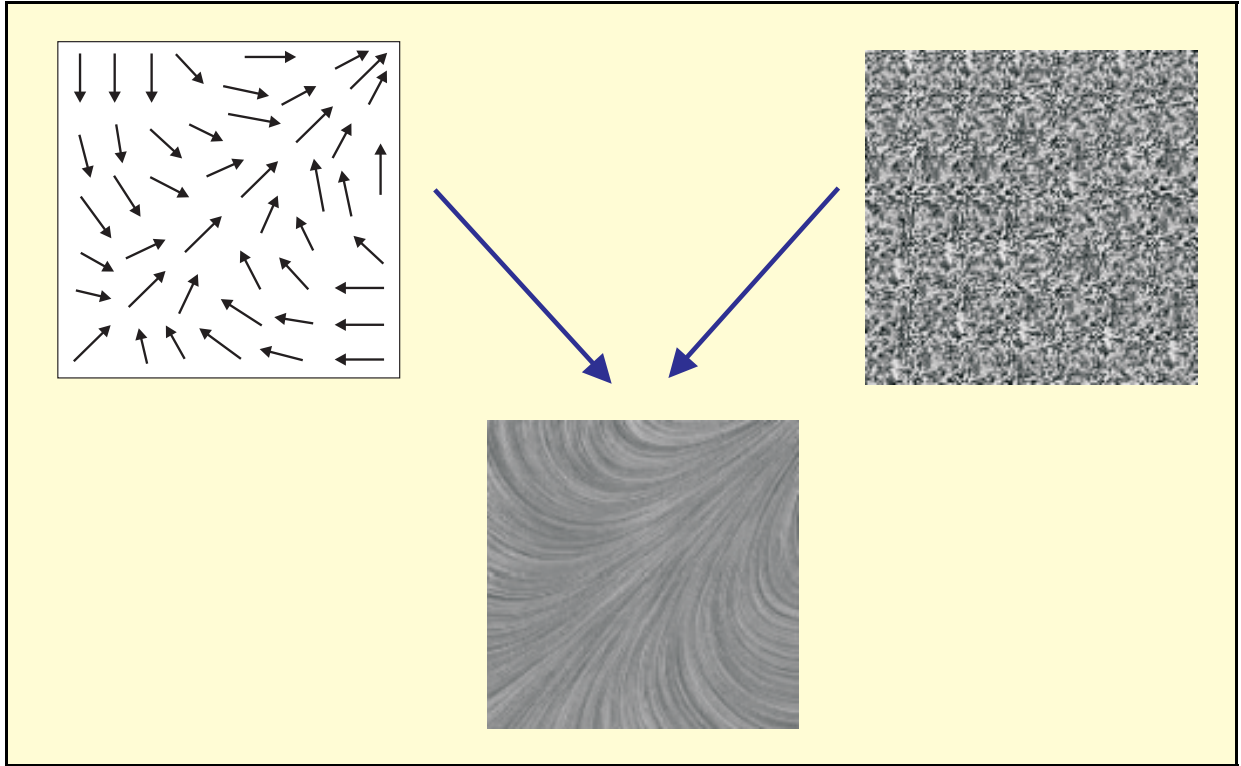


Fig. 21: The principle of the LIC method. The vector field lines are convoluted with the noise texture.

From the mathematical point of view the procedure of the blurring is implementation of the convolution integral

$$I(x_0) = \int_{s_0-L}^{s_0+L} k(s-s_0)T(\sigma(s))ds. \quad (14)$$

In the integral $I(x_0)$ is the intensity of the point $x_0 = \sigma(s_0)$, where $\sigma(s)$ is the field line parameterized by its length s . The convolution kernel k is one-dimensional and has length $2L$. The kernel is normalized to 1.

The convolution procedure creates highly correlated pixels along the field line, while the pixels in perpendicular direction are not correlated. The convolution integral has to be calculated for each pixel at least once. Some enhancement of the method published Hedge and Stalling. As the coherence is sufficient on long distances along the line, it is possible to calculate the convolution integral only for the first point of the field line and for subsequent pixels only changes of the integral can be calculated. This method was named *Fast LIC* [38].

In the implemented LIC method the algorithm of generating the RGB colors was modified. The details are described in [56]. As the colors have no physical meaning, the field evolution animations are done in grayscale.

Examples and tests

Herein we present some results which document the possibilities of the LIC visualization method.

In Table 6 you can see an example of the transferred data file, in Fig. 22 there is an example of electric field visualization and in Fig. 23 there is an example of magnetic field visualization.

In Tables 7 and 8 we can see the time consumption for the calculation of the output figure. It depends approximately linearly on the field line length, and more than linearly (but less than quadratically) on the figure size. Furthermore the calculation is more complicated for the vortex field than for the radial one [56].

Table 6: Head and a small part of the transferred data file

Particle in Cell Simulation Results					
24	16	16			
@FRAME					
@PARTICLE ELECTRON 0 0 255					
0.918	8.078	7.477	9.289	1.488	-1.235
3.067	7.295	8.802	-2.166	0.239	-0.391
5.178	9.207	9.252	2.208	-1.310	0.594
15.206	7.838	7.681	-1.015	1.732	-1.816
8.152	8.040	9.455	2.904	-2.467	-0.129
4.793	8.294	8.745	-1.452	2.546	0.839
15.567	7.963	9.422	0.623	0.426	3.791
4.760	7.469	9.143	2.236	1.661	-0.821
14.348	7.783	8.599	3.348	-2.083	-2.441
18.720	8.143	8.614	-2.881	0.698	0.688

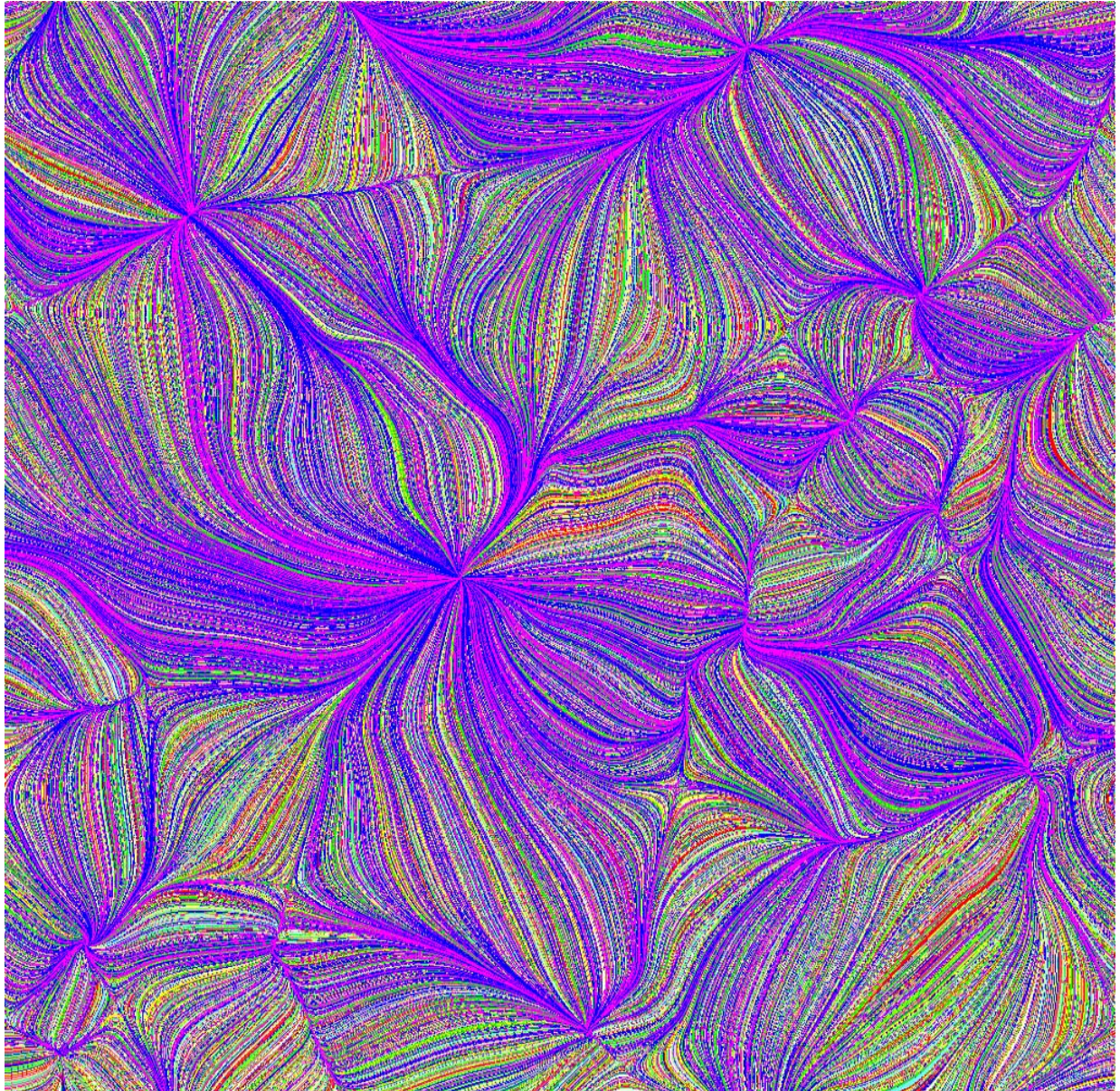


Fig. 22: LIC visualization of the electric field lines. The cross section plane was perpendicular to the filament. If the charged particle is nearby the cross section, local Coulomb field can be seen.

Table 7: Calculation times for radial fields by LIC in seconds. Intel Celeron 450, 128 MB RAM, video card Riva TNT, hardware acceleration OpenGL, OS: MS Windows NT 4.0 Workstation.

UNIT VISUAL		Figure size		
		256	512	1024
Field-line length	128	10	44	170
	265	11	53	224
	512	15	57	266
	1024	16	67	268
	2048	16	68	298

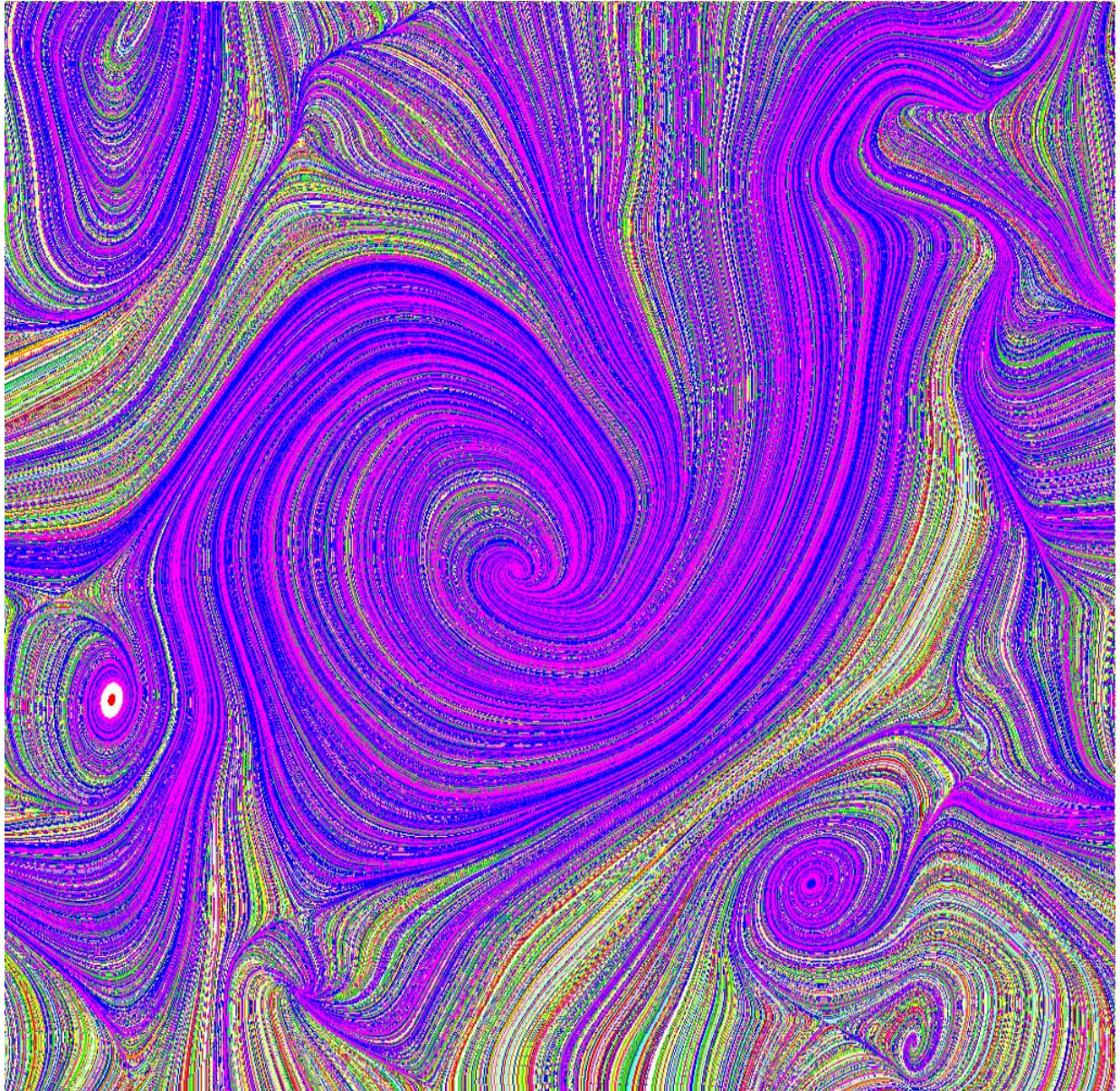


Fig. 23: LIC visualization of the magnetic field lines. The cross section plane was perpendicular to the filament. Typical magnetic vortices can be seen if the cross section plane is nearby the charged particle.

Table 8: Calculation times for vortex fields by LIC in seconds. Intel Celeron 450, 128 MB RAM, video card Riva TNT, hardware acceleration OpenGL, OS: MS Windows NT 4.0 Workstation.

UNIT VISUAL		Figure size		
		256	512	1024
Field-line length	128	10	44	170
	265	11	53	224
	512	15	57	266
	1024	16	67	268
	2048	16	68	298

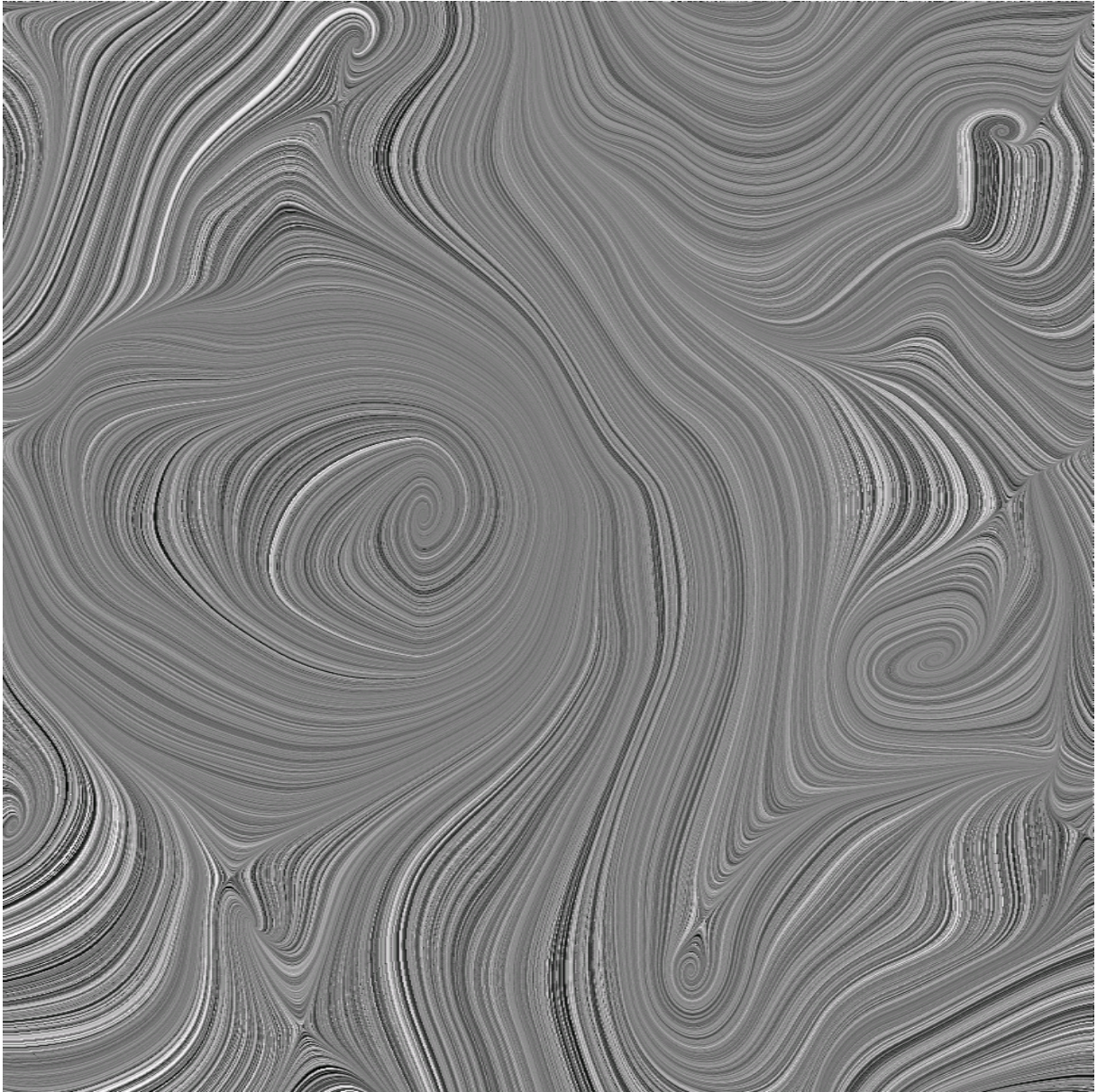


Fig. 24: LIC visualization of the magnetic field lines. The cross section plane was perpendicular to the filament. Field evolution was treated in this test. The field evolution is best seen in the grayscale. The color output of the LIC method is to a certain extent random and cannot be used for animation or field evolution tracking purposes.

3.2. Particle Visualization

The visualization program package VISUAL has two parts. First of them enables visualizing fields and was described in previous chapter. The second one serves as the visualizing tool for tracking particles. This part of the package VISUAL will be the topic of this chapter.

Basics

All the particles have three main attributes transferred to the package VISUAL in the data file *.dpc.

- *Charge* (negative, positive or neutral).
- *Position* in the three-dimensional rectangular parallelepiped.
- *Velocity* vector.

The particle is in the frame represented by a graphical object with appropriate graphical attributes (*color, tint, size*) in place given by its position vector.

Particles of the same kind are represented by the same *color*. Implicitly electrons are blue, ions red and neutrals green. This pre-set can be changed directly in the key statement @PARTICLE in the data file. This statement has as parameters RGB values of the displayed color. The color *tint* corresponds to the particle temperature calculated from the chaotic component of the velocity vector. The color of each particle then depends on its kind and temperature. Particles of the same kind have the same basic color and particle with the same temperature have the same color tint.

The velocity vector of the particles is in the package used only for the temperature calculation VISUAL. The vector itself is not displayed because the movements of all the particles can be tracked step by step by browsing successive frames of the scene.

The particles are represented in the scene as 3D polyhedrons which evoke best the spherical shape. Depiction of a great number of such objects is very time-consuming and therefore it is possible to change the complexity of the polyhedron. User can enter two parameters determining the number of meridians and parallels on the sphere. A polyhedron best fitting the sphere is calculated from these data. Increasing the number of meridians and parallels we obtain better similarity of the polyhedron and the sphere at the expense of the increasing depiction time. The diameter of the sphere can be chosen for every kind of the particle.

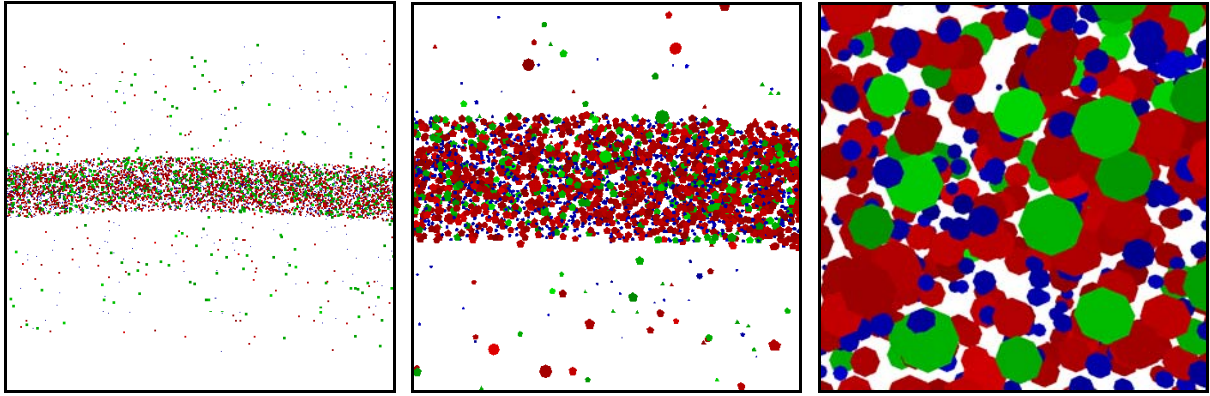


Fig. 25: Particles displayed in three different magnifications. Color of the particles denotes the kind of the particle (blue – electron, red – ions, green – neutrals). The tint denotes the particle's temperature. The polyhedrons representing particles can be seen in the biggest magnification.

Filters

There are three filters implemented in the package VISUAL which enable to depict only some of the particles. The filters decrease the time-consumption of the scene depicting.

- *Filter KIND.* Only some kinds of the particles can be depicted in the scene (e.g. electrons only).
- *Filter TEMPERATURE.* The filter enables to depict only particles with temperature in previously defined interval.
- *Filter SLICE.* The filter enables to define cross section planes parallel to the axes and to depict either particles above or below (left or right; in front or behind) such a plane or particles in narrow region nearby the defined plane.

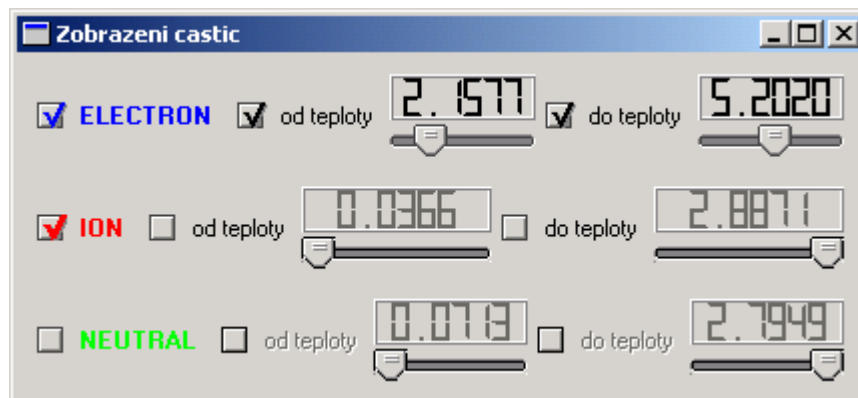


Fig. 26: Dialog window for filters KIND and TEMPERATURE. The actual setting will depict electrons in the temperature range from 2.1577 eV to 5.2020 eV, all ions and no neutrals.

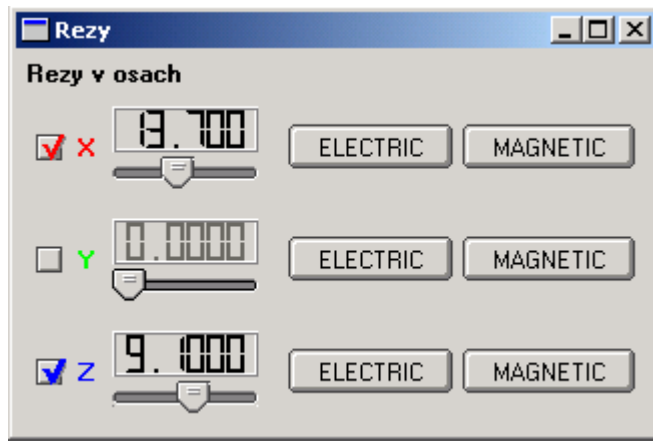


Fig. 27: Dialog window for filter SLICE. There are two cross section planes ($x = 13.7$ and $z = 9.1$). The buttons on the right enable calculation of electric and magnetic field in the cross section planes by LIC method described in chapter 3.1.

Transformations of the scene

There are three possible transformations of the scene included in the VISUAL package:

- *Zoom.* The scene can be zoomed to see the details of interesting areas.
- *Rotation.* The scene can be rotated and examined from various visual angles.
- *Translation.* The scene can be shifted along the coordinate axes.

Examples and tests

The fastness of the scene depiction in frames per second (fps) is presented in Table 9. Values are given for various numbers of particles and various levels of details (number of meridians and parallels describing the particle). Sufficiently fast respond is for one thousand particles. For higher number of particles either the response is not immediate or some filters have to be used to lower the number of the displayed particles.

Table 9: Fastness of the particles depiction in fps. Intel Celeron 450, 128 MB RAM, video card Riva TNT, hardware acceleration OpenGL, OS: MS Windows NT 4.0 Workstation [56].

UNIT VISUAL		Level of details		
		8x8	5x5	3x3
Number of particles	1 000	11.00	17.00	25.00
	5 000	2.50	4.70	8.20
	10 000	1.30	2.45	4.30
	15 000	0.80	1.64	2.90
	20 000	0.65	1.24	2.21
	30 000	0.42	0.83	1.50

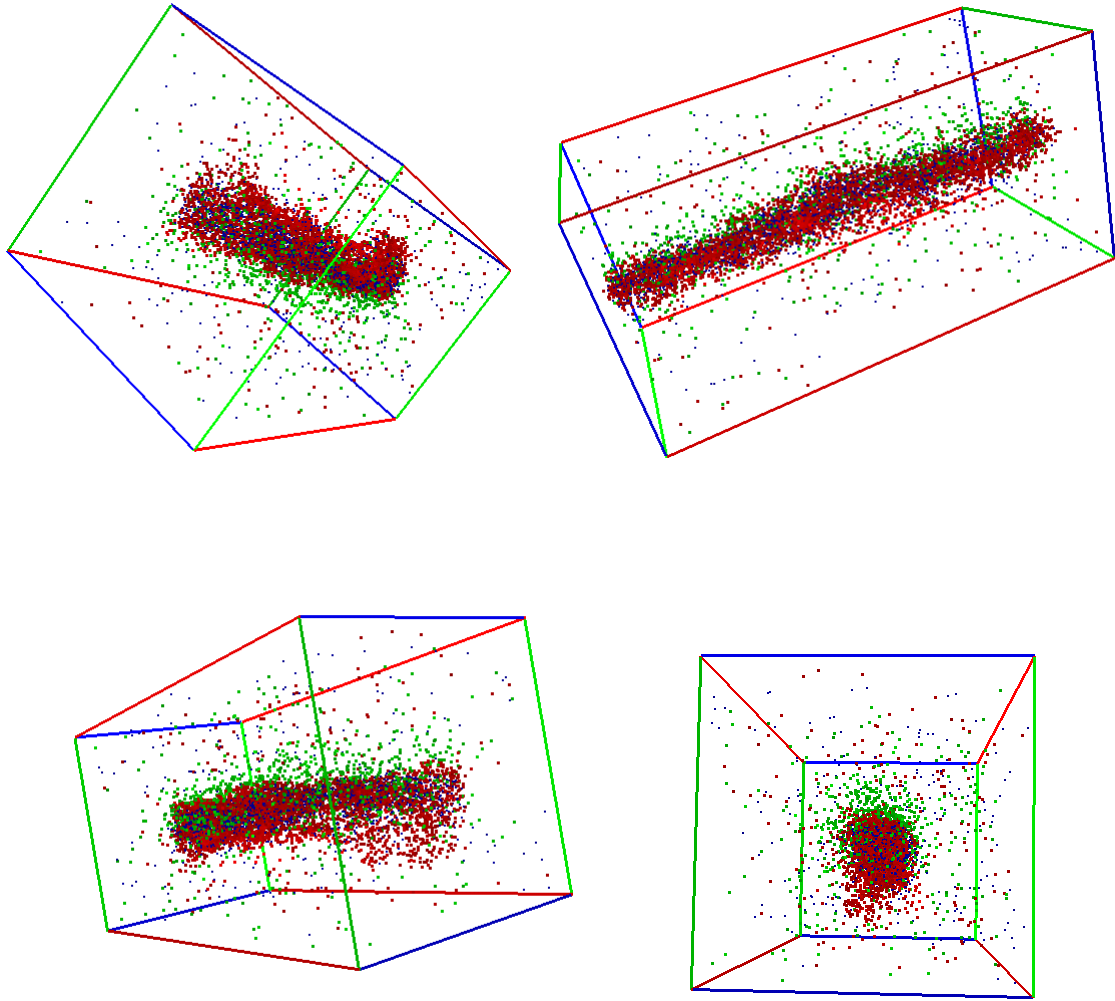


Fig. 28: Interactive rotation of the scene can be very useful.

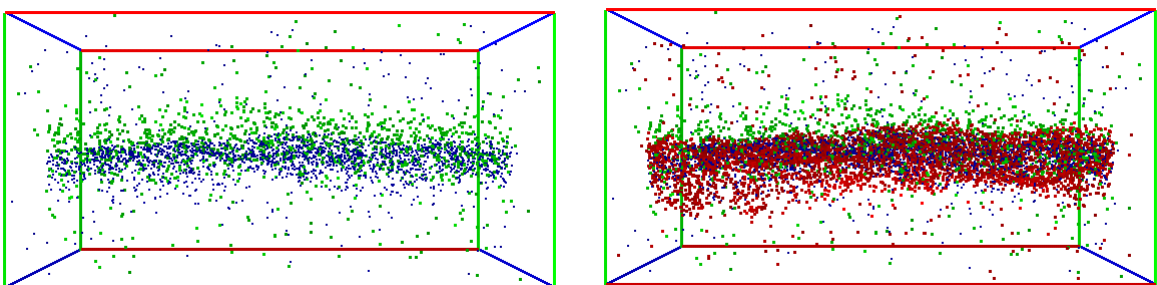


Fig. 29: Filter KIND. On the left only electrons and neutrals are imagined.
On the right all the particles can be seen.

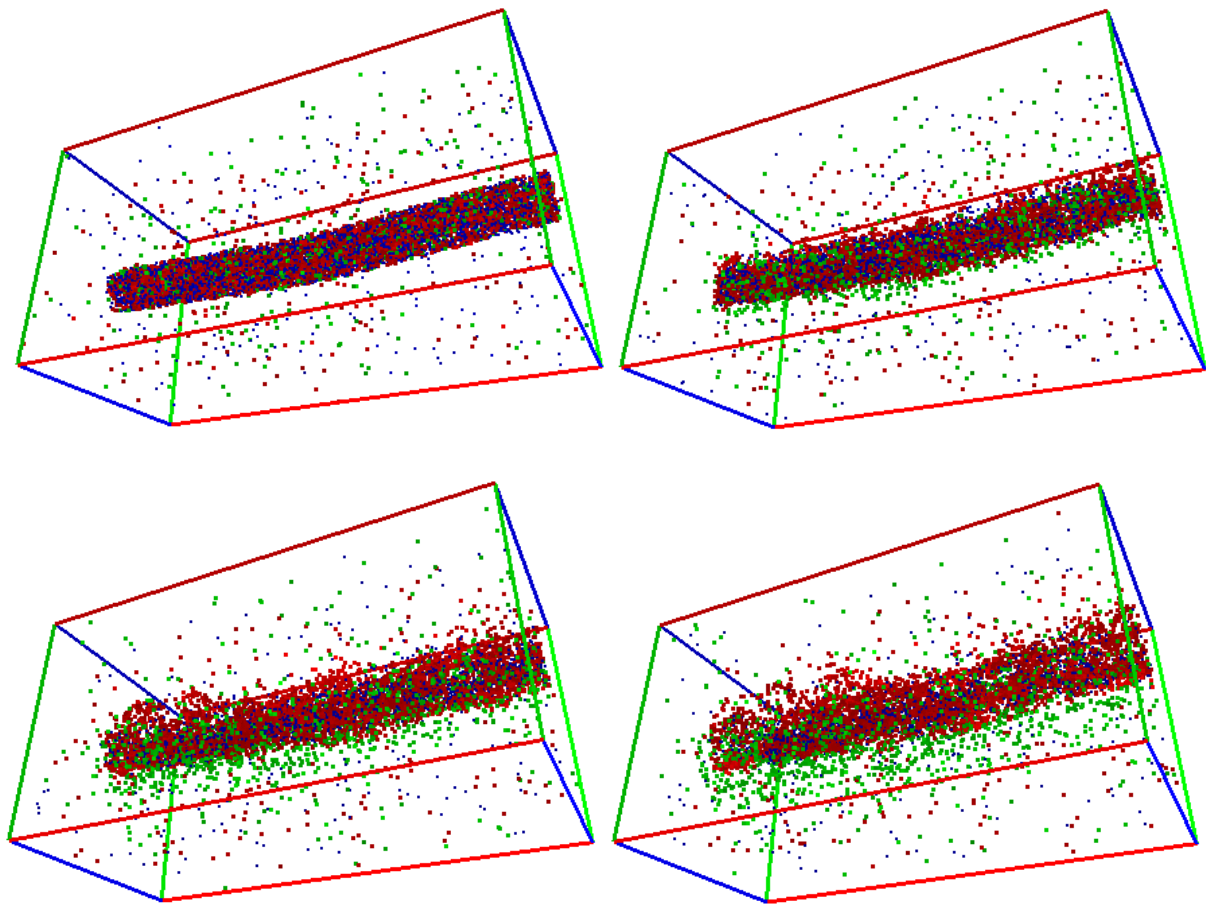


Fig. 30: Tracking the particle motion through succeeding frames give us the information about the filament evolution.

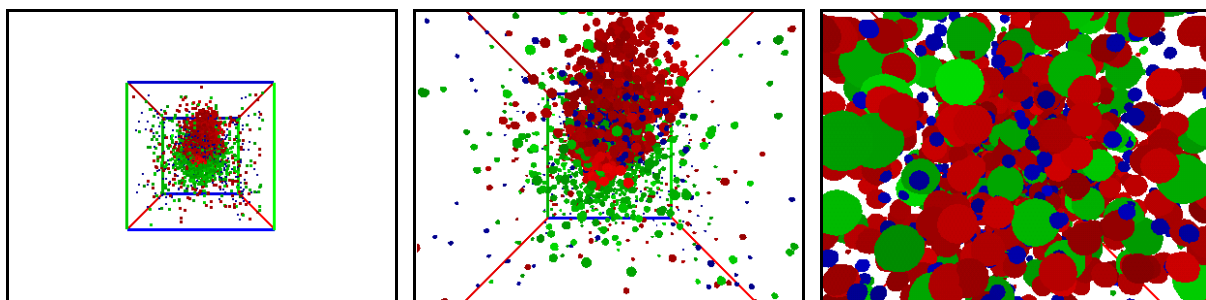


Fig. 31: Another interesting tool of the package VISUAL: Zoom tool.

3.3. Diagnostics

Computer plasma diagnostics is very useful both for debugging the program package and for the correspondence with lab and space experiments. Usually the mean values of particle velocities and fields are tracked through the computation. Especially valuable are the mean square values and variances for their relation with measurable physical quantities such as

temperature, thermal and electrical conductivity, specific heat, electric and magnetic susceptibility, etc.

Basics

First of all very useful are *simple average values* of many quantities (n is indexing particles, α kinds of particles, i, j, k the grid points):

$$\langle \mathbf{v}_\alpha \rangle = \frac{1}{N_\alpha} \sum_{n=1}^{N_\alpha} \mathbf{v}_{\alpha,n}; \quad \alpha = e, i, n, \quad (15)$$

$$\langle \mathbf{j} \rangle = \frac{1}{V} \sum_{\alpha} \left(Q_\alpha \sum_{n=1}^{N_\alpha} \mathbf{v}_{\alpha,n} \right), \quad (16)$$

$$\langle \mathbf{P} \rangle = \frac{1}{V} \sum_{\alpha} \left(Q_\alpha \sum_{n=1}^{N_\alpha} \mathbf{r}_{\alpha,n} \right), \quad (17)$$

$$\langle \mathbf{M} \rangle = \frac{1}{V} \sum_{\alpha} \left(\frac{1}{2} Q_\alpha \sum_{n=1}^{N_\alpha} \mathbf{r}_{\alpha,n} \times \mathbf{v}_{\alpha,n} \right), \quad (18)$$

$$\langle \mathbf{E} \rangle = \frac{1}{N_x N_y N_z} \sum_{i=1}^{N_x} \sum_{j=1}^{N_y} \sum_{k=1}^{N_z} \mathbf{E}_{ijk}, \quad (19)$$

$$\langle \mathbf{B} \rangle = \frac{1}{N_x N_y N_z} \sum_{i=1}^{N_x} \sum_{j=1}^{N_y} \sum_{k=1}^{N_z} \mathbf{B}_{ijk}. \quad (20)$$

The quantities defined in Eqs (15) - (20) are subsequently: average velocity of α -kind particles, total current density, polarization, magnetization, electric and magnetic fields. Averaging proceeds either over all particles or over all the grid points. Knowing polarization and magnetization the electric induction and magnetic intensity vectors can be obtained:

$$\mathbf{D} = \varepsilon_0 \mathbf{E} + \mathbf{P}; \quad \mathbf{H} = \frac{\mathbf{B}}{\mu_0} - \mathbf{M}. \quad (21)$$

Under the assumption of diagonal conductivity, permittivity and permeability tensors, they can be “measured” as

$$\sigma_k = j_k / E_k; \quad \varepsilon_k = D_k / E_k; \quad \mu_k = B_k / H_k. \quad (22)$$

The *quadratic averaging* is also of great importance, especially variances of some quantities, which are related to experimentally measured quantities such as temperature, heat capacity, susceptibility, etc. [83]:

$$\langle v^2 \rangle - \langle v \rangle^2 = \frac{kT}{m} (3 - 8/\pi); \quad (23)$$

$$\langle v^4 \rangle - \langle v^2 \rangle^2 = 6 (kT/m)^2; \quad (24)$$

$$\langle W^2 \rangle - \langle W \rangle^2 = kT^2 C_V; \quad (25)$$

$$\langle \mathbf{M}^2 \rangle - \langle \mathbf{M} \rangle^2 = \frac{1}{\mu_0} \frac{kT}{V} \chi. \quad (26)$$

The averaged particle quantities are saved separately for electrons, ions and neutrals, so electron and ion components of currents density are known as well as temperatures of relevant sub-fluids.

Another interesting and valuable diagnostics can offer a plot of the particles in phase space (velocity versus coordinates). Some instabilities can be detected from characteristic patterns.

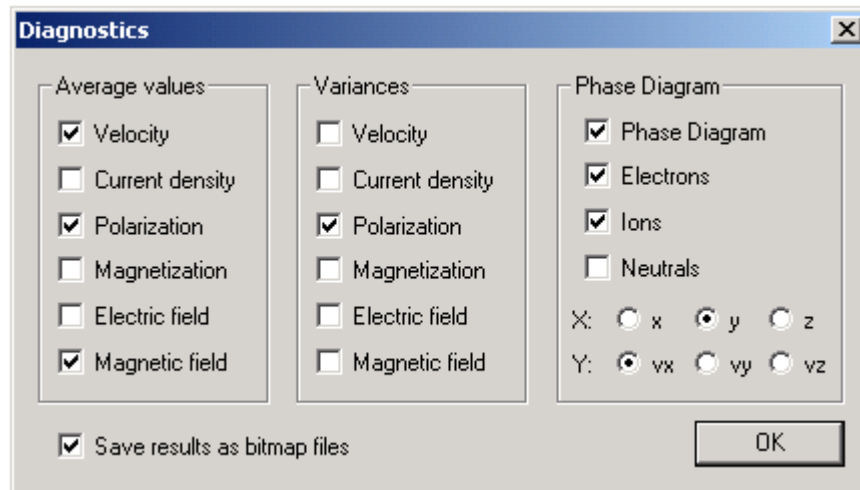


Fig. 32: Dialog window for diagnostic routines. Derived quantities as conductivity, temperature, etc., will be calculated from checked quantities.

Averaging velocities and fields

Averaging of all the velocity components is done for electrons, ions, neutrals and dust particles individually. The averaging procedure works in successive steps according to the scheme

$$\langle a \rangle_{n+1} = \langle a \rangle_n \frac{n}{n+1} + \frac{a_n}{n+1} ; \quad n = 1, 2, 3, \dots \quad (27)$$

This scheme has a great advantage. It works both for averaging of all the particles (the total number of particles is known) and averaging through the time evolution of some quantity (the total number of steps is not known and furthermore we need the intermediate results). The averaging procedure was tested on an assembly of particles with predetermined Gauss velocity distribution:

Table 10: Combined tests of the averaging procedure and Gauss distribution generator.

Temperature of the assembly was 3 eV, non-dimensional mass was 1.

The non-dimensional average velocities are presented in the table below.

DIAGNOSTICS	$\langle v_x \rangle$	$\langle v_y \rangle$	$\langle v_z \rangle$	$\langle v_x^2 \rangle$	$\langle v_y^2 \rangle$	$\langle v_z^2 \rangle$
Test 10 particles	+0.0429	+0.1086	-0.1723	+3.6486	+0.9710	+1.5310
Test 100 particles	-0.0732	+0.1821	-0.2070	+2.8359	+2.9889	+2.7710
Test 1 000 particles	-0.0436	-0.0173	-0.0385	+2.8473	+2.8860	+3.0579
Test 10 000 particles	-0.0095	-0.0376	-0.0244	+3.0218	+2.9790	+3.0114
Precise values	0.0	0.0	0.0	3.0	3.0	3.0

The fields are averaged in the same manner as particles. The only difference is that the averaging process proceeds over grid points instead over the particles.

Averaging over particles is saved in fields of type

```
AverField(1:6,1:k,1:N);
```

1:6 is indexing average and quadratic average field ,
 1:k is indexing particles (electrons, ions, neutrals, ...),
 1:N is indexing time .

(28)

Averaging over grid is saved in fields of type

```
AverField(1:6,1:N);  
1:6 is indexing average and quadratic average field ,  
1:N is indexing time .
```

(29)

Some tests and results

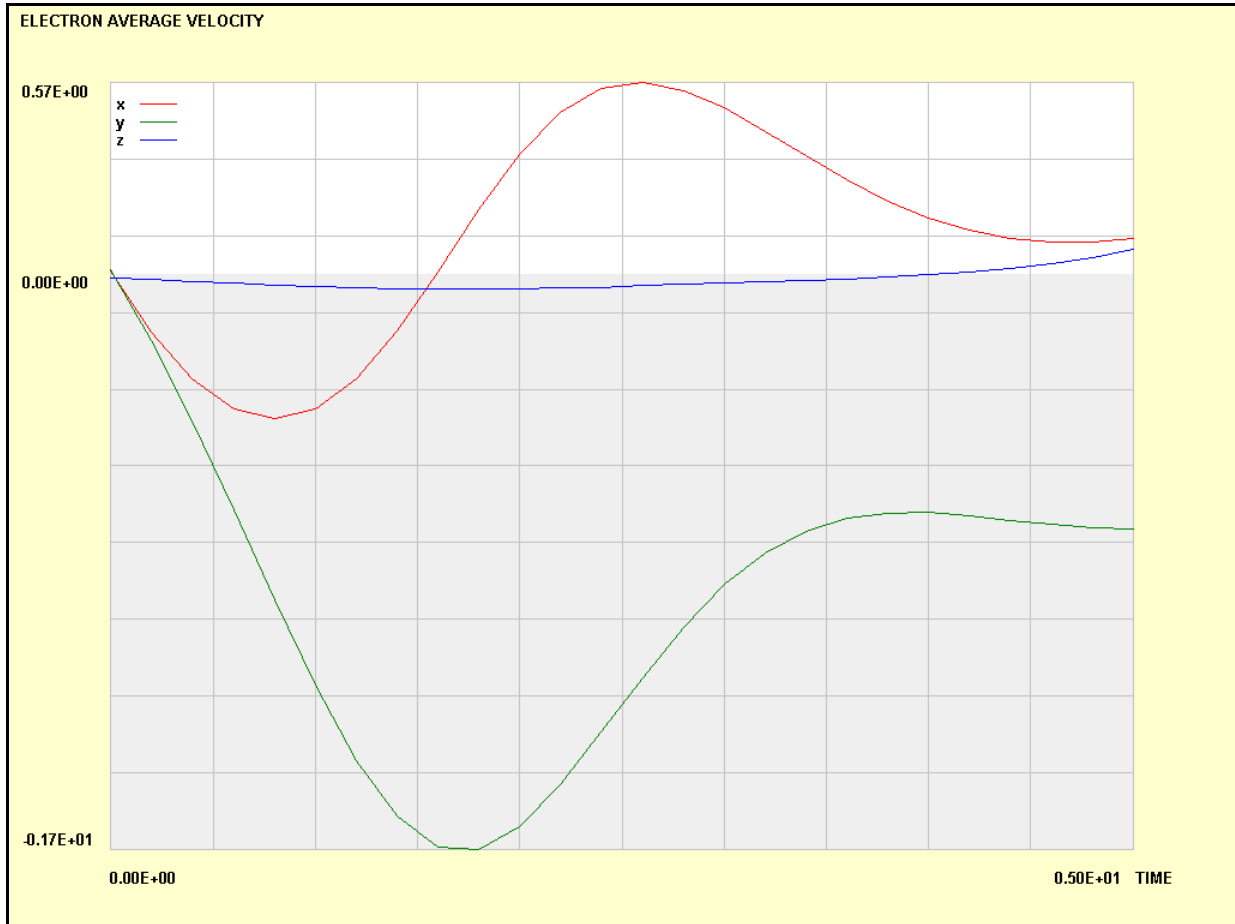


Fig. 33: Test of the diagnostic routines. Average velocity of the electron component plotted versus time is on the figure. Initial average velocity in all the axes was zero (Gauss distribution). Drift in (xy) plane was simulated. The velocity changes in the z-axis are insignificant. The gray area displays negative values.

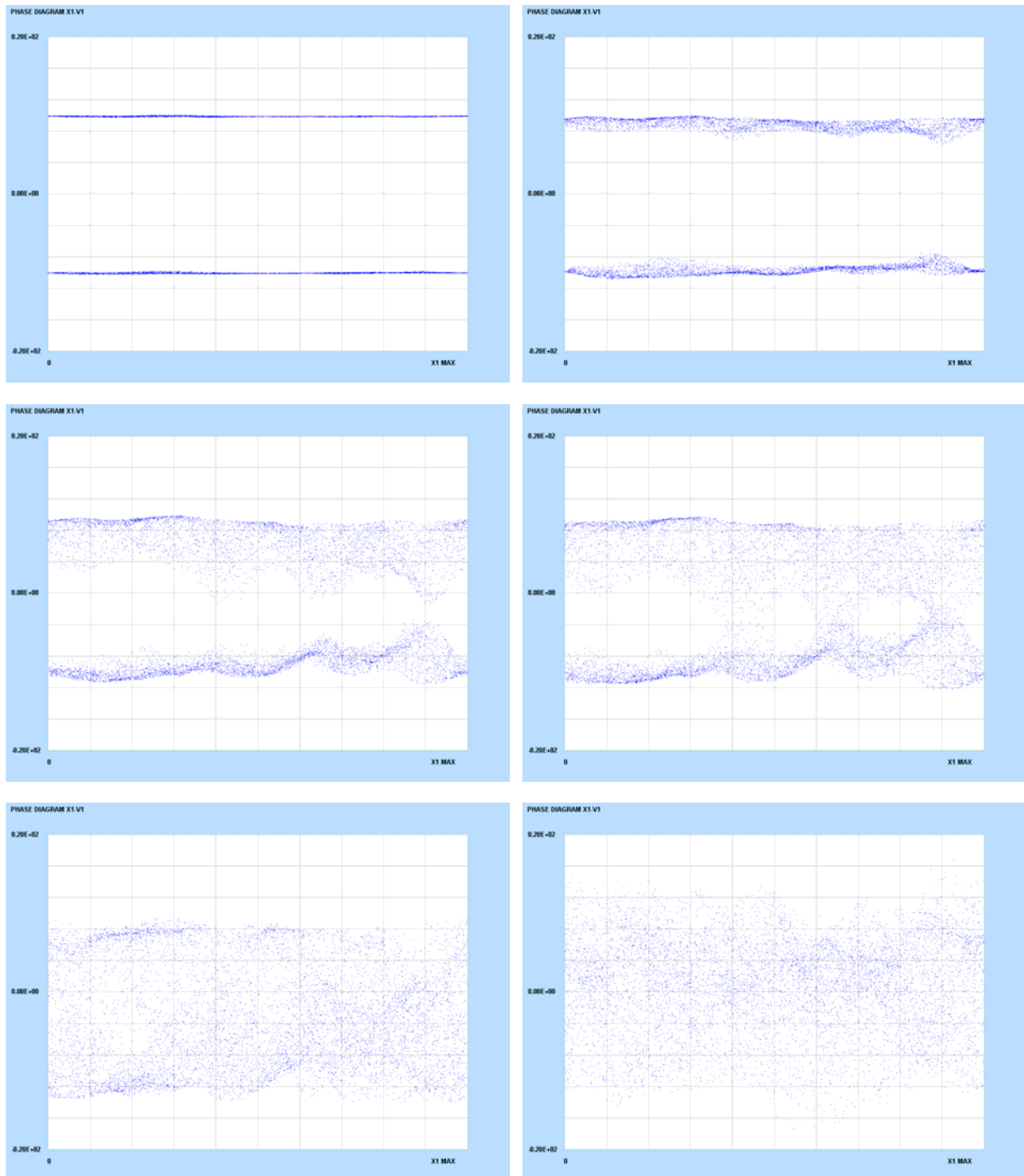
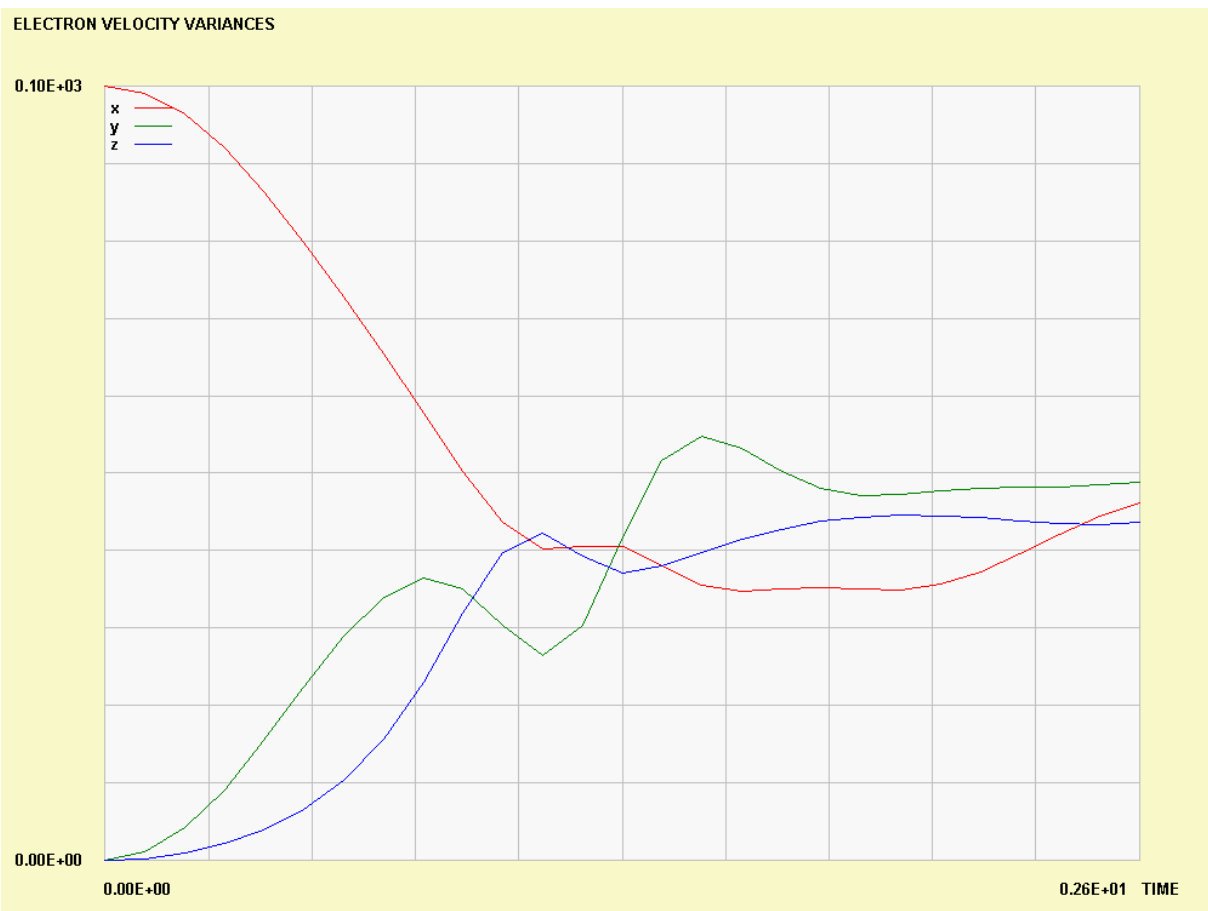
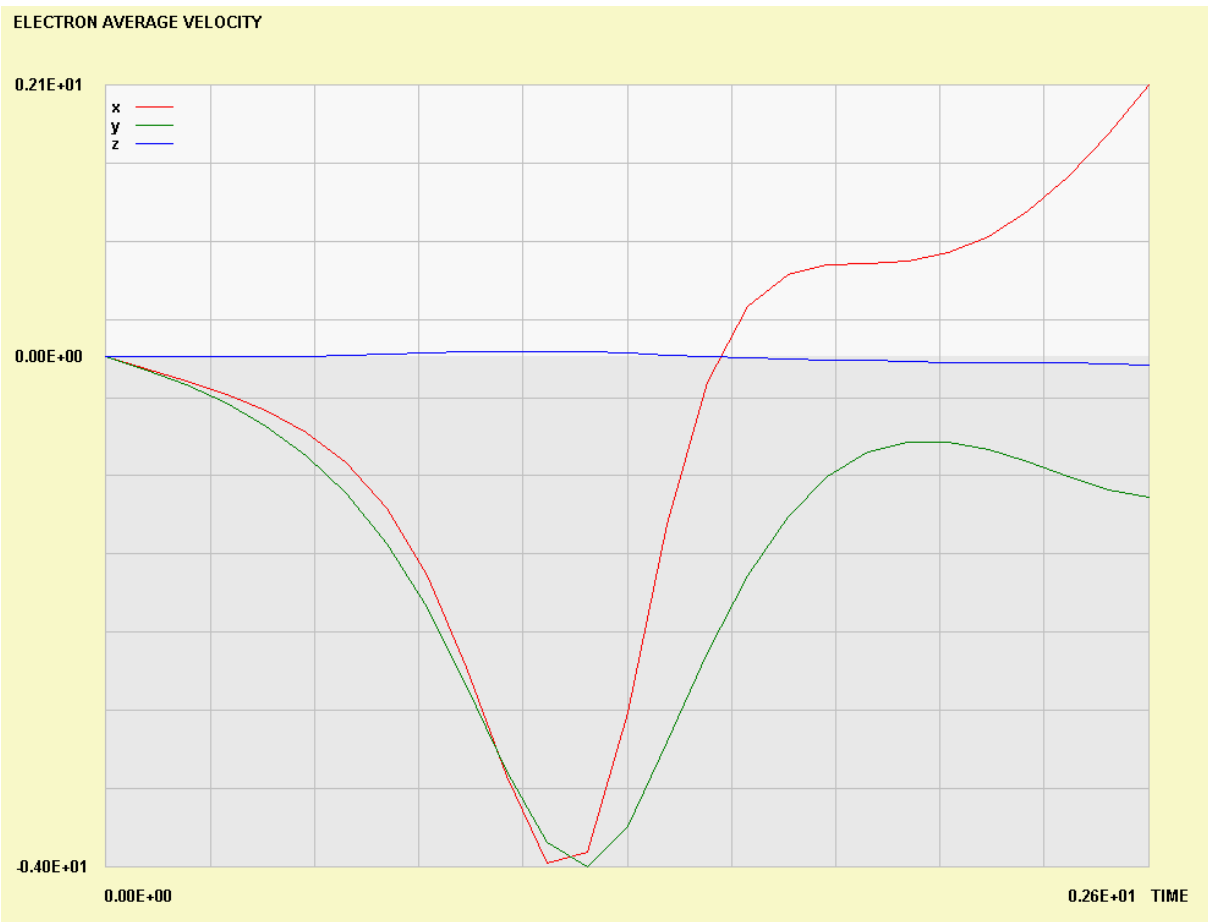


Fig. 34: Two stream instability, phase space diagrams. On this series you can see two-stream instability test (one of most popular tests of PIC simulation correctness). Two electron beams have opposite velocities and collide. On horizontal axis there is x position of the particles, on vertical axis there is x velocity component. In the first figure we can in the phase portrait see two different velocities, one positive (R beam) and one negative (L beam). On succeeding figures the beams collide and thermalization of the velocities occurs.

Figs. 35, 36 (next page): Two stream instability, thermalization. **Top:** average electron velocities. The beams move in opposite directions, average velocity is zero in the beginning. **Bottom:** In the beginning $\langle U_x U_x \rangle$ is nonzero positive and $\langle U_x \rangle \langle U_x \rangle$ is zero for both beams altogether. That is why the variance of the x velocity component is nonzero. Thermalization results in successive equalizing of all the three velocity component variances.



Figs 35, 36: See previous page.

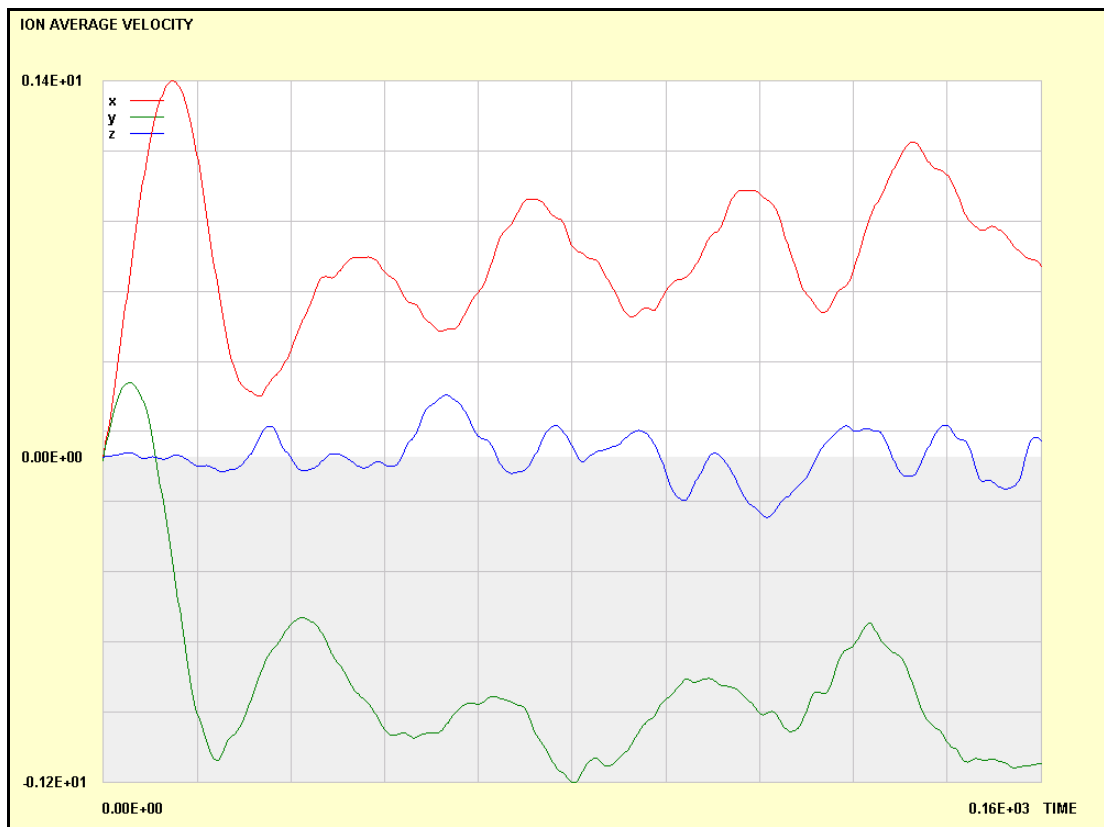


Fig. 37: Ion average velocities. Drift motion in (xy) plane can be detected. In z direction average velocity is approximately zero. Test: 10 000 particles; red: x-component, green: y-component, blue: z- component.

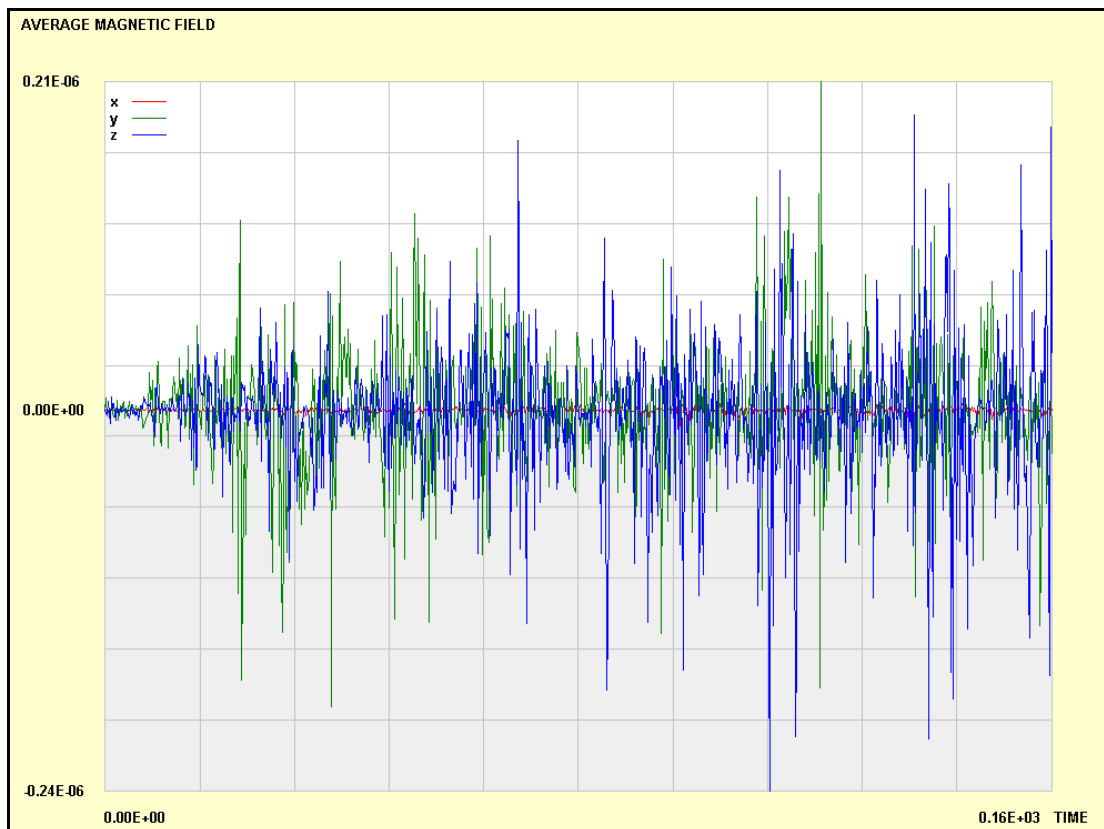


Fig. 38: Average magnetic field. Typical situation – one component is approximately zero (x) and the others have chaotic behaviors; red: x-component, green: y-component, blue: z-component.

3.4. Collisions

In 2001-2002, collisions of the neutrals with electrons and ions were included in the model, as well as ionization and recombination processes. The collisions are calculated via known cross sections by Monte Carlo method [40, 42, 44, 83]. This module of the PIC package created Dan Škandera in frame of his Diploma Thesis [64, 78].

Basics

The pair interaction of charged particles is fully solved in PP (Particle-Particle) codes, which are very time consuming. The PIC code naturally bypasses this problem and instead of collisions introduces interaction with global field generated by the particles. Simple versions of PIC simulation do not need additional collisions for physically correct results. Nevertheless PIC simulations cannot describe interaction of charged particles with neutrals. These types of collisions have to be introduced into the model from “outside”.

There are several possibilities how to add collisions with neutrals into PIC code. If we do not want to permit enormous slowing-down of the model due to the collisions, we have to compute the collisions only statistically (e.g. by Monte Carlo method) with simplified cross section dependence. This is the way we set forward in our department.

There are two types of interactions to be added into the model: Interaction of electrons with neutrals and interaction of ions with neutrals. Due to different mass of the electron and ion the two types of collisions have different cross section area dependence. For numerical treatment a reasonable approximation of real cross sections is introduced in Fig. 39 [6, 7].

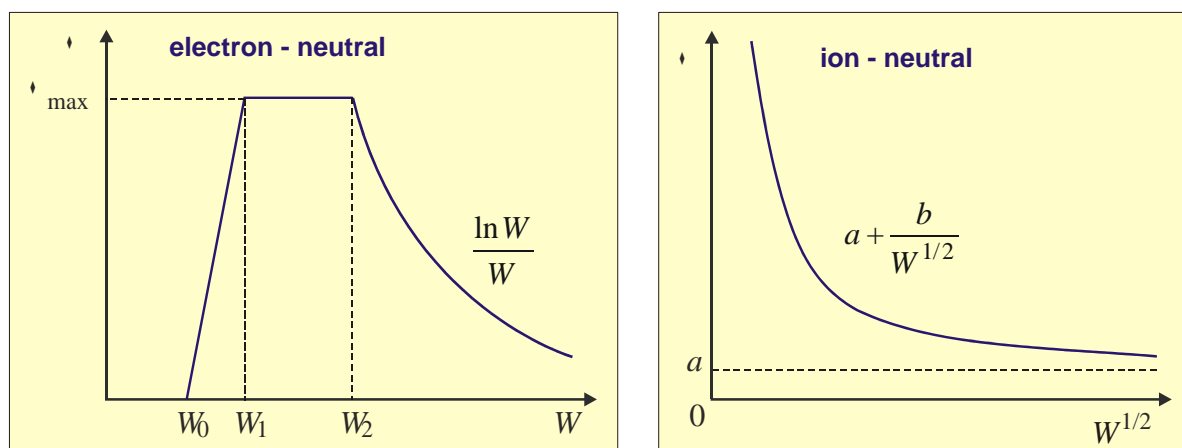


Fig. 39: Approximation of cross section area dependence suitable for numerical calculations [7]

Electron-neutral collisions

The electron-neutral collisions can be divided into three basic types:

1. Elastic collisions
2. Excitation
3. Ionization

These types of collisions differ in the values of characteristic constants W_0 , W_1 , W_2 , σ_{\max} (see Fig. 39). Furthermore these constants strongly depend on the kind of plasma. For example the argon plasma values are presented in Table 11. Values for other kinds of plasma can be found in [1, 2, 9]. Let us remark that the value W_0 has the meaning of minimum energy required for given process. For elastic collisions it is zero, for excitation processes it is the excitation energy and for ionization it is the ionization energy.

Table 11: Values of characteristic constants W_0 , W_1 , W_2 , σ_{\max} for electron-neutral cross section area dependence in argon plasma [9].

COLLISIONS	W_0 [eV]	W_1 [eV]	W_2 [eV]	σ_{\max} [m ²]
Elastic	0	15	20	1.2×10^{-19}
Excitation	11.55	30	100	7×10^{-21}
Ionization	15.76	30	100	3×10^{-20}

Ion-neutral collisions

These collisions are typical with approximately the same mass of both interacting particles. There are two basic types of these collisions:

1. Elastic collisions
2. Collisions with charge exchange

In simplified cross section area dependence according to the Fig. 39, these collisions are determined by two characteristic constants a and b . Their values can be found in literature, for example in [9]. Values for argon plasma are given in Table 12.

Table 12: Values of characteristic constants a and b for ion-neutral cross section area dependence in argon plasma [9].

COLLISIONS	a [m ²]	b [m ² eV ^{1/2}]
Elastic	1.8×10 ⁻¹⁹	4.0×10 ⁻¹⁹
Exchange	2.0×10 ⁻¹⁹	5.5×10 ⁻¹⁹

Algorithm

The whole algorithm how to implement collisions into PIC model consists from six basic steps:

1. Does the collision occur?
2. What kind of collision will happen?
3. Determination of relative velocity magnitude after the collision.
4. Transformation into new coordinate system.
5. Monte Carlo generation of new particle velocity direction (angles).
6. Transformation of new velocity back into the lab coordinate system.

Let us describe now these steps one by one.

Step 1: Does the collision occur?

After each calculation of new particle positions via some particle solver we have to do the following procedure:

First of all we must for every particle, let us say particle a , look in the neighborhood for possible candidates for collision (particles b). The enterable neighborhood can be defined by Debye sphere with the radius

$$r_D = \sqrt{\frac{\epsilon_0 k_B T}{n Q^2}} . \quad (30)$$

Secondly, we have to calculate total collision frequency for the watched particle a :

$$\nu_a = \sum_b \sum_p n_b \sigma_{p(a,b)}(W) v_{ab} . \quad (31)$$

Here a is the watched particle, b are candidates for collision inside the Debye radius, p indexes possible collision processes, W is known energy of the particle, v_{ab} is relative velocity of watched and target particles.

Thirdly, we generate random number γ_1 in the interval $\langle 0,1 \rangle$ and compare it with the probability of some collision during PIC time step interval Δt :

$$P_a = 1 - \exp[-v_a \Delta t]. \quad (32)$$

For $P_a > \gamma$ some collision will occur and we will proceed following steps. Otherwise the watched particle will not take part in any collision during this PIC step.

Step 2: What kind of collision will happen?

To decide what kind of collision from all the possible ones will happen, we can use standard method of cumulative distribution function (method of shooting) [83]. *Firstly* we calculate the cumulative distribution function

$$D_k = \frac{\sum_{p=1}^k \sigma_p}{\sigma_{\text{tot}}}; \quad \sigma_{\text{tot}} = \sum_{p=1}^N \sigma_p. \quad (33)$$

The values of the cumulative distribution function subsequently are $D_0 = 0$, $D_1 = \sigma_1 / \sigma_{\text{tot}}$, $D_2 = (\sigma_1 + \sigma_2) / \sigma_{\text{tot}}$, etc. The last value is $D_N = 1$. *Secondly* we generate random number γ_2 in the interval $\langle 0,1 \rangle$ and if it is from the interval (D_{n-1}, D_n) , process $p = n$ happens.

Step 3: Determination of the magnitude of the relative velocity after the collision

We have selected two interacting particles a and b and the kind of process (collision) p . From the energy conservation law we can determine the energy of watched particle a after the collision. According to the process chosen in previous step we have to involve ionization or excitation energy, if any. The energy formulas are given in Table 13:

Table 13: Energy formulas for considered processes

COLLISIONS	ENERGY FORMULA
e-n elastic	$W_a = W_{0a}$
e-n excitation	$W_a = W_{0a} - W_{\text{excit}}$
e-n ionization	$W_a = B \operatorname{tg} \left[\gamma_3 \operatorname{arctg} \left(\frac{W_{0a} - W_{\text{ionization}}}{2B} \right) \right]^*$
i-n elastic	$W_a = W_{0a} \cos^2 \theta^{**}$
i-n charge exchange	$W_a = D^{-1}(\gamma_3)^{***}$

- * During ionization the input energy minus ionization energy must be redistributed between the old electron and the new one. This is done by the method of inverse distribution function [83]. The cross section area dependence (Fig. 39) is integrated over energy with variable upper limit. The result is cumulative distribution function $D(W)$. The algorithm is the same as in Step 2. The only difference is that Step 2 had several discrete processes and D was calculated by summation; here the processes are continuous and D has to be determined by integration. After that random number γ_3 is generated and set equal to D . From the equality $D(W_a) = \gamma_3$ we calculate (inversion of D) the new energy W_a . The result contains the plasma characteristics W_0 , W_1 , W_2 , σ_{\max} combined in constant B and the random number γ_3 .
- ** The angle θ is the angle of the relative velocity rotation (magnitude does not change during the collision) introduced in Step 5.
- *** Fast ion collides with slow neutral and taking over one electron becomes fast neutral. The second product is slow ion with isotropic velocity distribution. The new energy of slow ion is calculated from differential cross section by the method of inverse cumulative distribution function in the same manner as it was during e-n ionization collision.

Step 4: Transformation into new coordinate system

The relative velocity is transformed to new coordinate system which is rotated in such a way, that the new velocity has component only in z direction. The angles determining the transformation are defined in Fig. 40.

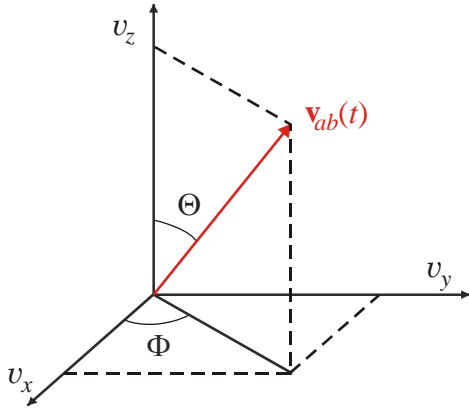


Fig. 40: Definition of the angles Θ, Φ .

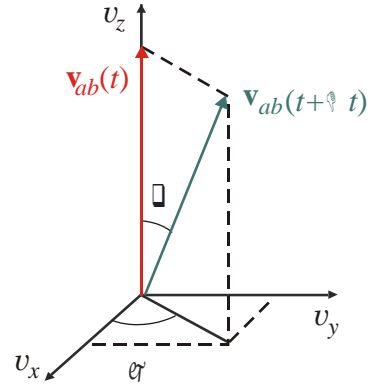


Fig. 41: Definition of the angles θ, φ .

Now the transformation proceeded in time t can be written as

$$\begin{pmatrix} \cos \Theta \cos \Phi & \cos \Theta \sin \Phi & -\sin \Theta \\ -\sin \Phi & \cos \Phi & 0 \\ \sin \Theta \cos \Phi & \sin \Theta \sin \Phi & \cos \Theta \end{pmatrix} \cdot \begin{pmatrix} v_x \\ v_y \\ v_z \end{pmatrix}_t = \begin{pmatrix} 0 \\ 0 \\ v \end{pmatrix}_t. \quad (34)$$

Step 5: Monte Carlo generation of new particle velocity direction (angles).

The magnitude of the relative velocity does not change after the collision. However the direction of the velocity changes. In the coordinate system introduced in the Step 4 the new velocity is given by the angles θ, φ . These new angles will be determined by Monte Carlo process from the differential cross section formulas by the method of the inverse cumulative distribution function, see Fig. 41. The calculated values are in Table 14:

Table 14: Angles θ, φ calculated by the method of the inverse cumulative distribution function. Energy W_a is given in eV. Random numbers in the interval $\langle 0,1 \rangle$ are denoted γ . Cross section dependence on the θ was taken from M. Surendra et al. [6].

COLLISIONS	ANGLES θ, φ
e-n elastic	$\theta = \arccos \left(\frac{2 + W_a - 2(1 + W_a)^{\gamma_4}}{W_a} \right),$ $\varphi = 2\pi\gamma_5.$
e-n excitation	
e-n ionization	
i-n elastic	$\theta = \arccos \sqrt{1 - \gamma_6}; \quad \varphi = 2\pi\gamma_7$
i-n charge exchange	$\theta = \pi\gamma_8; \quad \varphi = 2\pi\gamma_9$

Step 6: Transformation of new velocity back into the lab coordinate system

The last step is very simple. We perform inverse rotational transformation (34) to be back in the original coordinate system. From the new relative velocity we calculate new velocity of the watched particle a after the collision.

Some tests and results

The collision module is the last one implemented in the PIC package and is not fully tested at present time. Anyway it is known that the general features of the PIC results are not influenced, only the tiny details.

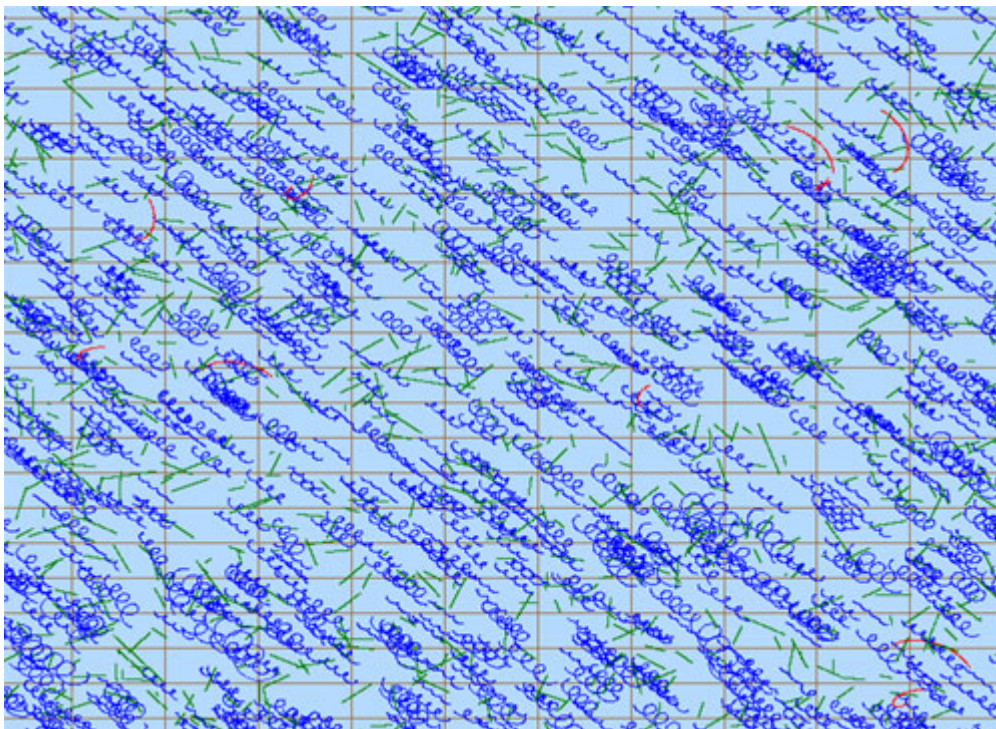


Fig. 42: Test of the module COLLISIONS. Initially only electrons and neutrals were present in external electric and magnetic field. The drift motion is visible. The red curves are ions generated during collisions of the electrons with neutrals by ionization processes.

3.5. Radiation

A very important way of energy losses is radiation [41]. There are several important radiation channels, but the magnitude of most of them can be only estimated from some global considerations. The only one exception is bremsstrahlung radiation and synchrotron radiation. The intensity of this radiation can be calculated directly from positions, velocities and acceleration of individual particles.

Parallely with the PIC package is nowadays developed package RADIATION by David Břeň in frame of his PhD studies [66, 75]. Data from the PIC program (particle velocities and positions) are written to data file rad.dpc and transferred to the RADIATION package. We have to save positions and velocities of the particles from former times to be able to calculate radiation fields from retarded potentials. This is time and memory consuming and it can be done only for several thousands of particles. Nevertheless it can be important for investigation of characteristic behavior of the radiating filament. From the robust PIC model some “representative” particles have to be chosen.

Basics

Intensity of radiation can be calculated from equation derived from the Maxwell set of equations

$$\begin{aligned}
 I &= \mathbf{E}\mathbf{E}^* \quad ; \\
 \mathbf{E} &\cong \frac{\mathbf{n}}{\kappa^3 R} \times \left(\left(\mathbf{n} - \frac{\mathbf{v}}{c} \right) \times \frac{\dot{\mathbf{v}}}{c} \right) \Bigg|_{t'} \quad ; \\
 \kappa &\equiv \left(1 - \frac{\mathbf{n} \cdot \mathbf{v}}{c} \right) \quad ; \\
 \mathbf{n} &\equiv \frac{\mathbf{R}}{R} .
 \end{aligned} \tag{35}$$

From relation (35) we can obtain time dependence of the radiation intensity from charged particle at position \mathbf{R} of the observer.

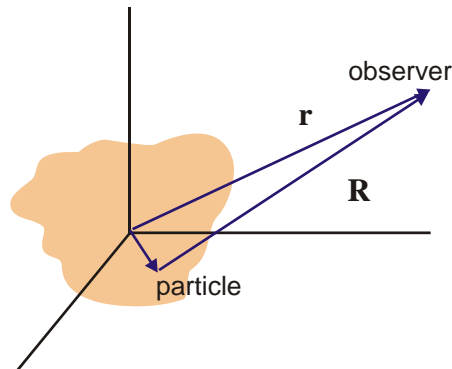


Fig. 43: Meaning of the relevant vectors

The particle moves with velocity \mathbf{v} and acceleration $\dot{\mathbf{v}}$. The whole calculation must be done in retarded time t' . The power radiated into cone $d\Omega$ is calculated from relation

$$\frac{dP}{d\Omega} = \frac{e^2}{16\pi^2 \epsilon_0 c} \frac{\left| \mathbf{n} \times \left(\left(\mathbf{n} - \frac{\mathbf{v}}{c} \right) \times \frac{\dot{\mathbf{v}}}{c} \right) \right|^2}{(1 - \mathbf{n}\beta)^5} . \quad (36)$$

The fields are projected on a far sphere (θ, ϕ). Nowadays only radiative fields are displayed ($I \sim 1/r^2$) and the space intensity distribution does not depend on the distance of the projection sphere. In future non-radiative fields, sufficiently near the filament, will be treated as well. In this case the distance of the projection sphere will be important parameter.

Implementation

An example of the transferred data file (between PIC package and RADIATION package) is in Table 15. The data file stores 6 REAL(4) values for every particle and time step (24 bytes). For a great number of particles the size of the data file can be enormous.

Table 15: Head and a small part of the transferred data file

Particle in Cell Simulation Results					
31.25000	62.50000	62.50000			
50	4200	4200		1200	
-1.000000	1.000000	1.000000		8.000000	
@FRAME	0.10				
@ELECTRONS					
1.222	8.079	7.477	9.009	2.282	-1.134
4.088	7.294	8.802	-2.282	-0.052	-0.412
6.903	9.208	9.252	2.213	-1.150	0.610
20.273	7.837	7.681	-1.227	1.535	-1.835
10.869	8.041	9.455	3.056	-2.245	-0.095
6.389	8.293	8.745	-1.802	2.330	0.846
20.755	7.963	9.422	0.503	0.404	3.757
.....					

In the program package the intensity is displayed by relative intensity on a far sphere. The relative intensity is represented by changing RGB color components. The maximum intensity is white: RGB=(255,255,255), zero intensity black: RGB=(0,0,0). The colors between these two values were taken as linear combinations of vectors red = (255,0,0), green = (0,255,0) and blue = (0,0,255).

There are two possible schemes: “cold” and “warm” one. Furthermore a window with time dependence of the total radiated intensity can be displayed. The input data are entered through a dialog window. The program was written in FORTRAN CVF 6.5A. The far projection sphere orientation is depicted in Fig. 45:

Some preliminary tests

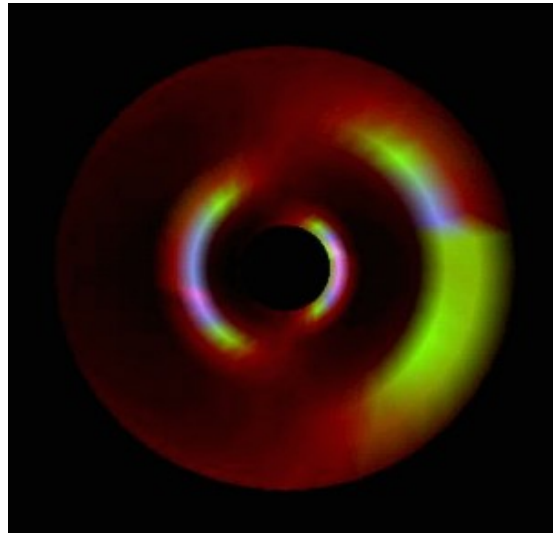


Fig. 44: Typical intensity in the case of circular motion: cross section of the intensity dependence.

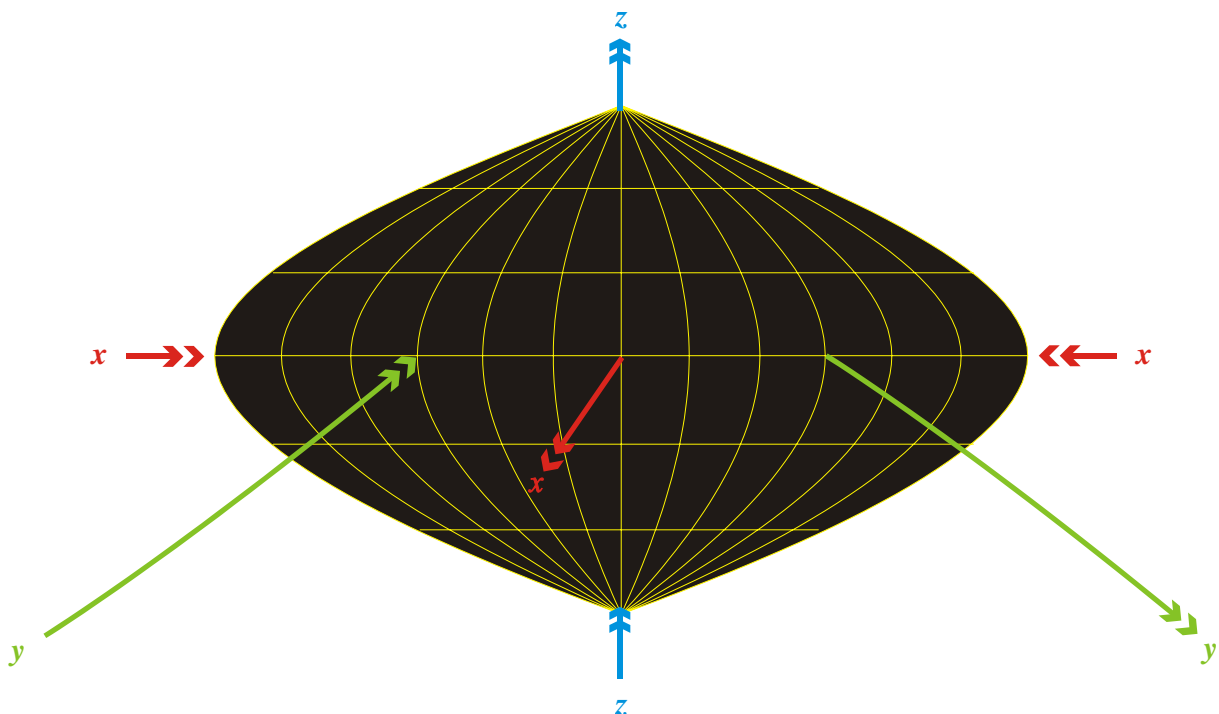


Fig. 45: Far projection sphere in the program package RADIATION.

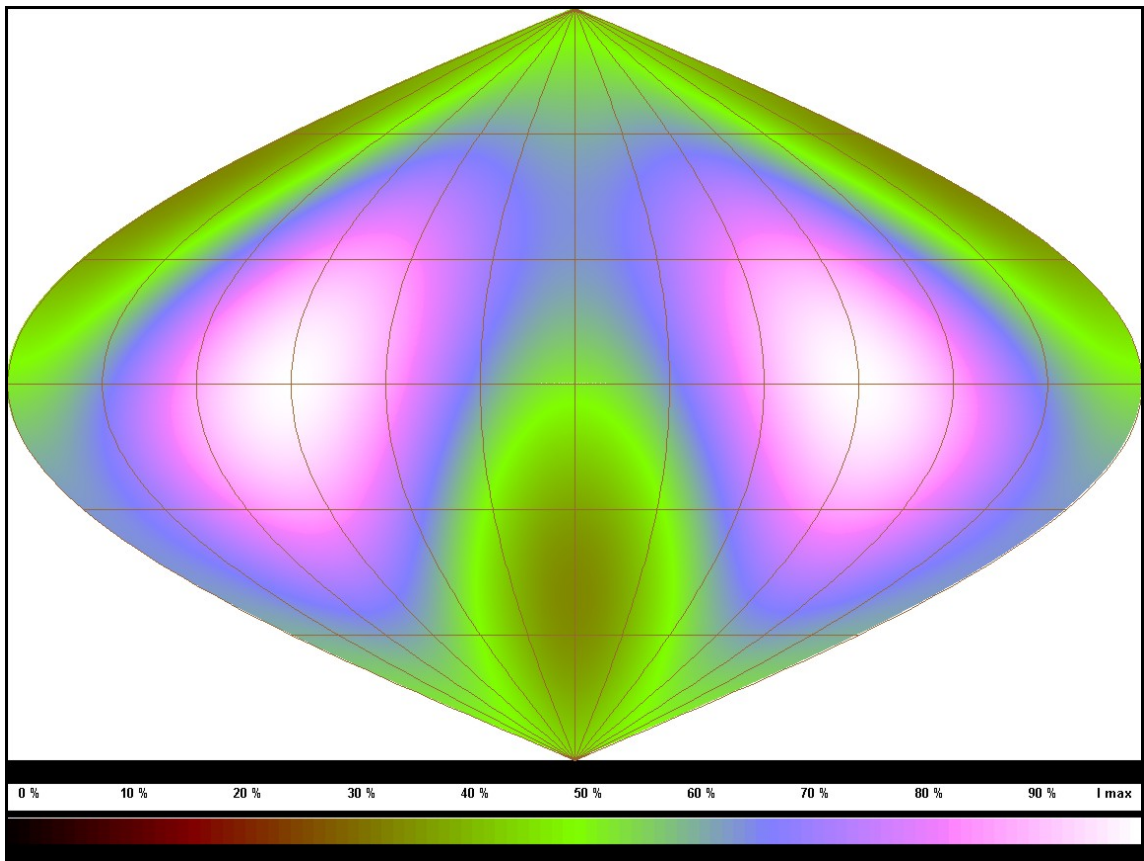


Fig. 46: Projection of intensity on a far sphere. Fiber oriented vertically (50 particles).

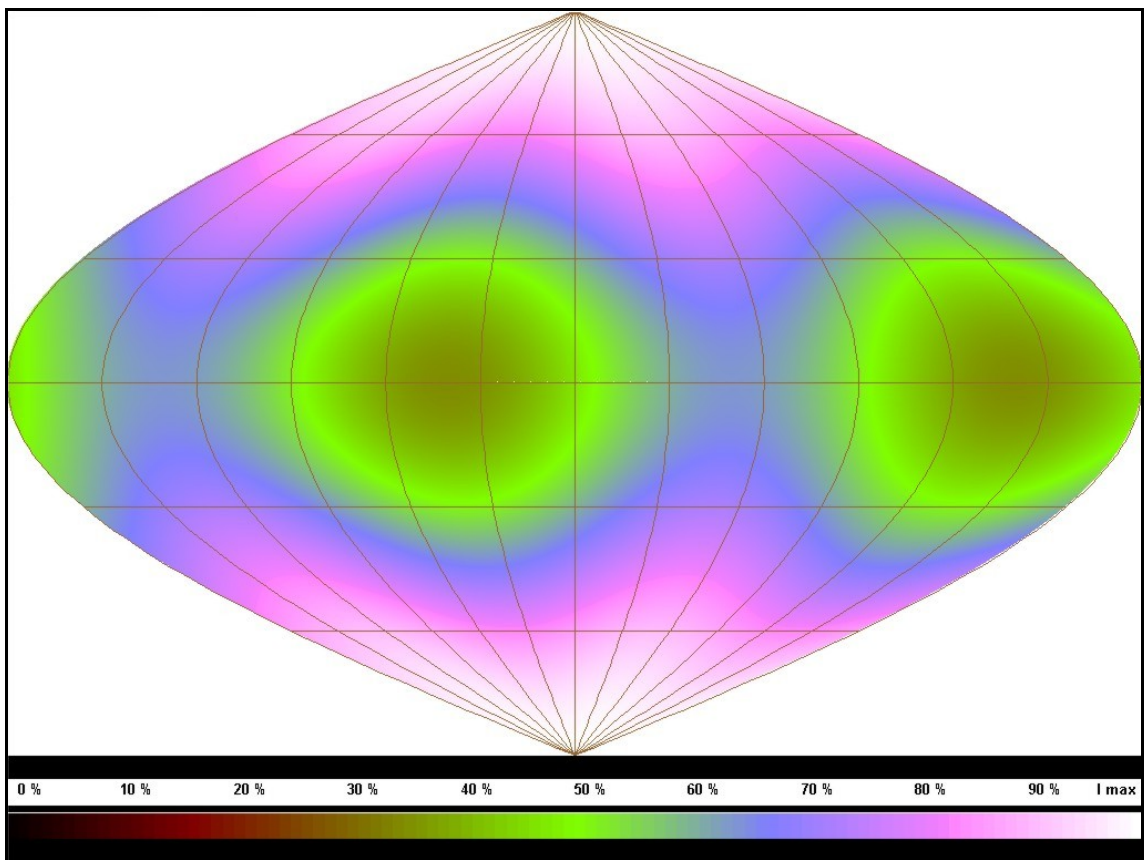


Fig. 47: Projection of intensity on a far sphere. Fiber oriented horizontally (50 particles).

3.6. Role of the Dust

Dust particles in plasma can influence plasma behavior dominantly. For example dust particles completely change conditions during radiation, the dust particles can radiate in continuum. This phenomenon can be cardinal for large plasma formations such as space nebulas. The dust can be responsible for sufficient exhaust of energy during creation of the stars. In large systems the charged dust particles interact not only via electromagnetic forces but also via gravitational ones. And gravitational interaction fetches in a wide new class of phenomena, new kinds of instabilities, which can for example cause star formation (Jeans criterion). But in lab plasma the presence of dust particles can completely change the plasma behavior as well. In the dust plasma, there are three typical plasma frequencies

$$\omega_{pe} = \sqrt{\frac{n_e Q_e^2}{m_e \epsilon_0}}; \quad \omega_{pi} = \sqrt{\frac{n_i Q_i^2}{m_i \epsilon_0}}; \quad \omega_{pd} = \sqrt{\frac{n_d Q_d^2}{m_d \epsilon_0}} \quad (37)$$

The dust grains are responsible for ultra low frequency wave modes, ions for magnetoacoustic modes and electrons dominantly modify the propagation of electromagnetic waves through the plasma. The dust grains can be charged both positively and negatively.

How to treat dust grains in PIC or PIC-like models? We have not only to add next type of heavy charged particles into the model but in most cases also gravitational interaction.

The basic interactions are described by scalar and vector potential of the electromagnetic force and by the gravitational potential. For low frequency modes the Laplace–Poisson equations for the potentials

$$\Delta\varphi = -\frac{\rho_e}{\epsilon_0}; \quad \Delta\mathbf{A} = -\mu_0 \mathbf{j}; \quad \Delta\varphi_g = 4\pi G \rho_m \quad (38)$$

have to be solved by some field solver. It is fortunate that the gravitational equation is in our approximation of the same type as the other two and the same solver can be used.

At the first glance it seems that adding dust particles into the PIC code need not to be a serious problem: one more type of particles and one more equation for gravitational potential. The equation of motion have to be slightly modified, the gravitational term must be introduced for dust particles

$$\frac{d}{dt}(m_a \mathbf{v}_a) = Q_a (\mathbf{E} + \mathbf{v}_a \times \mathbf{B}) - m_a \nabla \varphi_g. \quad (39)$$

The generalization of our PIC package in the sense sketched out above will be the motive of our endeavor in near future.

3.7. Animations

Very attractive outputs of our PIC model are various animations. We can animate the time evolution of the plasma fiber shape, the time evolution of fields in some cross sections, evolution of phase diagrams, radiation from the fiber, etc. These parts of our work are beyond the possibilities of printed material and beyond the scope of this dissertation. One can familiarize with it on our server www.aldebaran.cz.

4. SUPPORTING THEORY ADD-INNS

4.1. Filament Equilibrium (non-helical)

Let us solve the equilibrium of plasma column with axial current density and azimuthal magnetic field (pure z -pinch) in cylindrical coordinate system given in Fig. 48.

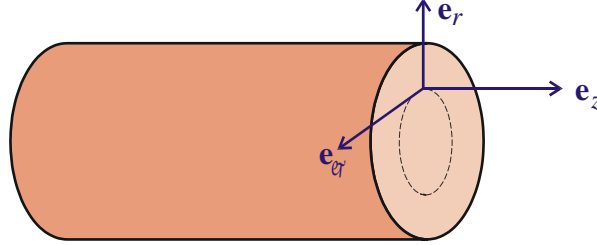


Fig. 48: Cylindrical coordinate system

Assuming cylindrical symmetry we have to determine (in the simplest model) current density, magnetic field and pressure dependences $j(r)$, $B(r)$, $p(r)$. During the equilibrium the Lorentz force density has to be balanced by the pressure gradient

$$0 = -\nabla p + \mathbf{j} \times \mathbf{B} \quad (40)$$

and current density is given by the Ampere law

$$\text{rot } \mathbf{H} = \mathbf{j}_C . \quad (41)$$

On the right hand side there is conductive current density. The Maxwell displacement current is zero in the equilibrium. Introducing

$$\mathbf{B} \equiv \mu_0(\mathbf{H} + \mathbf{M}) ; \quad \text{rot } \mathbf{M} = \mathbf{j}_M , \quad (42)$$

Eq. (41) can be rewritten into the well known form

$$\text{rot } \mathbf{B} = \mu_0(\mathbf{j}_C + \mathbf{j}_M) = \mu_0 \mathbf{j} . \quad (43)$$

In the expressions above \mathbf{j} is the total current density, \mathbf{j}_C is the conductive part, \mathbf{j}_M is the magnetization current density and \mathbf{M} is the magnetization. Substituting the current density from Eq. (43) into Eq. (40), the equilibrium condition in cylindrical coordinates will take a form

$$\frac{B^2}{\mu_0 r} + \frac{d}{dr} \left(\frac{B^2}{2\mu_0} + p \right) = 0 . \quad (44)$$

Forces

The equilibrium condition (44) must be granted both inside and outside the filament. In any case there are three balanced forces:

$$\begin{aligned}
 f_R &\equiv -\frac{B^2}{\mu_0 r}, & \text{curvature force density;} \\
 f_B &\equiv -\frac{d}{dr}\left(\frac{B^2}{2\mu_0}\right), & \text{magnetic pressure gradient;} \\
 f_P &\equiv -\frac{dp}{dr}, & \text{plasma pressure gradient.}
 \end{aligned}
 \tag{45}$$

The curvature force density corresponds with the non-scalar part $B_i B_j / \mu_0$ of the Maxwell stress tensor. In the filament interior all the three force densities are nonzero. In the filament exterior the plasma pressure gradient is zero; magnetic field can be calculated from the Ampere law as $B(r) = \mu_0 I / (2\pi r)$ and therefore

$$f_R = -\frac{\mu_0 I^2}{4\pi^2 r^3}, \quad f_B = +\frac{\mu_0 I^2}{4\pi^2 r^3}, \quad f_P = 0; \quad r \geq R. \tag{46}$$

Outside the filament the gradient of magnetic pressure is balanced by the curvature force density.

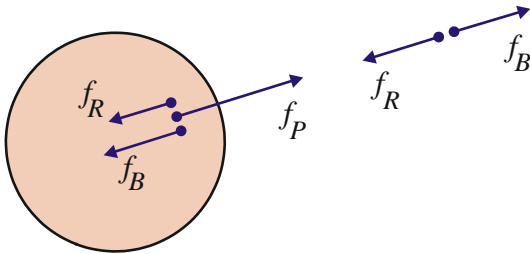


Fig. 49: Force equilibrium inside and outside the filament.

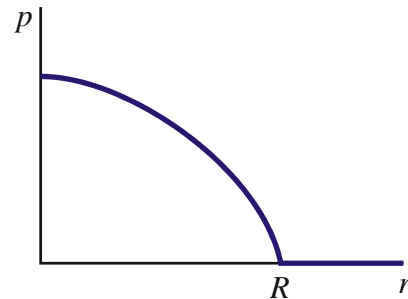


Fig. 50: Pressure dependence inside and outside the filament.

On the filament surface condition (as on the star surface in gravitation) $p(R) = 0$ is required.

Currents

The total current density in the simple filament (cylindrical filament with axial current) described above consists from three major parts [34]

$$\begin{aligned}
j_{\nabla B} &= -\frac{p}{B^2} \frac{\partial B}{\partial r}, & \text{gradient } B \text{ drift current ;} \\
j_R &= \frac{p}{rB}, & \text{curvature drift current ;} \\
j_M &= -\frac{1}{r} \frac{\partial}{\partial r} \left(\frac{rp}{B} \right), & \text{magnetization current .}
\end{aligned} \tag{47}$$

The first component is caused by the different gradient B drift of the electrons and ions, the second component is caused by the different curvature drift of the electrons and ions and the last component is a contribution from a charged system of particles rotating along magnetic field lines in non homogeneous field (the Larmor radii of neighboring particles differ and cause nonzero current).

The sum of these three components gives the equilibrium condition (40) with the total current divided into three parts:

$$\begin{aligned}
j_{\nabla B} + j_R + j_M &= -\frac{p}{B^2} \frac{\partial B}{\partial r} + \frac{p}{rB} - \frac{1}{r} \frac{\partial}{\partial r} \left(\frac{rp}{B} \right) = -\frac{1}{B} \frac{\partial p}{\partial r} \quad \Rightarrow \\
(j_{\nabla B} + j_R + j_M)B &= -\frac{\partial p}{\partial r}
\end{aligned}$$

Equilibrium in the cylindrical symmetry

Under assumption that current density is a power-step function of radius, the equilibrium solution can be found easily. The case $j = \text{const}$ is the well-known Bennett solution.

Table 16: Power-step equilibrium solution (non-helical filament)

variable	interior ($\xi \leq 1$)	exterior ($\xi > 1$)
$J(\xi)$	$I\xi^\alpha$	I
$j(\xi)$	$\frac{I}{\pi R^2} \frac{\alpha}{2} \xi^{\alpha-2}$	0
$B(\xi)$	$\frac{\mu_0 I}{2\pi R} \xi^{\alpha-1}$	$\frac{\mu_0 I}{2\pi R} \xi^{-1}$

$p(\xi)$	$\frac{\mu_0 I^2}{4\pi^2 R^2} \begin{cases} \frac{\alpha/2}{\alpha-1} (1-\xi^{2\alpha-2}); & \alpha \neq 1 \\ -\ln \xi; & \alpha = 1 \end{cases}$	0
$f_R(\xi)$	$-\frac{\mu_0 I^2}{4\pi^2 R^3} \xi^{2\alpha-3}$	$-\frac{\mu_0 I^2}{4\pi^2 R^3} \xi^{-3}$
$f_B(\xi)$	$-\frac{\mu_0 I^2}{4\pi^2 R^3} (\alpha-1) \xi^{2\alpha-3}$	$+\frac{\mu_0 I^2}{4\pi^2 R^3} \xi^{-3}$
$f_P(\xi)$	$+\frac{\mu_0 I^2}{4\pi^2 R^3} \alpha \xi^{2\alpha-3}$	0
$j_{\nabla B}(\xi)$	$-\frac{I}{\pi R^2} \frac{\alpha}{4} (\xi^{-\alpha} - \xi^{\alpha-2})$	0
$j_R(\xi)$	$\frac{I}{\pi R^2} \begin{cases} \frac{\alpha/4}{\alpha-1} (\xi^{-\alpha} - \xi^{\alpha-2}); & \alpha \neq 1 \\ -\frac{\ln \xi}{2\xi}; & \alpha = 1 \end{cases}$	0
$j_M(\xi)$	$\frac{I}{\pi R^2} \begin{cases} -\frac{\alpha/4}{\alpha-1} [(2-\alpha)\xi^{-\alpha} - \alpha \xi^{\alpha-2}]; & \alpha \neq 1 \\ \frac{1}{2\xi}; & \alpha = 1 \end{cases}$	0

The total current passing through the $\langle 0, r \rangle$ area is denoted as

$$J(r) \equiv \int_0^r 2\pi r j(r) dr. \quad (48)$$

The non-dimensional radius

$$\xi = \frac{x}{R} \quad (49)$$

is used in Table 16, $\xi = 0$ is the filament centre, $\xi = 1$ is the filament surface. Assuming $J(\xi)$ to be power step function with the exponent α , the current density dependence can be calculated from the definition (48), magnetic field from the Ampere law and the pressure from the equilibrium condition (44) with boundary condition $p(1) = 0$. From Eq. (45) the force densities

can be derived and from (47) the current densities. The result of the calculation is in the Table 16.

Conclusions

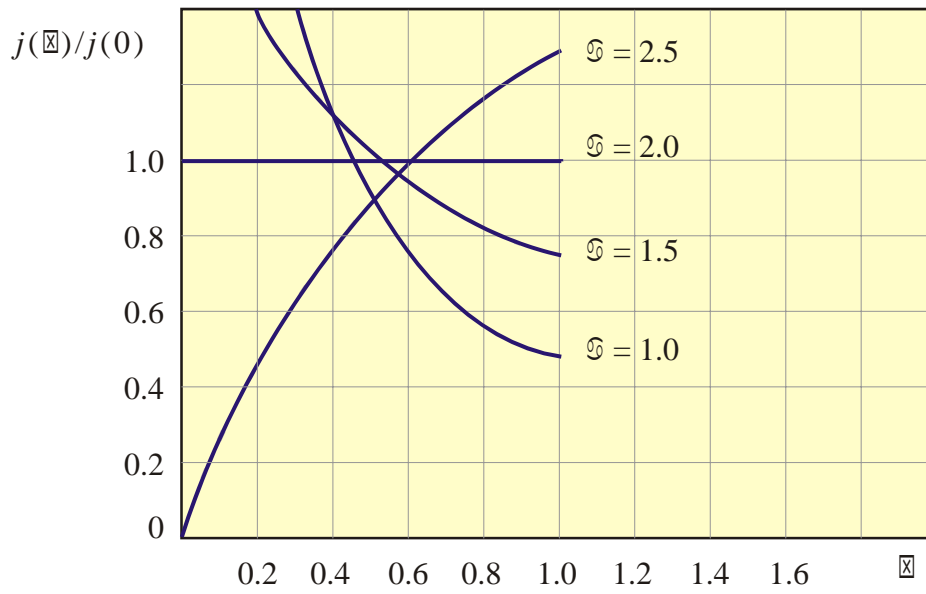
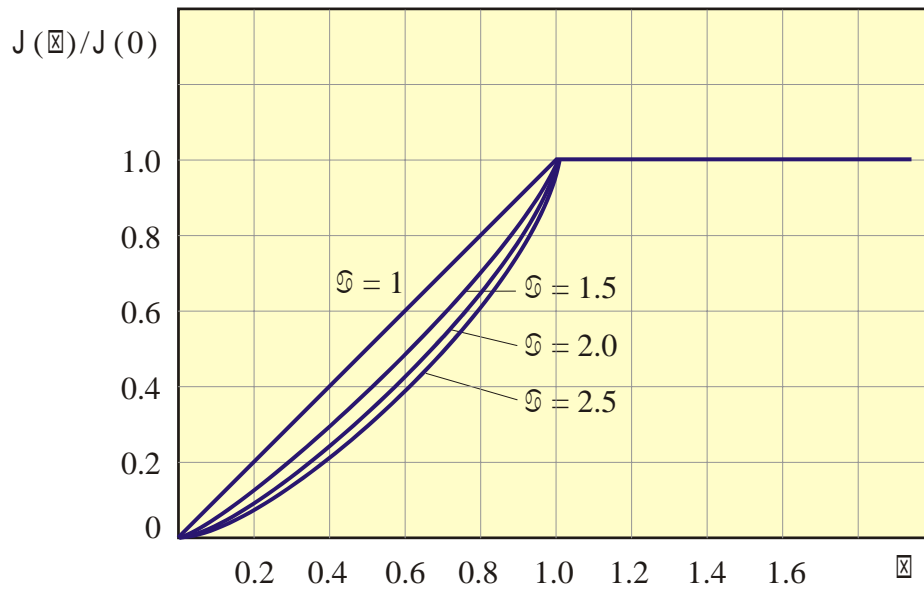
Some results are plotted in Fig. 51. The divergent parts of current density dependencies originate in the total current decomposition (47). The sum of the three components does not diverge and the divergence has no real meaning. The case $\alpha = 1$ can be derived as a limit of the general case. Small changes in parameter cause sufficient changes in the character of the solution. Let us characterize the most important cases:

$\alpha = 1.0$: The current passes mostly in the filament centre. Magnetic field is constant in the whole interior. The pressure diverges in the centre. This case describes filament with dense core, it is a limit of $\alpha \neq 1$ filaments, which solution does not have any divergences.

$\alpha = 1.5$: The current density has similar dependence as in the previous case. The current is located in the filament core. Magnetic field increases with the radius as convex function. The pressure linearly decreases from the centre towards the boundary.

$\alpha = 2.0$: This is the well-known Bennett solution. The current density is constant in the whole interior. Magnetic field increases linearly with the radius and the pressure decreases parabolically from the centre towards the boundary (Bennett profile). The sum of gradient B current density and curvature drift current density is zero. The only remaining current is the magnetization current.

$\alpha = 2.5$: Current density has the biggest value on the boundary and the current passes mostly along the filament surface. The magnetic field increases towards the filament boundary but not linearly. The pressure dependence is similar to the Bennett one.



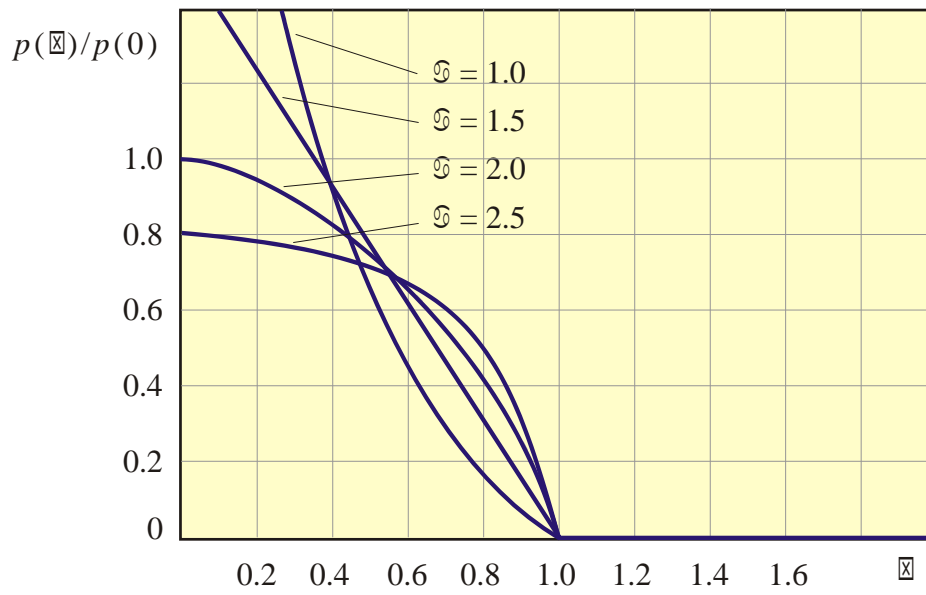
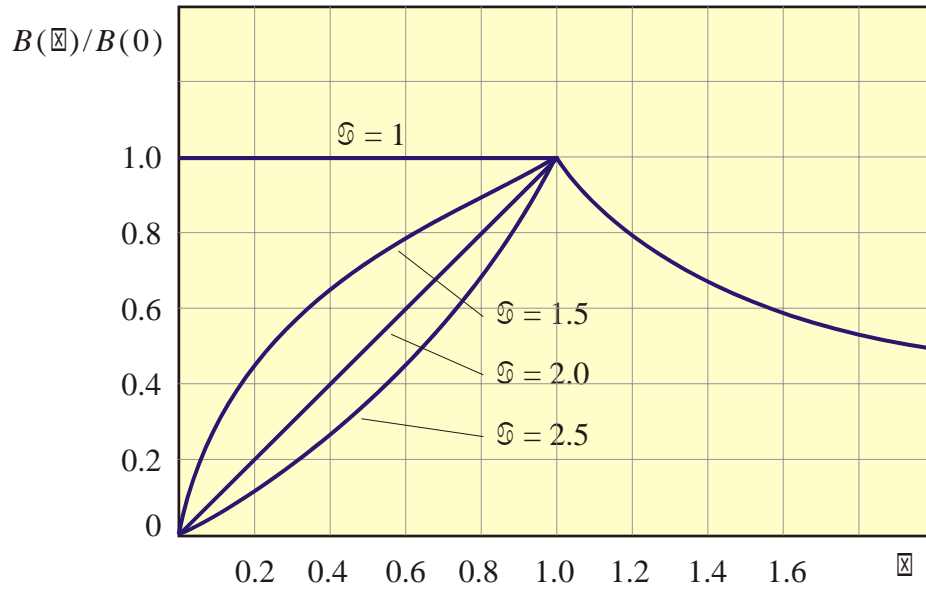


Fig. 51: Power-step equilibrium solution (non-helical filament)

4.2. Radiating Filament Equilibrium (non-helical)

Relatively simple model of radiating z -pinch filament we have proposed in [35, 45]. Let us assume axial current density only and corresponding azimuthal magnetic field. In the cylindrical geometry and one fluid MHD model, there are five equilibrium functions to be obtained: current density $j(r)$, concentration $n(r)$, magnetic field $B(r)$, pressure $p(r)$ and temperature $T(r)$.

Force equilibrium equation

Combining standard force equilibrium equation

$$-\nabla p + \mathbf{j} \times \mathbf{B} = 0 \quad (50)$$

with the Ampere law

$$\text{rot } \mathbf{B} = \mu_0 \mathbf{j}, \quad (51)$$

we obtain in cylindrical geometry the equilibrium equation

$$\frac{B^2}{\mu_0 r} + \frac{d}{dr} \left(\frac{B^2}{2\mu_0} + p \right) = 0. \quad (52)$$

If we would know magnetic field dependence in some manner, we can calculate pressure from this ordinary differential equation. As input parameter of the equilibrium configuration serves the central pressure $p(0)$. Integrating equation (52) we can determine the pressure dependence $p(r)$ and from the condition $p(R) = 0$ (zero surface pressure) the equilibrium pinch radius. If we are looking for current density and magnetic field dependences as well, it is better to let the equilibrium equation in shape (50) which is in cylindrical geometry

$$\frac{dp}{dr} = -j(r)B(r). \quad (53)$$

Radiation equilibrium

In pinch, the Joule heating is compensated by the radiation processes. There are three basic mechanisms of the radiation: recombination, bremsstrahlung and synchrotron radiation. Corresponding power densities for cylindrical pinch can be written as [35, 45]

$$\begin{aligned} P_R &= P_{R0} n^2 T^{-1/2} && \text{recombination,} \\ P_B &= P_{B0} n^2 T^{1/2} && \text{bremsstrahlung,} \\ P_S &= P_{S0} n^2 T^2 && \text{synchrotron radiation.} \end{aligned} \quad (54)$$

The proportionality constants P_{R0} , P_{B0} , P_{S0} depend strongly on the plasma type, its impurities and degree of ionization. Some estimates of the values are given in [35, 45]:

$$\begin{aligned} P_{R0} &\approx 5 \times 10^{-36} z^5 \text{ Wm}^3 \text{K}^{-1/2} , \\ P_{B0} &\approx 1.5 \times 10^{-41} z^3 \text{ Wm}^3 \text{K}^{1/2} , \\ P_{S0} &\approx 5 \times 10^{-52} z^2 \text{ Wm}^3 \text{K}^{-2} . \end{aligned} \quad (55)$$

Temperature dependence (54) of the radiation power is plotted in Fig. 9. The recombination is dominant for the temperatures bellow 10^5 K, the bremsstrahlung in the temperature interval $(10^5 \div 10^7)$ K and synchrotron radiation above 10^7 K.

From Eq. (54) we can for all types of radiation cooling write a simple formula

$$P(r) = \frac{j^2}{\sigma} = P_0 n^2 T^\beta \quad [\text{W/m}^3]. \quad (56)$$

The coefficient β is $-1/2$ for recombination, $1/2$ for bremsstrahlung and 2 for synchrotron radiation.

Combining (56) with the Spitzer formula for conductivity

$$\sigma = \frac{\sigma_0}{z \ln \Lambda} T^{3/2}, \quad \sigma_0 = 4.1 \times 10^{-3} \text{ K}^{-3/2} \Omega^{-1} \text{ m}^{-1} \quad (57)$$

we obtain the second basic equation of the z -pinch equilibrium

$$j(r) = A n(r) T^{\beta/2+3/4}(r); \quad A \equiv \sqrt{\frac{\sigma_0 P_0(z)}{z \ln \Lambda}} . \quad (58)$$

Ampere law

The interrelation between current density and magnetic field in the z -pinch is given by means of the Ampere law (51), in cylindrical geometry

$$\frac{1}{r} \frac{d}{dr} (rB) = \mu_0 j . \quad (59)$$

After simple manipulation we obtain the third basic equation of the equilibrium set of the equations:

$$\frac{dB}{dr} = \mu_0 j(r) - \frac{B(r)}{r}; \quad B(0) = 0 . \quad (60)$$

Equation of state

The concentration, temperature and pinch pressure fulfill some equation of state, the simplest possible form is

$$p(r) = (1 + Z)n(r)kT(r) . \quad (61)$$

It is of course possible to investigate more sophisticated equations of state and their influence on the z -pinch behavior. But for the purpose of the radiation equilibrium calculations the shape (61) is satisfactory.

Ohm's law

In equilibrium the Ohm's law has a simple form

$$\mathbf{j} = \sigma \mathbf{E} . \quad (62)$$

The electric field is axial and irrotational: $\text{rot } E = -\partial B/\partial t = 0$ implies $E_z(r) = \text{const}$. Combination with the Spitzer formula (57) gives

$$j(r) = KT^{3/2}(r) . \quad (63)$$

In higher temperature areas conductivity and current density is higher. The constant K can be estimated from average current density and temperature in the z -pinch.

Algebraic and differential equations

The set of equations (53), (58), (60), (61) and (63) is internally consistent set of mixed algebraic and differential equations. The algebraic equations can be eliminated in a following way: We substitute into Eq. (58) concentration from Eq. (61) and after that temperature from Eq. (63). From the resulting equation we determine the current density as a function of pressure. After similar manipulations we obtain concentration and temperature as a unique function of pressure as well:

$$\begin{aligned} j &= C_j p^{\frac{6}{7-2\beta}} ; & C_j &\equiv \left(\frac{A}{(1+z)k} \right)^{\frac{6}{7-2\beta}} K^{\frac{1-2\beta}{7-2\beta}} \\ T &= C_T p^{\frac{4}{7-2\beta}} ; & C_T &\equiv \left(\frac{A}{K(1+z)k} \right)^{\frac{4}{7-2\beta}} . \\ n &= C_n p^{\frac{3-2\beta}{7-2\beta}} ; & C_n &\equiv \left(\frac{1}{(1+z)k} \right)^{\frac{3-2\beta}{7-2\beta}} \left(\frac{K}{A} \right)^{\frac{4}{7-2\beta}} \end{aligned} \quad (64)$$

Let us remark, that radiation equilibrium model implicitly leads to polytropic behavior of the plasma. As we can see from the last equation in (64), the polytropic coefficient has value

$$\gamma = \frac{7 - 2\beta}{3 - 2\beta} . \quad (65)$$

Remaining differential equations (53) and (60) can be with the help of (64) transferred into nonlinear set of ordinary differential equations for two variables $p(r)$ and $B(r)$:

$$\begin{aligned} \frac{dp}{dr} &= -C_j p^\alpha B, \\ \frac{dB}{dr} &= \mu_0 C_j p^\alpha - \frac{B}{r}, \end{aligned} \quad (66)$$

where α is power exponent of the pressure given via the radiation exponent β :

$$\alpha = \frac{6}{7 - 2\beta} . \quad (67)$$

In following Table 17 some typical values of these exponents are given for several situations:

Table 17: Exponents and coefficients in the radiation z-pinch model

radiation exponent β	pressure exponent α	polytropic coefficient γ	kind of radiation
0.5	0.75	2	recombination
0	0.86	2.33	
0.5	1	3	bremsstrahlung
1	1.2	5	
1.5	1.5	∞	synchrotron
2	2	-3	
2.5	3	-1	

As initial condition of the set of equations (66) will be chosen $p(0) = p_0$, $B(0) = 0$. Central pressure p_0 is fundamental parameter of the equilibrium configuration. For numerical calculations we have to know the value

$$\lim_{r \rightarrow 0} \frac{B(r)}{r} = \lim_{r \rightarrow 0} \frac{dB}{dr} = \frac{1}{2} \mu_0 C_j p_0^\alpha. \quad (68)$$

The first equality follows from the L'Hospital rule and the second one directly from the differential equation for the magnetic field.

The surface of the radiating pinch cannot be defined by standard relation $p(R) = 0$, because $dp/dr = 0$ follows from the pressure equation and the curve $p(r)$ does not intersect the r axis. The surface of the radiating pinch is not sharp. The surface has to be defined in some alternative way, for example the surface can be treated as the area with maximum value of the magnetic field.

Non-dimensional variables

The non-dimensional variables in the model can be chosen according to the scheme

$$\begin{aligned} \bar{p} &= \frac{p}{p_0}; & p_0 &\equiv p(0), \\ \bar{B} &= \frac{B}{B_0}; & B_0 &\equiv \sqrt{\mu_0 p_0}, \\ \bar{j} &= \frac{j}{j_0}; & j_0 &\equiv C_j p_0^{\frac{6}{7-2\beta}}, \\ \bar{T} &= \frac{T}{T_0}; & T_0 &\equiv C_T p_0^{\frac{4}{7-2\beta}}, \\ \bar{n} &= \frac{n}{n_0}; & n_0 &\equiv C_n p_0^{\frac{3-2\beta}{7-2\beta}}, \\ \bar{r} &= \frac{r}{r_0}; & r_0 &\equiv \frac{1}{C_j \sqrt{\mu_0 p_0^{2\alpha-1}}}. \end{aligned} \quad (69)$$

The set of differential equations (66) have non-dimensional form

$$\begin{aligned} \frac{d\bar{p}}{d\bar{r}} &= -\bar{p}^\alpha \bar{B}; \bar{p}(0) = 1, \\ \frac{d\bar{B}}{d\bar{r}} &= \bar{p}^\alpha - \frac{\bar{B}}{\bar{r}}; \bar{B}(0) = 0, \lim_{\bar{r} \rightarrow 0} \frac{\bar{B}}{\bar{r}} = \frac{1}{2}, \end{aligned} \quad (70)$$

and algebraic equations (64) acquire a simple non-dimensional shape

$$\bar{j} = \bar{p}^{\frac{6}{7-2\beta}}, \quad \bar{j} = \bar{p}^{\frac{6}{7-2\beta}}, \quad \bar{T} = \bar{p}^{\frac{4}{7-2\beta}}, \quad \bar{n} = \bar{p}^{\frac{3-2\beta}{7-2\beta}}. \quad (71)$$

The equations (70) and (71) are prepared for numerical calculation by standard numerical methods.

Conclusions

The model proposed has only one input parameter (central pressure), provides unambiguous solution of the equilibrium with radiation processes. Compared to standard Bennett solution without radiation the model predicts “soft” pinch surface, some solutions have central depletion of the concentration and pressure (hollow pinch), temperature gradient have to be nonzero, chemical elements can be separated according to ionization potential and the radiation can be responsible for radial charge separation.

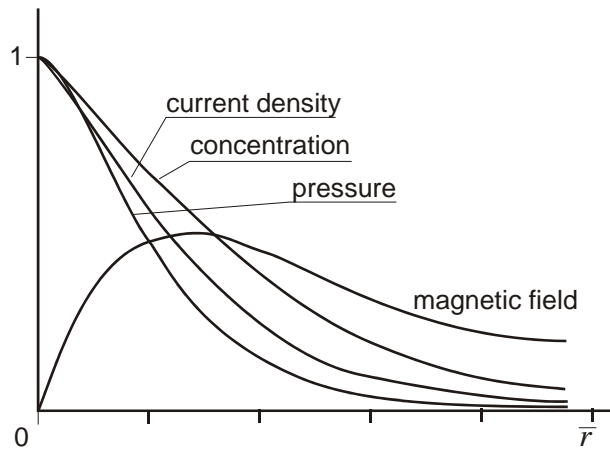


Fig. 52: Numerical solution for $\beta = -1/2$.

4.3. Helical Structures

Helicity and Beltrami condition

Helicity can be defined for the vector field \mathbf{V} by the relation

$$H(t, \mathbf{x}) \equiv \mathbf{V} \cdot \text{rot } \mathbf{V} \quad (72)$$

or integral helicity

$$K(t) = \int_V H(t, \mathbf{x}) dV \quad (73)$$

Helicity is scalar field, which is zero for all fields with $\text{rot } \mathbf{V} = 0$. For vortices with circular field lines the helicity is zero as well. The fields with helical field lines have nonzero helicity proportional to $\cos \beta$ (β - pitch angle). For the plasma filament structure, the following helicity definitions may be meaningful (vector potential \mathbf{A} , magnetic field induction \mathbf{B} , current density \mathbf{j} , electric field \mathbf{E} and velocity field \mathbf{v}):

$$\begin{aligned} H_A &= \mathbf{A} \cdot \text{rot } \mathbf{A} = \mathbf{A} \cdot \mathbf{B}, \\ H_B &= \mathbf{B} \cdot \text{rot } \mathbf{B} = \mu_0 \mathbf{j} \cdot \mathbf{B}, \\ H_j &= \mathbf{j} \cdot \text{rot } \mathbf{j} = -\frac{1}{\mu_0} \mathbf{j} \cdot \Delta \mathbf{B}, \\ H_E &= \mathbf{E} \cdot \text{rot } \mathbf{E} = -\mathbf{E} \frac{\partial \mathbf{B}}{\partial t}, \\ H_v &= \mathbf{v} \cdot \text{rot } \mathbf{v}. \end{aligned} \quad (74)$$

The vector field fulfilling the Beltrami property

$$\mathbf{V} \times \text{rot } \mathbf{V} = 0, \quad \text{or} \quad \text{rot } \mathbf{V} = \alpha \mathbf{V} \quad (75)$$

is very interesting from the helicity point of view. The coefficient of the proportionality between the field and its rotation may be a function of space and time variables. The Beltrami fields are helical, because

$$H \equiv \mathbf{V} \cdot \text{rot } \mathbf{V} = \alpha \mathbf{V} \cdot \mathbf{V} = \alpha V^2. \quad (76)$$

The α coefficient is the field helicity divided by quadrate of the field absolute value. For $\alpha = \text{const}$ and $\text{div } \mathbf{V} = 0$, the field \mathbf{V} satisfies Helmholtz equation

$$\Delta \mathbf{V} + \alpha^2 \mathbf{V} = 0. \quad (77)$$

It can be derived from (3) by applying the rot operator. In this case, the field \mathbf{V} is characteristic vector of the Laplacian operator in corresponding geometry.

Typical examples of the Beltrami fields are *ABC* flows [29]:

$$\mathbf{V} = (A \sin z + C \cos y, B \sin x + A \cos z, C \sin y + B \cos x). \quad (78)$$

For this field $\text{rot } \mathbf{V} = \mathbf{V}$ and $\Delta \mathbf{V} = -\mathbf{V}$. Chaotic regions exist in these flows.

In plasma physics, the magnetic field satisfies Beltrami condition in force free configuration with current density aligned along magnetic field, $\mathbf{j} \parallel \mathbf{B}$ (Birkeland current). In this case the Lorenz force density $\mathbf{j} \times \mathbf{B}$ is zero. This configuration has the lowest possible energy and plasma with energy dissipation tends to this configuration. The Beltrami condition can be derived from the Ampere law:

$$\mathbf{j} = \text{rot } \mathbf{B} / \mu_0 \wedge \mathbf{j} \parallel \mathbf{B}, \quad \Rightarrow \quad \mathbf{B} \times \text{rot } \mathbf{B} = 0, \quad \text{resp.} \quad \text{rot } \mathbf{B} = \alpha \mathbf{B}. \quad (79)$$

From the above it is obvious that the force free magnetic field is helical.

Magnetic helicity conservation

The conditions for magnetic helicity conservation were investigated in frame of Michal Stránský Diploma theses [65]. The magnetic helicity for vector potential is defined as

$$K = \int \mathbf{A} \cdot \text{rot } \mathbf{A} \, dV = \int \mathbf{A} \cdot \mathbf{B} \, dV \quad (80)$$

The total time differentiation gives

$$\frac{dK}{dt} = \int_V \left(\frac{\partial \mathbf{A}}{\partial t} \cdot \mathbf{B} + \mathbf{A} \cdot \frac{\partial \mathbf{B}}{\partial t} \right) dV + \int_S (\mathbf{A} \cdot \mathbf{B})(\mathbf{n} \cdot \mathbf{v}) dS. \quad (81)$$

In classical MHD the magnetic field time evolution is given by equation [84]

$$\frac{\partial \mathbf{B}}{\partial t} = \eta_M \Delta \mathbf{B} + \text{rot}(\mathbf{v} \times \mathbf{B}); \quad \eta_M \equiv \frac{1}{\sigma \mu_0}. \quad (82)$$

The first term represents magnetic field diffusion (η_M is magnetic diffusivity) and the second one changes of magnetic field due to tracking the plasma streamlines (so called frozen magnetic field). In ideal plasma the conductivity is high, the dissipative term is negligible and magnetic field lines are frozen into the plasma fluid. The magnetic field evolution is given by equation

$$\frac{\partial \mathbf{B}}{\partial t} = \text{rot}(\mathbf{v} \times \mathbf{B}). \quad (83)$$

In this case the second term in (81) is equal

$$\begin{aligned}
\int_V \mathbf{A} \cdot \frac{\partial \mathbf{B}}{\partial t} dV &= -\int_V \operatorname{div}[\mathbf{A} \times (\mathbf{v} \times \mathbf{B})] dV + \int_V (\mathbf{v} \times \mathbf{B}) \cdot \operatorname{rot} \mathbf{A} dV = \\
&= -\int_V \operatorname{div}[\mathbf{A} \times (\mathbf{v} \times \mathbf{B})] dV + \int_V (\mathbf{v} \times \mathbf{B}) \cdot \mathbf{B} dV = -\int_V \operatorname{div}[\mathbf{A} \times (\mathbf{v} \times \mathbf{B})] dV = \\
&= -\int_V \operatorname{div}[\mathbf{A} \times (\mathbf{v} \times \mathbf{B})] = -\int_S [(\mathbf{A} \cdot \mathbf{B})(\mathbf{v} \cdot \mathbf{n}) - (\mathbf{A} \cdot \mathbf{v})(\mathbf{B} \cdot \mathbf{n})] dS .
\end{aligned}$$

If the system under consideration has closed magnetic field lines (the system has to be sufficiently large to be this true), the normal component $\mathbf{B} \cdot \mathbf{n}$ of magnetic field on the surface is zero and last term vanishes. The non-vanishing term balances the last term in (81) and so we have

$$\frac{dK}{dt} = \int_V \frac{\partial \mathbf{A}}{\partial t} \cdot \mathbf{B} dV . \quad (84)$$

From the definition of electric field

$$\mathbf{E} = -\nabla \phi - \frac{\partial \mathbf{A}}{\partial t} \quad (85)$$

we can substitute the time derivative of vector potential into (84):

$$\frac{dK}{dt} = -\int_V (\mathbf{E} \cdot \mathbf{B} + \nabla \phi \cdot \mathbf{B}) dV = -\int_V \operatorname{div}(\phi \mathbf{B}) dV = -\int_S \phi (\mathbf{B} \cdot \mathbf{n}) dS = 0 . \quad (86)$$

The integral helicity is conserved under these assumptions:

1. Negligible magnetic field diffusion (high conductivity, zero resistivity)
2. Zero normal magnetic field component on the surface of the system (closed system field lines).

Magnetic helicity dissipation

If the system has closed magnetic field lines (zero normal magnetic field components) the only way how to change the total helicity is the magnetic field dissipation. Let us estimate the role of diffusion term in magnetic field equation. Following the procedure above step by step with diffusion term left in Eq. (82) we will obtain simple relation

$$\frac{dK}{dt} = -\frac{1}{\sigma} \int_V \mathbf{j} \cdot \mathbf{B} dV \quad (87)$$

The magnetic field energy is given by formula

$$W_M = \frac{1}{2\mu_0} \int_V B^2 dV \quad (88)$$

and the time derivation is

$$\frac{dW_M}{dt} = \frac{1}{\sigma} \int_V j^2 dV \quad (89)$$

Using Schwartz inequality $\mathbf{f} \cdot \mathbf{g} \leq \|\mathbf{f}\| \cdot \|\mathbf{g}\|$ in L^2 space [82] we obtain

$$\left| \frac{dK}{dt} \right| \leq \left(\frac{2}{\sigma\mu_0} W_M \left| \frac{dW_M}{dt} \right| \right)^{1/2}. \quad (90)$$

For reconnection phenomena we have to introduce typical length

$$L \equiv \frac{|K|}{W_M}. \quad (91)$$

This length is roughly equal to the system size if helical structure is developed well. The dissipation time constant can be defined by the relation

$$\tau_d = L^2 / \eta_M = L^2 \sigma \mu_0. \quad (92)$$

Assuming dissipation or reconnection process in finite isolated volume and finite time Δt , we will obtain from Eq. (90) by simple integration

$$\left| \frac{\Delta K}{K} \right| \leq \left(\frac{\Delta t}{\tau_d} \right)^{1/2}. \quad (93)$$

We can see that for quick phenomena ($\Delta t \ll \tau_d$) the total helicity change ΔK will be negligible. For example solar corona eruption with reconnection time $\Delta t \sim 1000$ s, linear dimensions $L \sim 1000$ km and diffusivity $\eta \sim 10^{-6} \text{ km}^2 \text{ s}^{-1}$ will give $\tau_d \sim 10^{12}$ s and $\Delta K / K < 3 \times 10^{-5}$.

Stationary solutions

In Michal Stranský Diploma Theses [65] was proved that there exist stationary solution with non zero helicity both for zero resistivity (frozen magnetic field, helicity conserves) and for non zero resistivity (helicity does not conserve). The solution with non zero resistivity is helical filament with interior hole along its axis. The conditions for helicity conservation

derived above (zero diffusion and zero normal magnetic field components) are sufficient conditions but not necessary conditions.

Diocotron instability

If, in the cylindrical pinch, the charge is separated in radial direction for some reasons, the radial electric field arises. As a consequence, the pinch azimuthally rotates due to particle drift in perpendicular E_r and B_z fields. On the pinch surface Kelvin-Helmholtz like instability called the *diocotron instability* evolves. The surface is modified into typical vortex structures [10]. The charge separation can be invoked by particle drifts, pinch radiation accompanying with the temperature gradient and some instabilities. The diocotron instability had been observed in many plasma arrangements and the azimuthal rotation can be the starting mechanism for the onset of the helical mode.

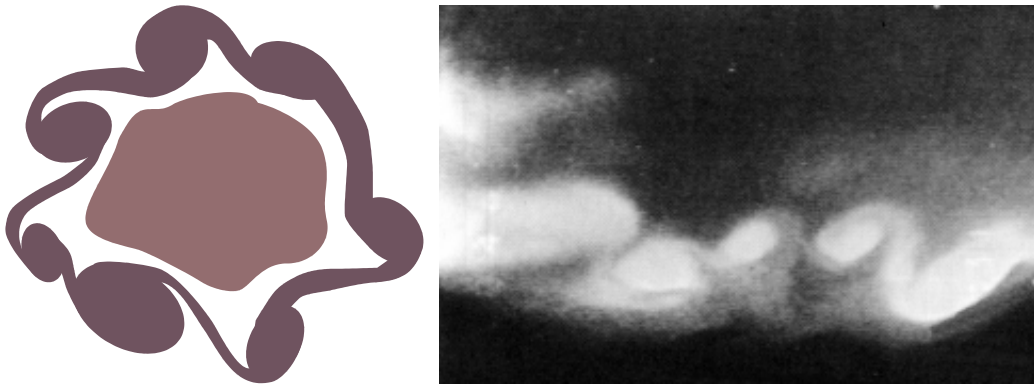


Fig. 53: Diocotron instability. Left: The pinch cross section. Right: Aurora in Alaska 1973 [10]

The radial violation of quasineutrality can be described in terms of concentration by simple formula

$$\Delta n = n_e - Zn_i = n_e (1 - f); \quad f \equiv \frac{Zn_i}{n_e} . \quad (94)$$

For $f \neq 1$ radial electric field arises. It can be calculated from Maxwell equation

$$\text{div } \mathbf{D} = -e(n_e - Zn_i), \quad (95)$$

which gives in cylindrical coordinates

$$\frac{1}{r} \frac{d}{dr} (r E_r) = -\frac{n_e e}{\epsilon_0} (1-f) . \quad (96)$$

This field together with axial magnetic field is responsible for azimuthal drift with the drift velocity

$$v_\varphi = \frac{E_r}{B_z} . \quad (97)$$

The vorticity of the velocity field is

$$\omega_{\mathbf{v}} \equiv \frac{1}{2} \text{rot } \mathbf{v} = \frac{1}{2r} \frac{\partial}{\partial r} \left(r \frac{E_r}{B_z} \right) = \frac{1}{2B_z} \frac{n_e e}{\epsilon_0} (f-1) = \frac{ne^2}{m_e \epsilon_0} \frac{m_e}{2e B_z} (f-1) = \frac{\omega_p^2}{2\omega_c} (f-1) . \quad (98)$$

The fundamental parameter for the development of the diocotron instability is

$$q \equiv \frac{\omega_v}{\omega_c} = \frac{\omega_p^2}{2\omega_c^2} (f-1) . \quad (99)$$

The diocotron instability is very frequent phenomenon. It is observed in many laboratory experiments, in space plasma as well as in numerical simulations. Even spiral arms of some galaxies have structures typical for the diocotron instability. Its characteristic picture can be found in current layers, curtain shapes of the auroras, etc.

The evolution of the diocotron instability provoked by surface pinch rotation can be dominant impulse to the rearrangement of the filament to helical structure. Both these processes seem to cohere; maybe they evolve all at once.

5. RESULTS AND CONCLUSIONS

1) Overview

A fully three dimensional Particle in Cell model of the plasma fiber had been developed in our department. The code is written in FORTRAN 95, implementation CVF (Compaq Visual Fortran) under Microsoft Visual Studio user interface. Five particle solvers (Newton, Runge-Kutta, Boris-Buneman, Leap-Frog and Canonical) and two field solvers (FFT and multigrid) are included in the model. The solvers have relativistic and non-relativistic variants. The model can deal both with periodical and non-periodical boundary conditions.

Plasma fiber and its surroundings is generated during the initiation process. The user can influence many parameters of the fiber, such as temperatures of electrons and ions, electric and magnetic fields, perturbations of the shape of the fiber and of the charged particle positions.

The PIC program package simulates the behaviour of the fiber, namely the evolution of magnetic field structures and turbulences.

The numerical solution of the particle motion and calculation of the electric and magnetic fields is the only one small part of the program package. There are many additional routines and collaborating program packages for computer diagnostics, graphical output and other calculations such as radiation, etc.

The field visualization is done via Line Integral Convolution method, the particles are visualized in several ways described above. The most interesting is the possibility of recording animations of the scene as avi files.

Diagnostic routines enabling to calculate quantities comparable with the experiments are also the integral part of the package.

The program package PIC was developed during five years and several diploma and doctoral students contributed to some parts of the package. In the following table there are main parts of package and their authors

PART	PURPOSE	AUTHOR
PIC	Basic part of the code	P. Kulhánek
INIT	Fiber initiation	P. Kulhánek
PS	Particle solver nonrelativistic	P. Kulhánek
PSR	Particle solver relativistic	D. Škandera
FFT	FFT field solver	R. Dejmek
MUDPACK	Multigrid Package field solver	C. A. John, NCAR, USA
MC	Monte Carlo collisions of the neutrals	D. Škandera
DIAG	Diagnostic routines	P. Kulhánek
LIC	Line Integral Convolution field visualization	O. Novák
VISUAL	Particle visualization and animations	M. Smetana
RADIATION	Radiation program package	D. Břeň, P. Kulhánek
DUST	Charged dust particles	V. Kaizr

2) Surface turbulences and helical structure onset

In the numerical simulations it had been proved, that surface turbulent phenomena can hang together with radial electric field perturbations. The perturbed field along with axial magnetic field causes azimuthal drift and the succeeding diocotron instability forms vortices evolving into structures with non-zero helicity. Typical magnetic fields are in Fig. 54.

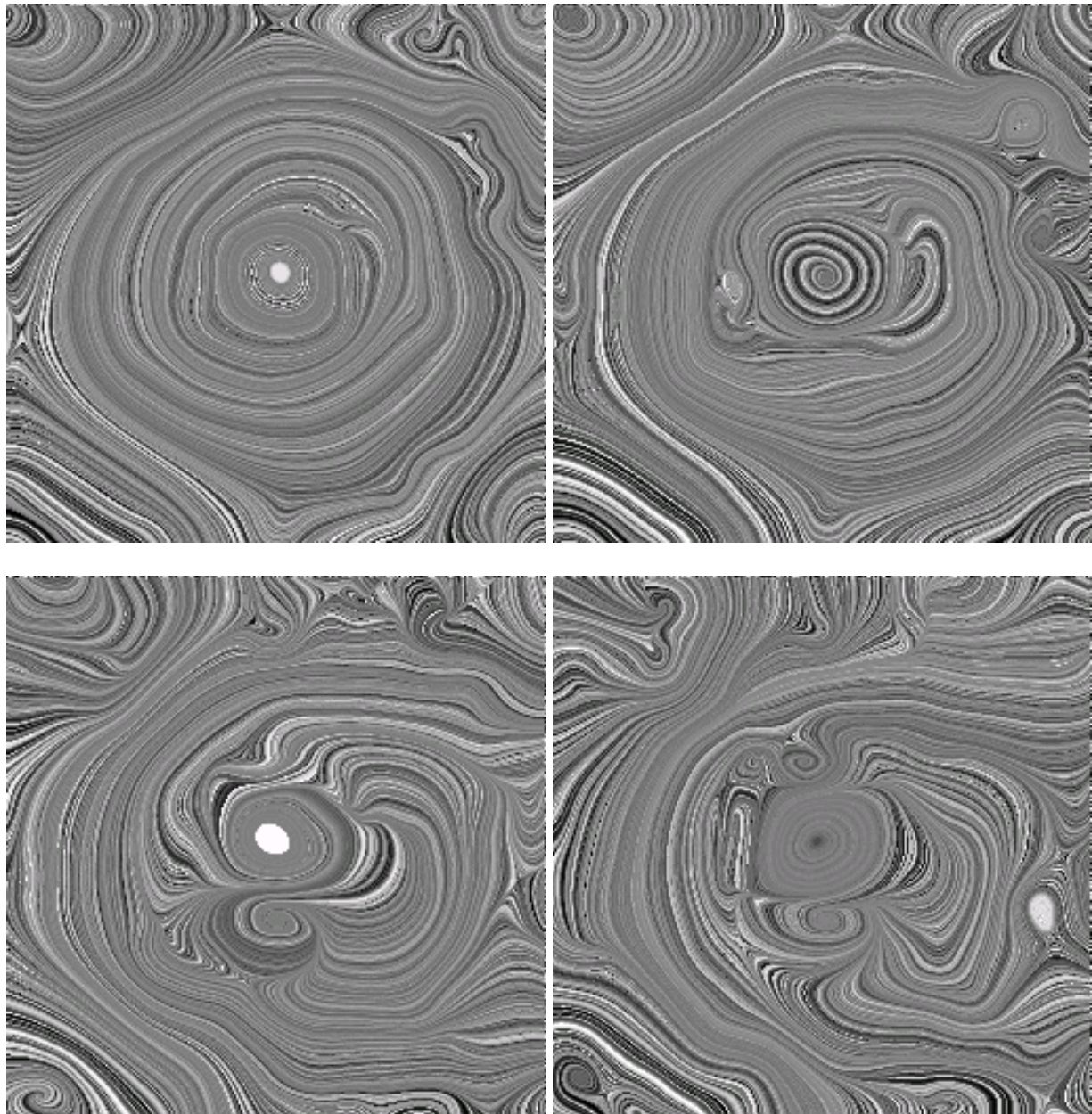
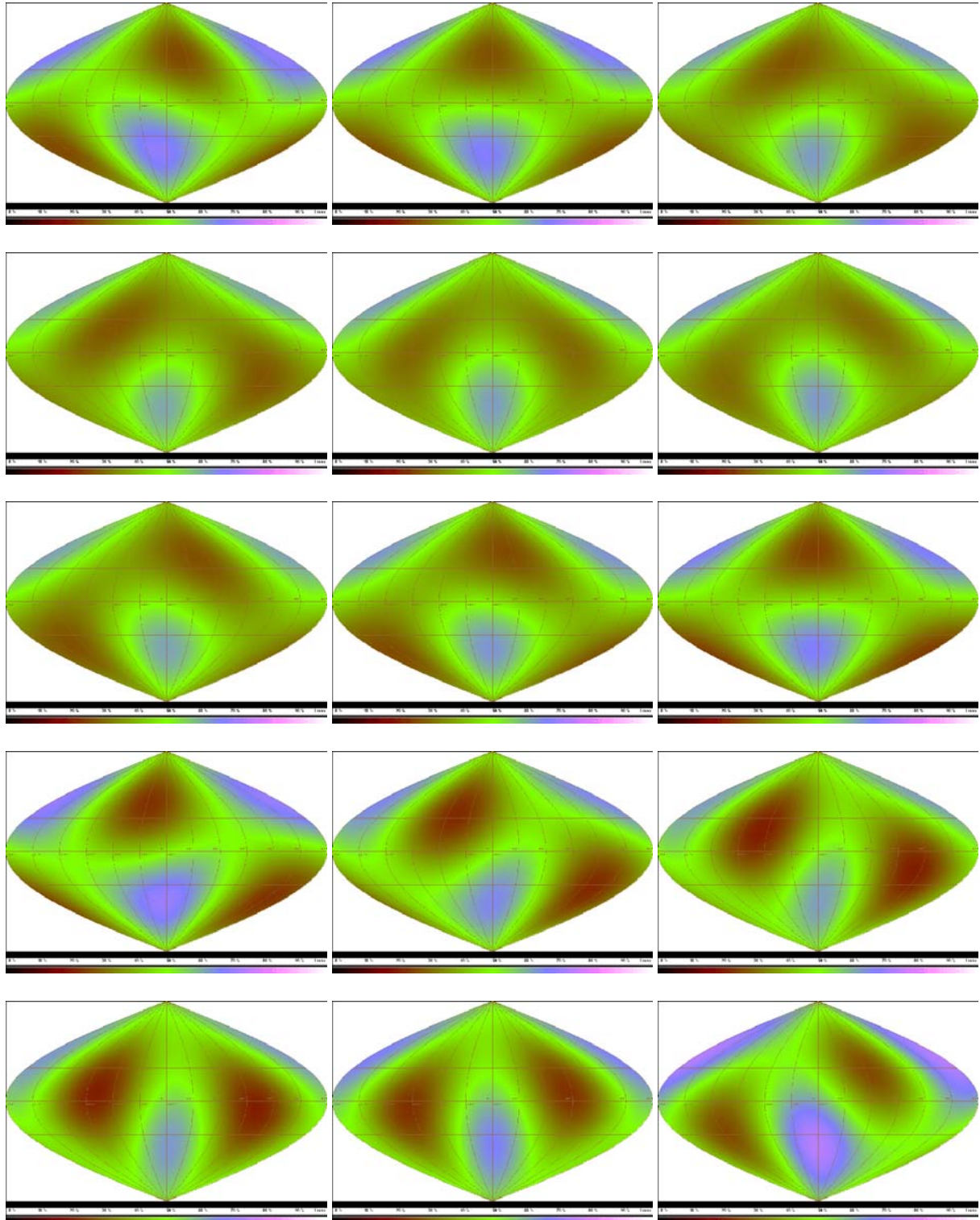


Fig. 54: PIC simulation of the surface turbulent structures. Magnetic field lines in the cross section plane perpendicular to the filament. Number of particles: 600 000, steps 1000, 1200, 1400 and 1600. Radial electric field perturbation: 5%, initial temperature 3 eV both fiber and surroundings. The filament diameter: 30 % of the computational parallelepiped width.

3) Radiation of the fiber

Bremsstrahlung and synchrotron radiation from the moving charged particles was calculated in the module RADIATION. The radiative intensity is projected on a far sphere as described in chapter 3.5. The directional dependence of the radiation during the fiber evolution was calculated. The program package RADIATION was developed for the PIC calculations, but we had used it in other models, for example for treating the radiation of plasma cluster

penetrating through the electric double layer, MHD and compress magnetic bow shock and through the polar cusp of the Earth magnetosphere. In Fig. 55 there can be seen the plasma fiber radiation evolution during the simulation. The number of radiating particles must be very low as the calculation of the radiation with retarded time is very time consuming, for 500 particles typically 1 day on 3 GHz processor.



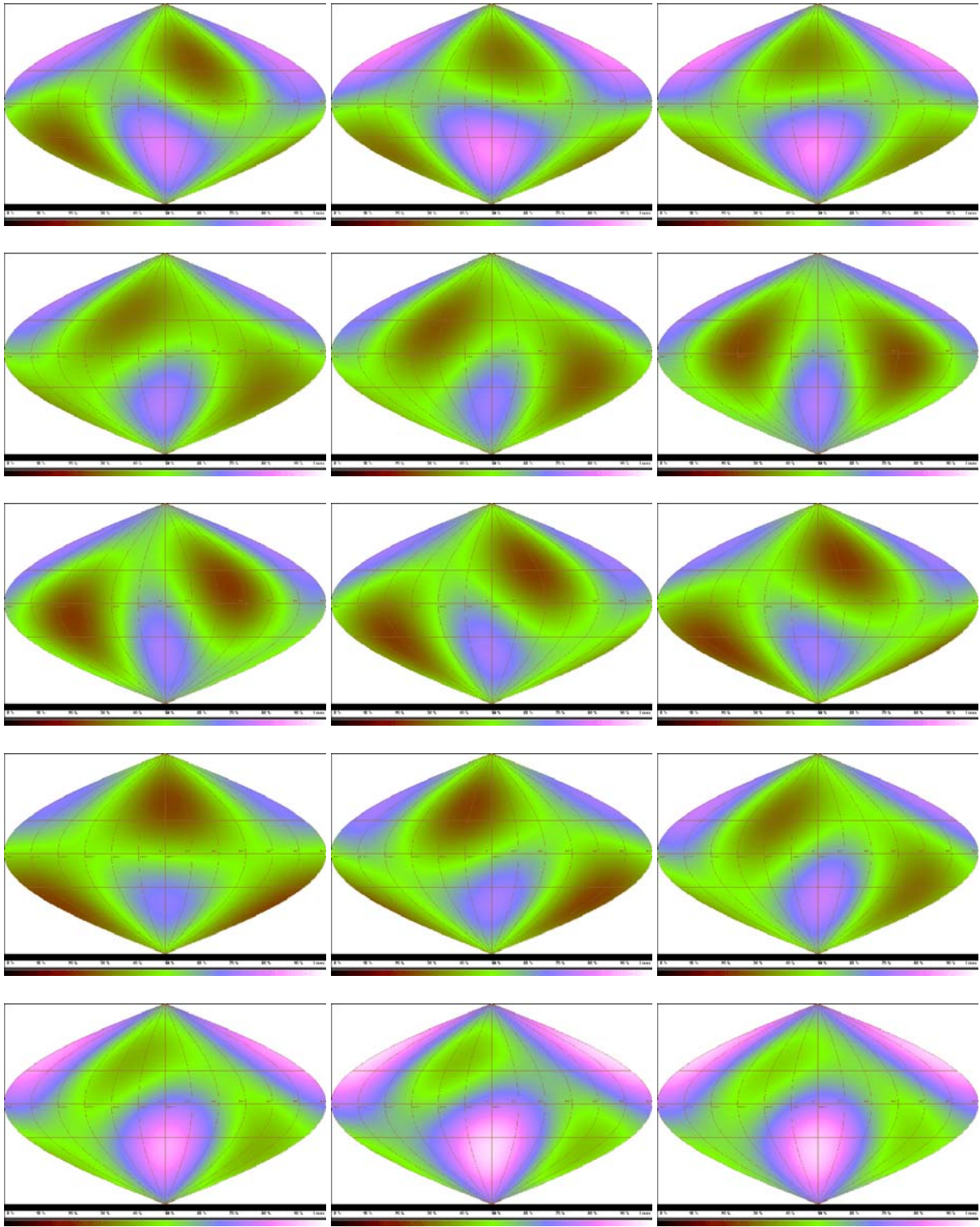


Fig. 55: Plasma fiber radiation in the PIC simulation. Number of electrons: 500, simulation steps: 1000, depicted steps 770, 774, 778 ...886. The grid for field calculation was $33 \times 33 \times 33$, initial perturbation of the particle density in the axis direction was done, non-zero electric field along the fiber axis was applied.

4) New visualization techniques

A great number of visualization routines was developed in frame of the PIC program package. Visualized can be both particle motion and field development. The scene can be rotated, zoomed or shifted during the simulation. Well arranged and transparent Graphic User Interface enables to use particle and field filters, method of visualization or the possibility of recording the animation to avi file. The developed GUI for visualization procedures can be seen in Fig. 56. Details are given in chapters 3.1 and 3.2.

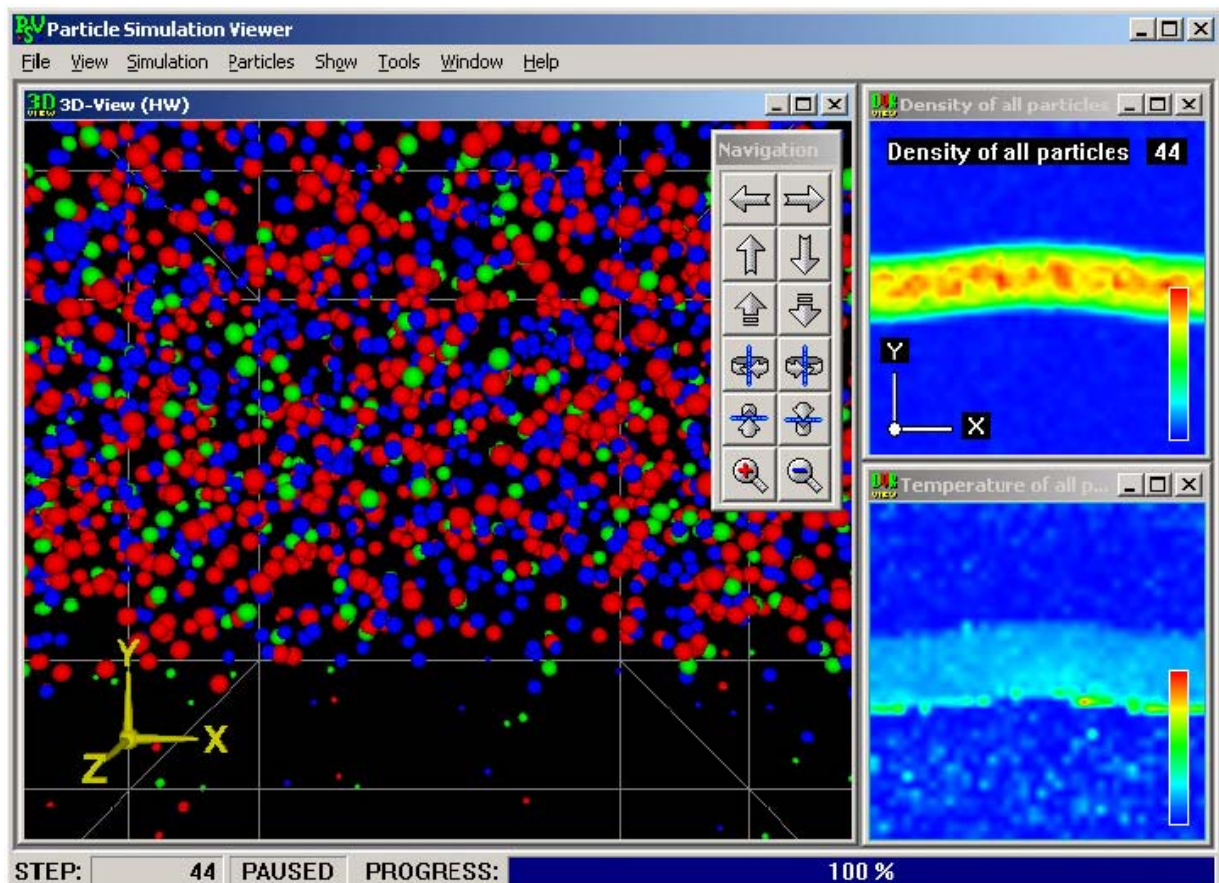


Fig. 56: Developed GUI for visualization procedures

5) Current decomposition

In parallel with the numerical simulations a theoretical analysis of the plasma fiber behaviour was performed. It was shown that current density in the plasma fiber can be decomposed into three parts: The first component is caused by the different gradient B drift of the electrons and ions, the second component is caused by the different curvature drift of the electrons and ions and the last component is a contribution from a charged system of particles

rotating along magnetic field lines in non homogeneous field. Details of the current decomposition are presented in chapter 4.1.

6) Radiative pinch

A simple theoretical model of the radiating pinch was suggested. The radiative intensity is a power function of temperature. Such a course can treat bremsstrahlung, synchrotron radiation and recombination radiation in one formula. The density, pressure and magnetic field profiles of radiative pinch were calculated. A polytropic behaviour of the plasma was proved and polytropic coefficients were found for all the types of radiation. Details can be found in chapter 4.2 for non-helical pinch and in chapter 4.3 for helical pinch.

7) Outline

The PIC model developed during the past five years enables a deep understanding of the processes in the plasma fiber. It is also very efficient package for simulation of MHD shocks, instabilities, electric double layers, polar cusp and other interesting phenomena. In present time the model was used for plasma fiber simulations but the authors of the package are sure it will be useful for a great number of various plasma simulations in future.

REFERENCES

- [1] Opal C. B., Peterson W. K., Beaty E.C. Jr.: *Measurements of secondary electron spectra produced by electron impact ionization of a number of simple gases*, J. Chem. Phys. 55 (1971) 4100.
- [2] Takizuka T., Abe H.: *A Binary Collision Model for Plasma Simulation with a Particle Code*, J. Comput. Phys. 25 (1977) 205.
- [3] Moffatt H. K.: *Magnetic field generation in electrically conducting fluids*, Cambridge University Press, 1978.
- [4] Chen F. F.: *Úvod do fyziky plazmatu*, ACADEMIA, Praha 1984.
- [5] Birdsall C. K.: *Plasma Physics via Computer Simulations*, McGraw-Hill, 1985.
- [6] Surendra M., Graves D. B., Jellum G. M.: *Self – consistent model of a direct – current glos discharge: Treatment of fast electrons*, Phys. Rev. A 41 (1990) 1112.
- [7] Birdsall C. K.: *Particle in Cell Charged - Particle Simulations, Plus Monte Carlo Collisions with Neutral Atoms, PIC-MCC*. IEEE Trans. on Plasma Science **19** (1991) 65.
- [8] Wijk J.: *Spot Noise Texture Synthesis for Data Visualization*, Computer Graphics 25/4 (1991) 309-318.
- [9] The Plasma Theory and Simulation Group Homepage <http://ptsg.eecs.berkeley.edu>
- [10] Peratt A. L.: *Physics of the Plasma Universe*, Springer-Verlag, 1992.
- [11] Kulhánek P.: *The z-Pinch Plasma Column Equilibrium; IX*. Symposium o elementárních procesech a chemických reakcích v nízkoteplotním plazmatu, Častá 1992.
- [12] Hakr J., Kravárik J., Kubeš P., Kulhánek P., Novotný V., Píchal J.: *MHD Model of the Gas Embedded Interrupted Z-pinch*. In: Proceedings of the 21th Intern. Conf. Ion. Gases. Bochum : Universität Bochum, 1993, vol. 1, p. 381-382.
- [13] Hakr J., Kravárik J., Kubeš P., Kulhánek P., Píchal J., Pína L.: *Diagnostics of the Interrupted Z-pinch*. In: Workshop 93. Prague: CTU, 1993, vol. B, p. 93-94.
- [14] Kubeš P., Hakr J., Kravárik J., Kulhánek P., Píchal J.: *Interrupted Z-pinch in Argon*. In: Proc. of the 16th Symp. Plasma Physics and Technology. Prague: CTU, 1993, p. 170-172.
- [15] Kubeš P., Kravárik J., Hakr J., Kulhánek P., Píchal J.: *Observation of the Jets in the Gas Embedded Interrupted Z-pinch*. In: Proc. of the 3rd Int. Conf. Dense Z-pinches. Philadelphia: American Institute of Physics, 1993, p. 620-622. ISBN 1-56396-297-7.

- [16] Kubeš P., Píchal J., Kravárik J., Hakr J., Kulhánek P.: *Z-pinch Discharge Turbulent Energy Considerations*. In: *Contributed Papers, Part II*. Frankfurt: European Physical Society, 1993, p. 353-354.
- [17] Kubeš P., Kravárik J., Hakr J., Kulhánek P., Píchal J., Peřina P.: *Z-Pinch Plasma Jet*. In: *IEEE Transactions on Plasma Science*. 1993, vol. 21, no. 5, p. 605-606.
- [18] Kubeš P., Píchal J., Kulhánek P., Hakr J., Kravárik J., Krejčí A.: *Some Problems of Plasma Pinch Research*. In: *Acta Polytechnica*. 1993, vol. 33, no. 4, p. 59-63.
- [19] Kulhánek P.: *The Z-pinch Plasma Column Equilibrium*. In: *Acta Physica Universitatis Comenianae*. 1993, vol. 34, no. 1, p. 155-157.
- [20] Nishikawa, Wakatani: *Plasma Physics: Basic Theory with Fusion Applications*, SPRINGER-VERLAG, 1994.
- [21] Hakr J., Kravárik J., Kubeš P., Kulhánek P., Píchal J.: *Diagnostics and Dynamics of the Z-pinch*. In: *CTU Seminar 94*. Prague: CTU, 1994, vol. A, p. 87-88.
- [22] Kravárik J., Hakr J., Kubeš P., Kulhánek P., Píchal J.: *Optic Diagnostic Devices for Pulse Discharge Plasma*. In: *CTU Seminar 94*. Prague: CTU, 1994, vol. A, p. 89-90.
- [23] Kubeš P.: Hakr J.: Kravárik J.: Kulhánek P.: Píchal J.: *Vlastnosti imploze plasmatu typu Z-pinč*. In: *Jedenásta konferencia českých a slovenských fyzikov*. Žilina: VŠDS, 1994, s. 9-12. ISBN 80-7100-191-0.
- [24] Kubeš P., Kravárik J., Hakr J., Kulhánek P., Píchal J.: *Magnetic Z-pinch Stable Structure Study*. In: *Symposium EPCR LTP. Abstracts Book*. Bratislava: Comenius University, 1994, p. 8.
- [25] Kubeš P., Kravárik J., Hakr J., Kulhánek P., Píchal J.: *Study of the Plasmoid in the Interrupted Z-pinch*. In: *Proceedings 1994 ICPP*. Sao Jose dos Campos: INPE, 1994, vol. 1, p. 241-244. ISBN 1-56396-496-1.
- [26] Hakr J., Kravárik J., Kubeš P., Kulhánek P., Píchal J., Pína L.: *Laser, Optical and X-ray Plasma Diagnostics of z-Pinch*. In: *Acta Physica Universitatis Comenianae*. 1994, vol. 35, no. 1, p. 149-152.
- [27] Kubeš P., Kravárik J., Hakr J., Kulhánek P., Píchal J.: *Pinč v hustém plazmatu*. In: *Československý časopis pro fyziku*. 1994, roč. 44, č. 4, s. 254-258.
- [28] Kubeš P., Kravárik J., Hakr J., Kulhánek P., Píchal J.: *Stable Structure in the Interrupted z-pinch*. In: *IEEE Transactions on Plasma Science*. 1994, vol. 22, no. 5, p. 605-607.

- [29] Feudel F., Seehafer N., and Schmidtman O.: *Fluid helicity and dynamo bifurcations*, Phys. Lett. A 202, 73-78, 1995.
- [30] Kubeš P., Kravárik J., Hakr J., Kulhánek P., Píchal J., Karpinski L., Paduch M., Tomazsewski K.: *Study of the Conical Electrode Magnetic Field Configuration*. In: Workshop 95. Prague: CTU, 1995, vol. I, p. 83-84.
- [31] Kulhánek P.: *MHD Model of the Z-pinch Mass Transfer*. In: 17th Symposium on Plasma Physics and Technology. Prague: CTU, Faculty of Electrical Engineering, Department of Physics, 1995, p. 144-146. ISBN 80-01-01344-8.
- [32] Kulhánek P., Hakr J., Kubeš P., Kravárik J., Píchal J.: *Compression Time of the Gas Puff Z-pinch*. In: Workshop 95. Prague: CTU, 1995, vol. I, p. 85-86.
- [33] Kubeš P., Kravárik J., Hakr J., Kulhánek P., Píchal J.: *Magnetic Z-pinch Stable Structure Study*. In: Acta Physica Universitatis Comenianae. 1995, vol. 36, no. 2, p. 145-152.
- [34] Kulhánek P.: *Teoretické modely z-pinče*. [Docentská habilitační práce]. Praha : ČVUT, 1996. 101 s.
- [35] Koller J., Kulhánek P., Žáček M.: *Rovnováha z-pinče s radiačními procesy*. In: Sborník abstraktů - 12. konference českých a slovenských fyziků. Ostrava: VŠB-TUO, 1996, díl 1, s. 25. (in Czech).
- [36] Kulhánek P.: *Rovnováha pinče s proměnným elektrickým polem*. In: Sborník abstraktů - 12. konference českých a slovenských fyziků. Ostrava: VŠB-TUO, 1996, s. 28.
- [37] Kulhánek P., Urban M.: *„Z-pinch Equilibrium with non Zero Helicity“*, Proceedings: Workshop 96, TUB&CTU, Prague 1996. Vol. I, p. 117-118.
- [38] Stalling D., Hedge H. C.: *Fast and Resolution Independent LIC*, SIGGRAPH 95 Conference Proceedings, pp. 249-256, ACM SIGGRAPH, 1996.
- [39] Žáček M., Koller J., Kulhánek P.: *Present state of the z pinch equilibrium calculations*, Workshop 97, CTU Prague, 1997.
- [40] Coddington P.: Monte Carlo Simulation for Statistical Physics, <http://www.npac.syr.edu/users/paulc/lectures/montecarlo/>, 1997.
- [41] Kubeš P., Kravárik J. et al.: *Generation of VUV Radiation of a Rod Corona from a Small Magnetic Pinch*, ICPP Prague, 1998.
- [42] Břeň D., Kulhánek P., Škandera D.: *Monte Carlo Simulations of the Systems with Many Particles*. In: Modelling Collective Phenomena in Complex Systems. Eindhoven: European Physical Society, 1998, vol. 22F, p. 182-183.

- [43] Kubeš P., Kulhánek P.: *Magnetic Pinches in Astrophysics and Electromagnetic Collapse*. In: JENAM 98 Abstract. Noordwijk: European Space Agency, 1998, p. 231.
- [44] Kulhánek P., Škandera D., Žáček M., Koller J., Jakeš M., Zelenka J.: *Monte Carlo Simulations of the Systems with Many Particles*. In: Workshop 98. Prague : CTU, 1998, vol. I, p. 105-106.
- [45] Žáček M., Kulhánek P.: *Helicity Pinch Equilibrium with Radiative Processes*. In: 1998 ICPP Contributed Papers. Eindhoven: European Physical Society, 1998, vol. 22C, p. 1005-1008.
- [46] Kulhánek P.: *Pinče a pinčové stěny*. In: Astropis. 1998, roč. 5, č. 4, s. 3-7.
- [47] John C. A.: *Multigrid package MUDPACK 5.0*. National Center for Atmospheric Research; <http://www.scd.ucar.edu/css/software/mudpack>; e-mail: johnad@ucar.edu, 1999.
- [48] Wegenkittl R., Gröller E., Purgathofer W.: *Animating Flowfields: Rendering of Oriented Line Integral Convolution*. Technical Report TR-186-2-96-23. Institute of Computer graphics, Vienna University of Technology, 1999.
- [49] Risquet C. P.: *Visualizing 2D flows: Integrate and Draw*. <http://www.informatic.uni-rostock.de/~carlos/FlowVisualization/IntegrateDraw.html>
- [50] Břeň D., Kulhánek P.: *PIC Simulations of the Plasma z-pinch Column*. In: Proceedings Contributed Papers XXIV ICPIG. Warsaw: IPPLM, 1999, vol. 3, p. 109-110.
- [51] Aubrecht L., Dvorak T., Koller J., Kulhánek P.: *Particle-in-cell Simulation*. In: Proceedings of Workshop 99. Prague: CTU, 1999, p. 72.
- [52] Jackiw R., So-Young Pi: *Creation and Evolution of Magnetic Helicity*, Hep-th 9911072, <http://xxx.lanl.gov>, 1999
- [53] Kulhánek P.: *New Numerical Scheme for Charged Particle Movement*. In: Proceedings of Workshop 2000. Prague: CTU, 2000, vol. A, p. 67. ISBN 80-01-02229-3.
- [54] Kulhánek P.: *3D PIC Model of Helical Current Filament*. In: Proceedings of 6th Granada Seminar on Computational Physics. Granada: Universidad de Granada, 2000, p. 297-306.
- [55] Kulhánek P.: *Particle and Field Solvers in PM Models*, Czechoslovak Journal of Physics, Vol. 50 (2000), Suppl. S3, pp 231-244.
- [56] Novák O.: *Vizualizace plazmového vlákna*, Diploma Thesis, FEE CTU 2000 (in Czech).
- [57] Dejmeck R.: *Simulace jevů v plazmatu metodami PM*, Diploma Thesis, FEE CTU 2001 (in Czech).

- [58] Encyclopedia of Astronomy and Astrophysics: *Magnetic Helicity*, Nature Publishing Group, 2001
- [59] Kulhánek P.: *Present State of PIC Simulations*. In: Proceedings of Workshop 2001. Prague: CTU, 2001, vol. A, p. 64-65. ISBN 80-01-02335-4.
- [60] Břeň D., Kulhánek P.: *Eclipse Zambia 2001*. In: Jihočas. 2001, roč. 9, č. 3, s. 4-8.
- [61] Kulhánek P.: *Expedice Zambia Eclipse 2001*. In: Astropis. 2001, roč. VIII, č. 2, s. 26-27.
- [62] Kulhánek P.: *Expedice Zambia Eclipse II*. In: Astropis. 2001, roč. VIII, č. 3, s. 15-16.
- [63] Kulhánek P.: *Sluneční střípky*. In: Československý časopis pro fyziku. 2001, roč. 2001, č. 4, s. 275-278.
- [64] Škandera D.: *Tvorba modulů pro programový balík PIC*, Diploma Thesis, FEE CTU 2002 (in Czech).
- [65] Stránský M.: *Zkoumání podmínek vzniku a udržení helicitních struktur v plazmatu*, Diploma Thesis, FEE CTU 2002 (in Czech).
- [66] Břeň D.: *Numerical modeling of energy losses in z-pinches*, Proc. 20th SPPT, Czechoslovak Journal of Physics, **52 D** (2002) 226-230.
- [67] Kulhánek P.: *Particle in cell simulation of helical structure onset in plasma fiber with dust grains*, Proc. 20th SPPT, Czechoslovak Journal of Physics, **52 D** (2002) 221-225.
- [68] Kaizr V.: *Low frequency waves in plasma fibers with gravitational field*, Proc. 20th SPPT, Czechoslovak Journal of Physics, **52 D** (2002) 231-234.
- [69] Stránský M.: *Investigation of necessary conditions for creation and preservation of helical structures in plasma*, Proc. 20th SPPT, Czechoslovak Journal of Physics, **52 D** (2002) 235-239.
- [70] Škandera D.: *Relativistic particle solvers in PIC model*, Proc. 20th SPPT, Czechoslovak Journal of Physics, **52 D** (2002) 240-245.
- [71] Pašek J.: *Particle to particle in cell simulations of the plasma*, Proc. 20th SPPT, Czechoslovak Journal of Physics, **52 D** (2002) 246-250.
- [72] Žáček M.: *MHD models of the helical structures in plasma*, Proc. 20th SPPT, Czechoslovak Journal of Physics, **52 D** (2002) 251-254.
- [73] Kulhánek P., Břeň D., Kaizr V., Pašek J.: *Particle in Cell Simulation of Helical Structure Onset in Plasma Fiber with Dust Grains*, in Proceedings „3rd International Conference on the Physics of Dusty Plasmas“, Durban, 2002

- [74] Kaizr V., Kulhánek P., Břeň D., Pašek J.: *Low frequency Waves in Plasma Fibers with Gravitational Field*, in Proceedings „3rd International Conference on the Physics of Dusty Plasmas“, Durban, 2002.
- [75] Břeň D.: *Preparation of the Modul „Radiation“ into Particles in Cells Program Package*, CTU Workshop 2002, 82-83.
- [76] Kaizr V.: *Low Frequency Waves in Plasma Fibers with Gravitational Field*, CTU Workshop 2002, 88-89.
- [77] Kulhánek P.: *New Modules in Particles in Cells Program Package*, CTU Workshop 2002, 76-77.
- [78] Škandera D.: *Charged-Particle Collisions with Neutral Atoms in PIC-MCC Model*, CTU Workshop 2002, 112-113.
- [79] Stránský M.: *Investigation of the Necessary Conditions for Creation and Preservation of Helical Structures in Plasma*, CTU Workshop 2002, 114-115.
- [80] Žáček M.: *Steady-State MHD Models of the Plasma Pinches with Helical Structure*, CTU Workshop 2002, 158-159.
- [81] Kulhánek P.: *Theoretical Physics 1 – Theoretical Mechanics*. Study texts for PhD students. FEE CTU 2000 (in Czech). Download: <http://www.aldebaran.cz/> .
- [82] Kulhánek P.: *Theoretical Physics 2 – Quantum Mechanics*. Study texts for PhD students. FEE CTU 2001 (in Czech). Download: <http://www.aldebaran.cz/> .
- [83] Kulhánek P.: *Theoretical Physics 3 – Statistical Physics*. Study texts for PhD students. FEE CTU 2002 (in Czech). Download: <http://www.aldebaran.cz/> .
- [84] Kulhánek P.: *Theoretical Physics 4 – Waves and Instabilities in Plasma*. Study texts for PhD students. FEE CTU 2002 (in Czech). Download: <http://www.aldebaran.cz/> .

ACKNOWLEDGEMENT

This research has been partially supported by the research program No J04/98:212300017 „Research of Energy Consumption Effectiveness and Quality” of the Czech Technical University in Prague (sponsored by the Ministry of Education, Youth and Sports of the Czech Republic) and by the research program INGO No LA 055 and Research Center of Laser Plasma LA 100 of the Ministry of Education, Youth and Sports of the Czech Republic.

I would like to express my personal thanks to prof. Pavel Kubeš for his permanent support, valuable advice and whole-life optimism. Special thanks belong to my department, doctoral students (Richard Valenta, Miloš Uzel, David Břeň, Martin Žáček, Jan Pašek, Michal Stránský, Dan Škandera, Václav Kaizr, Karel Řezáč), diploma students (Radim Dejmek, Ondřej Novák, Vít Novotný, Martin Hauptvogel, Martin Smetana) and many others.